SIMULATION OF NOISE MECHANISMS IN SCALED BULK AND PARTIALLY DEPLETED SILICON-ON-INSULATOR FIELD-EFFECT TRANSISTORS

By

DEREK O. MARTIN

A DISSERTATION PRESENTED TO THE GRADUATE SCHOOL
OF THE UNIVERSITY OF FLORIDA IN PARTIAL FULFILLMENT
OF THE REQUIREMENTS FOR THE DEGREE OF
DOCTOR OF PHILOSOPHY

UNIVERSITY OF FLORIDA

2007

© 2007 Derek O. Martin

To Kris, Will, Kate, and Emily

ACKNOWLEDGMENTS

I would like to thank my supervisory committee chair, Professor Gijs Bosman, for his guidance and support. I also would like to express my gratitude to Professors Mark Law, Jerry Fossum, and Li Shen for serving on my supervisory committee and for their interest. I thank Qi Xiang and Rainer Thoma for serving as hosts and mentors during my internships. I would also like to thank my former professors, mentors and teachers in research labs and in classrooms, in college and in secondary school. This work would not have been possible without a solid collective of knowledge and experience.

I would also like to thank the Semiconductor Research Company, the National Science Foundation, Advanced Micro Devices, Motorola, Agilent, and the University of Florida for their financial support. I am grateful to Concetta Riccobene of AMD for providing the bulk and SOI transistors measured and simulated in this work, as well as the process descriptions required for process simulation.

My sincerest thanks go to Professor Law, Professor Bosman, Juan Sanchez, and Frank Hou for developing the platform for simulating noise in FLOODS. Without it, this work would not have been possible. I also thank fellow students Lisa Kore and Jong-Hwan Lee for their collaboration and technical discussions.

Finally, I am deeply grateful to my wife, Kris, and my children for their support, patience, and perseverance as I have pursued this work.

TABLE OF CONTENTS

page

ACKNOWLEDGMENTS 4

TABLE 7

LIST OF FIGURES 8

ABSTRACT 11

CHAPTER

1 INTRODUCTION 13

1.1 Fluctuation Phenomena 14
1.2 Numerical Device Simulation 16
1.3 Transport Models 16
1.4 Noise Simulation 19
1.5 SOI Devices and Noise 19

2 TRANSPORT MODELS AND PHYSICAL PROPERTIES 22

2.1 Advanced Transport Models for PDE-based Device Simulation 22
2.1.1 Poisson's Equation 23
2.1.2 Moments of the Boltzmann Transport Equation 23
2.1.2.1 Zeroeth order moment: carrier continuity equations 25
2.1.2.2 First order moment: momentum balance equations 25
2.1.2.3 Second order moment: energy balance equations 26
2.1.2.4 Third order moment: heat flow balance equations 27
2.1.3 Closure and Reduction Relations 27
2.1.3.1 Momentum related reduction relations 28
2.1.3.2 Energy related reduction relations 28
2.1.3.3 Heat flow related reduction and closure relations 28
2.1.3.4 PE and first four BTE moments, closed and summarized . 29
2.1.4 Hydrodynamic Model 29
2.1.5 Reduced Hydrodynamic, or "Energy Balance" Model 30
2.1.6 Drift-Diffusion Model 32
2.2 Implementation of Surface Mobility Models in FLOODS 32
2.2.1 Low Kinetic Energy Mobility Formulation 34
2.2.2 Hot Carrier Mobility 36
2.2.3 Implementation-Specific Details 37
2.3 Implementation of the Energy Balance Transport Equations in FLOODS . 38
2.4 Impact Ionization 40
2.5 Impedance Field Simulation of Velocity Fluctuation Noise 42
2.5.1 Velocity Fluctuation Noise Simulation 42
2.5.1.1 Hydrodynamic model with velocity fluctuation noise . . . 46

2.5.1.2 Energy balance model with velocity fluctuation noise . . . 48
2.5.1.3 Drift-diffusion model with velocity fluctuation noise 51
2.5.2 Velocity Fluctuations in EB and DD Models 52
2.5.2.1 One Dimensional $n^+/n/n^+$ Resistor Simulations 52
2.5.2.2 nMOSFET Simulations 53
2.6 Impedance Field Simulation of Number Fluctuation Noise 54
2.6.1 Number Fluctuation Noise Simulation 54
2.6.1.1 Bulk or surface trap capture and emission 57
2.6.1.2 Direct Carrier tunneling 58
2.6.1.3 Impact Ionization 61
2.6.2 Number Fluctuations in EB and DD Models for $n^+/n/n^+$ Resistors 62
2.7 Quantization Effects and Noise 63

3 NOISE MEASUREMENTS 78

3.1 Measurement Setup 78
3.1.1 Resistor Network Design 78
3.1.2 Practical Considerations 79
3.2 Measured Devices 80

4 SIMULATIONS OF MEASURED DEVICES 101

4.1 The 90nm Bulk MOSFET 102
4.2 The 90nm SOI MOSFET 107

5 CONCLUSION 138

5.1 Summary 138
5.2 Recommendations for Future Work 138

A APPENDIX: SIMULATION FILES 140

BIOGRAPHICAL SKETCH 171

TABLE

Table page

4-1 Final impact ionization rates and carrier lifetimes 123

LIST OF FIGURES

Figure page

1-1 Components of a signal including deterministic and stochastic parts 21

2-1 Electron temperature in a $0.1\mu m$ $n^+/n/n^+$ resistor 66

2-2 Low bias velocity fluctuations in a $0.1\mu m$ $n^+/n/n^+$ resistor 67

2-3 High bias velocity fluctuations in a $0.1\mu m$ $n^+/n/n^+$ resistor 68

2-4 Velocity fluctuation noise for $n^+/n/n^+$ resistors of varying lengths. 69

2-5 EB and DD models and velocity fluctuations in resistor 70

2-6 $0.25\mu m$ nMOSFET doping concentraton 71

2-7 Velocity fluctuations in DD model for $0.25\mu m$ nMOSFET 72

2-8 Velocity fluctuations in EB model for $0.25\mu m$ nMOSFET 73

2-9 Low bias number fluctuations in a $0.1\mu m$ $n^+/n/n^+$ resistor 74

2-10 Number fluctuations noise for $n^+/n/n^+$ resistors of varying lengths 75

2-11 EB and DD models and number fluctuations in resistor 76

2-12 Probability distributions and energies in an infinite well 77

3-1 Circuit used for bulk and SOI device noise measurements. 82

3-2 Physical layout of circuit showing the critical path of electrical connections. . . . 83

3-3 Connection scheme to ensure the avoidance of dielectric breakdown. 84

3-4 Linear scale I_D vs. V_{GS} for $90nm$ bulk nMOSFET 85

3-5 Logarithmic scale I_D vs. V_{GS} for $90nm$ bulk nMOSFET 86

3-6 I_D vs. V_{DS} for $90nm$ bulk nMOSFET 87

3-7 Drain current noise of the $3.2\mu m$ x $90nm$ n-channel bulk MOSFET 88

3-8 Linear scale I_D vs. V_{GS} for $90nm$ SOI nMOSFET 89

3-9 Logarithmic scale I_D vs. V_{GS} for $90nm$ SOI nMOSFET 90

3-10 I_D vs. V_{DS} for $90nm$ SOI nMOSFET 91

3-11 Drain current noise of the $4.8\mu m$ x $90nm$ n-channel SOI MOSFET 92

3-12 Linear scale I_D vs. V_{GS} for $2.33\mu m$ bulk nMOSFET 93

3-13 Logarithmic scale I_D vs. V_{GS} for 2.33μm bulk nMOSFET 94
3-14 I_D vs. V_{DS} for 2.33μm bulk nMOSFET 95
3-15 Drain current noise of the 3.2μm x 2.33μm n-channel bulk MOSFET 96
3-16 Linear scale I_D vs. V_{GS} for 2.33μm SOI nMOSFET 97
3-17 Logarithmic scale I_D vs. V_{GS} for 2.33μm SOI nMOSFET 98
3-18 I_D vs. V_{DS} for 2.33μm SOI nMOSFET 99
3-19 Drain current noise of the 0.6μm x 2.33μm n-channel SOI MOSFET 100
4-1 Absolute value of bulk nMOSFET doping 113
4-2 Linear scale match of I_D vs. V_{GS} in 90nm bulk device. 114
4-3 Logarithmic scale match for I_D vs. V_{GS}. 115
4-4 Match of simulated drain current for bulk device 116
4-5 Match of noise for 90nm bulk nMOSFET with contant trap density. 117
4-6 Drain current noise contribution along channel/oxide surface 118
4-7 Simulated oxide trap locations 119
4-8 Final fit of measured and simulated noise for the 90nm Bulk nMOSFET. 120
4-9 Quantized n(x) under trap 1 121
4-10 Quantized n(x) under traps 2 and 3 122
4-11 Absolute value of SOI nMOSFET doping 124
4-12 Logarithmic scale match of I_D vs. V_{GS}. 125
4-13 Match of simulated drain current for SOI device 126
4-14 Mathematic fit of Lorentzia for plotting 127
4-15 Oxide noise without excess noise 128
4-16 Quantized n(x) under trap 1 129
4-17 Quantized n(x) under traps 2 and 3 130
4-18 Velocity fluctuation noise simulations for $V_{GS} = 1.25V$. 131
4-19 Excess noise at 100Hz. 132
4-20 Linear scale match of I_D vs. V_{DS} with adjusted impact ionization rate 133

4-21 Zero-frequency value of Lorentzia 134
4-22 Cut-off frequency of Lorentzia 135
4-23 Fit of simulated noise with corrected interface charge 136
4-24 Final fit of simulated noise, with modified backside body doping 137

Abstract of Dissertation Presented to the Graduate School
of the University of Florida in Partial Fulfillment of the
Requirements for the Degree of Doctor of Philosophy

SIMULATION OF NOISE MECHANISMS IN SCALED BULK AND PARTIALLY DEPLETED SILICON-ON-INSULATOR FIELD-EFFECT TRANSISTORS

By

Derek O. Martin

May 2007

Chair: Gijs Bosman
Major: Electrical and Computer Engineering

The focus of this dissertation is on the simulation and measurement of low frequency noise in highly scaled bulk and Silicon-On-Insulator (SOI) metal-oxide-semiconductor field-effect devices (MOSFETs). To further the capability of simulating noise in such devices, the Florida Object-Oriented Device Simulator (FLOODS) has been extended to be able to use the Energy Balance system of equations. An advanced surface mobility model is added, and the noise capability of this numerical device simulator is modified to include the mechanism of direct band to oxide trap tunneling for the simulation of degenerate devices.

The derivation of the Energy Balance model and other high-order models is presented, and the correct insertion of noise sources into these models is described. Simple test cases are used to demonstrate the simulation of noise using the model implementation and the effects of this model as compared to the Drift-Diffusion model.

Noise measurements are taken for bulk and SOI MOSFETs, and simulations are performed to match the conditions of the measurements. The shape of the low frequency noise is used to profile the active traps in the gate oxides. While higher order moments than Drift-Diffusion gave anomalous DC simulation results for the devices measured, Drift-Diffusion results are compared to the measured DC and noise data with good agreement, and error correction for quantization effects is computed.

Though the original intended usage of the Energy Balance model was not performed, the Drift Diffusion simulations gave good agreement to the measured data, and this work represents the most complete PDE-based numerical simulation of noise in such devices to date. The analysis provides reverse-engineering of the number and the location of traps in the oxide of the devices measured, which was a primary goal for this work. The error correction for quantization effects validates that quasi-classical numerical simulation is applicable to highly scaled devices. This work also provides encouragement that future work can extend the use of this methodology to emerging device technologies.

CHAPTER 1
INTRODUCTION

Silicon-On-Insulator (SOI) devices have gained acceptance as a way to fabricate semiconductor integrated circuits that are faster than their bulk silicon counterparts, and that allow higher density due to their DC latchup immunity. This higher IC density attribute is best utilized, however, when the body of the SOI device is not contacted, and left to float. Specific noise characteristics unique to such partially depleted devices were recently studied [1], such as excess Lorentzian-shaped components present at high drain bias. Our study further investigated these and other noise characteristics exhibited by modern scaled partially depleted and bulk MOSFETs.

Chapter 2 gives a derivation of moments of the Boltzmann Transport Equation, which yield the energy balance and drift diffusion models. Terms which cause fluctuations and noise in semiconductor devices are tracked through the derivation to show the correct placement of Langevin noise sources in the transport models. The details of the implementation of these transport models in FLOODS are described, including enhancements to allow accurate simulation of scaled devices. A more advanced mobility model is implemented for the accurate simulation of oxide trapping-associated noise. Direct band-to-trap tunneling, necessary for the degenerate channel region of the scaled MOSFETs, is added. Examples of noise simulations in simple devices using high-order transport models for both velocity fluctuation noise and number fluctuation noise are demonstrated. In chapter 3, the measurements of the DC characteristics and noise of bulk and SOI devices are presented. As the devices were not protected from ESD and are difficult to handle, a connection scheme for the execution of noise measurements minimizing high transient voltages is discussed. Chapter 4 describes the reverse engineering and simulation of the devices measured, including all assumptions made and parameters used. Good agreement between simulation and measurement is acheived for the noise due to direct oxide tunneling in both devices. The excess low frequency noise exhibited by the SOI device measurements gives good agreement to both

the magnitude and cutoff frequencies of the simulated Lorentzia, once the fixed interface charge is considered in its proper context for quantization effects. Numerical simulation with the semi-classical drive-diffusion model is shown to be useful for the profiling of traps in the gate oxide of these devices, the simulation of the diffusion noise in SOI devices is shown to give good agreement with measured noise characteristics, and insight into the relationships between various simulation parameters and the resulting noise is acheived. Chapter 5 summarizes what has been accomplished in this work, and gives recommendations for future work.

The following sections of this chapter give background information on the nature of fluctuations in semiconductors, numerical simulation of devices, simulation of noise, and semiconductor devices in general. This is intended to provide a basis for discussion of implementation choices for simulating noise in SOI devices.

1.1 Fluctuation Phenomena

It is helpful to first discuss the nature of noise. Voltages and currents (and number of carriers, carrier velocities, even position of individual atoms) in semiconductors are time dependent signals in a non-linear, causal system. The system consists of the material properties of the semiconductor device (its crystalline makeup, doping concentrations, and geometrical description) and the physical laws that govern the behavior of all parts of the system. Knowledge of the non-linear system itself and its stimuli (inputs to the system, consisting of applied voltages and currents, heat, light, sound, mechanical forces, electric and magnetic fields, gravity, radiation, etc.) allows prediction of many components of the signals in the system. The DC, or mean, component of a signal is equal to its time average, $\int_T s(t)dt/T$, where t is time, $s(t)$ is the signal, and T is the length of the observation. Another possible component is that which is zero-mean and periodic, usually due to periodic stimuli. Finally, there may also be other components which are not periodic, but can be determined from changes to other parts of the system or inputs, such as capacitive or magnetic coupling to other voltages and currents. These components

(whether they are desired or not) are deterministic, and can be entirely predicted from complete knowledge of the system and its stimuli. However, even when all these components are added together, they do not completely describe a signal (Figure 1-1). Some interactions in the highly complex non-linear system are stochastic (random and unpredictable, even with complete system and stimulus knowledge). The stochastic components are the subject of this study, and while their time-dependent value cannot be predicted, some of their phenomenological aspects (e.g. power spectral density and its bias dependencies) can be predicted (given complete knowledge of the system and stimuli). In addition, it is the premise of this work that knowledge of the system (device) that is limited to knowledge of its fabrication methods, currently understood physics and DC and AC characteristics is incomplete, and the measurement and study of the noise in a device can further knowledge of the system.

Commonly observed types of noise include white noise (for which the power spectral density is independent of frequency, at least for observable frequencies), $1/f$ or $1/f$-like noise (in which the power spectral density is approximately inversely proportional to frequency), and Lorentzian shaped noise (for which the power spectral density is white up to a cutoff frequency, above which it decreases inversely proportional to frequency squared). White noise in semiconductor devices is generally due (directly or indirectly) to fluctuation in the average velocity of charge carriers. Lorentzian shaped noise has been attributed to fluctuations in numbers of trapped carriers, and to white noise that is filtered by the non-linear system. $1/f$ noise is somewhat more controversial, and has been attributed to traps, as well as fluctuation in other quantities.

As the knowledge of real semiconductor devices is incomplete (the exact geometries and material properties of a device can only be estimated from knowledge of its fabrication, and the complete physics is approximated by our limited understanding), a pseudo-realistic model of any device considered in this work and its physics is set up for numerical simulation, and the physics of fluctuations in the pseudo-realistic simulated

device are then used to predict the measurable attributes of the noise of the real device. This requires an adequately realistic model of the device and its physics for simulation, accurate measurement of the DC behavior of the device to supplement the understanding of the device itself, and finally, rigorous measurement of the noise of the device.

1.2 Numerical Device Simulation

Partial differential equations' (PDEs) numerical solution and subsequent semiconductor device simulation have been used in the analysis and design of semiconductor devices for nearly half a century [2]. While physics-based compact models (closed-form or near-closed-form solutions based on simplifying approximations such as quasineutrality and depletion) have been shown [3, 4] to be capable of accurately simulating a wide variety of physical effects (some of which are very difficult to model microscopically for PDE-based numerical simulation), and while recent PDE-based models have been shown to be difficult to discretize for stable numerical solution [5], numerical device simulation remains a very helpful tool for the evaluation of physical effects in semiconductor devices. This is particularly true in cases where the physics of devices does not lend itself easily to simplifying assumptions or in cases where obtaining the detailed geometrical dependence of certain effects is desired.

1.3 Transport Models

The derivation of models for charge transport in semiconductor devices typically begins with Poisson's Equation and the Boltzman Transport Equation, and then uses these to derive the PDEs which will be solved in the semiconductor. One such derivation is very nicely given by Lundstrom [6]. This derivation is followed to obtain the hydrodynamic model implemented in the Florida Object-Oriented Device Simulator (FLOODS) as discussed in Chapter 2, though the notation used in this work more closely follows that used by Tang [7].

The drift-diffusion system of equations includes Poisson's Equation and the zeroeth-order moments of the Boltzmann Transport Equation for electrons and holes.

The first-order moments are used to give relations for the particle fluxes. The mobility has been modeled empirically, based on and calibrated to macroscopic averages computed from measurement data. Klaassen gave a model which is used for the computation of doping [8] and temperature [9] dependences of carrier mobilities in bulk silicon. Darwish et al. [10] gave a model which is used to further compute the degraded mobility in surface inversion layers in silicon MOSFETs.

The hydrodynamic and energy balance systems of equations for transport in semiconductor devices are derived from consideration of higher-order moments of the Boltzmann Transport Equation. Many different models have been derived (i.e., Stratton [11] and Bløtkejær [12]). Thoma et al. derived a more physically complex set of equations which do not include any constant-effective-mass approximations and are more consistent with the results of Monte Carlo simulations [13]. Tang [7] derived a generalized model which can be made, through judicious choice of closure relations, to match several other models as demonstrated by Ieong and Tang [14].

Quantization of the inversion layer in MOSFETs has the effects of reducing the overall inversion layer charge (compared to what a classical model would predict), and changing the shape of the distribution of carriers through the channel, such that the peak of the distribution is displaced from the surface. In the devices considered for this work, the carriers in the inversion layer of the device are confined in the vertical (gate to substrate) direction, and as such are subject to quantization effects.

The simulations in this work employ a rough semi-classical approach, assuming that the reduction in the inversion layer charge is approximated by fixed charge at the interface. This approach is not dissimilar to that employed by the recent model presented by Li and Yu [15], which corrects classical models by introducing a fixed charge distributed through the channel. The remaining error lies in the shape of the inversion layer distribution and the position from which carriers can tunnel into the oxide to give rise to low frequency noise.

These effects are, however, shown not to be directly important to the tunneling rates (and therefore the random charging and discharging rates) associated with an oxide trap. Since modifying the physics in the numerical device simulation to include quantization effects does not greatly affect the simulated noise associated with the oxide traps, quantization effects are not directly included in the simulation, though an error correction for the computed trap positions and energies is computed and given.

While the strengths of higher order transport models include more accurate prediction of impact-ionization rates [16] and simulation of some small device effects such as velocity overshoot, these models have also been shown to cause undesirable results. Egley et al. [17] demonstrated an overestimation of hot channel carrier diffusion into floating bodies, leading to incorrect prediction of negative differential drain conductance (or inverse kink effect) in simulations of partially depleted SOI MOSFETs. This result has also been reported by others. To quote Polsky et al. [18, page 504], "hydrodynamic transport produces negative differential resistance (NDR)... no other experimental publication in this area has confirmed the observation of NDR... Therefore, NDR is now considered by many to be an artifact of the hydrodynamic transport model." To quote Munteanu and Le Carval [19, page G574], "We clearly show that anomalous behaviors exist in all major commercial simulation codes and concern both partially depleted silicon-on-insulator devices (inverse kink effect) and bulk transistors (positive substrate current effect)." Polsky notes that the NDR effect is due both to overestimation of inversion carrier diffusion into the floating body and to failures in the hydrodynamic model's handling of Shockley Reed Hall recombination. Several methods have been employed to try to reduce or eliminate the NDR effect, including modifying the diffusivity modeling [19–21], modifying the modeling of the energy relaxation times [19], and by using trap-assisted-tunneling generation-recombination to offset the negative charging [19]. However, no definitive theory has been put forward that satisfyingly resolves the problem in a way that gives great confidence in the accuracy of the modeling, or would work for

a wide range of structures and carrier recombination lifetimes. Further, work by Banoo and Lundstrom [22] has suggested that the hydrodynamic model predicts output currents which are higher than derived ballistic limits. Therefore, these models should be used primarily when the accurate computation of impact-ionization is required or when specific qualitative results – rather than strictly quantitative results – are sought.

1.4 Noise Simulation

The impedance field method for computing noise in semiconductor devices was first proposed by Shockley et al. [23]. This was long used in the context of closed-form analysis, but was also introduced as a methodology useful in the forum of numerical device simulation by Bonani et al. [24]. This has also been implemented in FLOODS for diffusion noise by Sanchez and Hou [25], and for generation-recombination noise by Hou et al. [26]. Simulation of the Fourier coefficients of the solution variables by the method of harmonic balance and subsequent simulation of the inter-frequency mixing of noise have been implemented by Sanchez [27]. Recent work by Hou [28, 29] has added the capability to simulate $1/f$-like noise by considering interface trapping and tunneling of carriers to and from oxide traps.

An alternate method of noise simulation based on the hydrodynamic model was demonstrated by Goo et al. [30], using the modeling of noise sources as small current sources in a lossy transmission line. The simulation of noise in hydrodynamic models using the impedance field method was considered by Bonani et al. [31]; however, details were not given regarding how or whether the fluctuations of physical quantities were coupled into the energy balance equations. More recent work [32] has detailed the coupling of noise fluctuations into higher-order transport models, and this work furthers this goal.

1.5 SOI Devices and Noise

The UFSOI compact models [3] have been developed by professor Fossum and his research group. The charge-based coupling of the front and back surfaces was characterized by Suh and Fossum [4] and Lim and Fossum [33]. Non-local impact

ionization was modeled by Krishnan [16]. Noise modeling was added to the model by Workman [1] and was shown to accurately compute the excess low frequency Lorentzian shape observed in partially depleted devices.

This excess noise in partially depleted SOI transistors has been measured and published by Simoen et al. [34]. Separate measurement data can be found in [1]. Low frequency noise measurements have also been made on buried-channel SOI p-MOSFETs by Lukyanchikova [35]. This work contributes new noise measurements in similarly processed long and short channel bulk and SOI transistors provided by a Semiconductor Research Corporation member company.

After a discussion of the numerical simulation methods used, the analysis of this data using the simulations will be given.

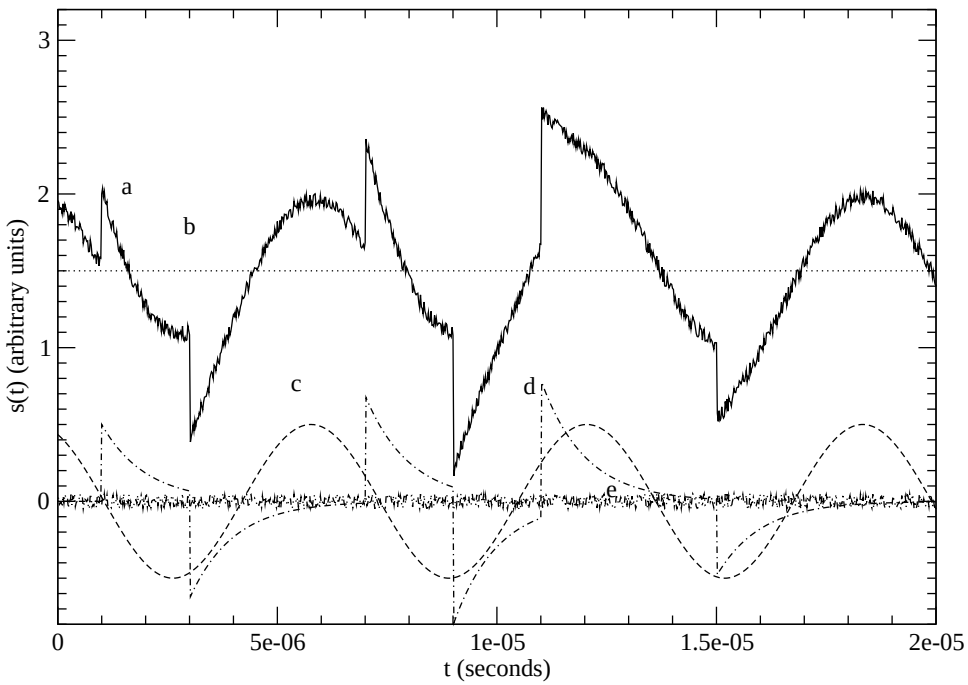

Figure 1-1. Components of a signal (a) in a nonlinear system, including the DC component (b), AC component (c), an aperiodic deterministic component (d), and a stochastic component (e).

CHAPTER 2
TRANSPORT MODELS AND PHYSICAL PROPERTIES

The numerical simulation of scaled modern devices can yield questionable results, if the user does not adequately understand the physical models (including boundary conditions) and assumptions made for the simulations being performed. Furthermore, the modeling of certain properties as appropriate for the newer and more advanced transport models is not fully mature, and the difficulty of numerical simulation makes necessary assumptions for these models which are questionable. Nevertheless, highly scaled devices exhibit effects that can only be adequately captured by transport models that possess sufficient complexity to capture observed behavior. It is desirable to balance the need for increasing complexity with skepticism with regard to certain simulation effects. What follows is a detailed discussion of the origin of each of the transport models and the corresponding usage of impedance-field noise simulation, as well as the modeling of the physical properties of the materials used for the simulation.

2.1 Advanced Transport Models for PDE-based Device Simulation

The Schrödinger wave equation (SWE), Poisson's equation (PE), and the Boltzmann transport equation (BTE) together describe the transport of charge through any semiconductor device (the SWE and PE together define the allowed states in the system and the BTE and PE together describe how the carriers occupy those states, react to electric fields and potential, and transport charge through the device). Transport models are generally simplifications of these equations which can be solved numerically or in closed form.

Generally, in semiconductors such as Silicon, the carriers are nearly free, and the only way the SWE and PE affect transport is in the definition of parameters such as mobility and intrinsic carrier densities, since electrons in the conduction band and holes in the valence band are nearly free carriers. However, in tightly confined areas such as the high field region under the gate oxide in a highly scaled and strongly inverted MOSFET,

the solutions of the SWE and PE give quantized states or sub-bands that alter these properties.

The following derivations of various transport models use the BTE and PE to define the motion of semi-classical carriers moving in a semiconductor device. The SWE does not enter the derivation, save through modeling of band-related parameters.

The implications of neglecting the quantization effect in the devices measured in this work will be discussed after presenting the transport models and the computation of noise associated with each one.

2.1.1 Poisson's Equation

Poisson's Equation relates charge density to the electric field and potential in the semiconductor, and is given as follows:

$$\nabla^2\psi = -\frac{q}{\epsilon}\left(p - n + N_D^+ - N_A^-\right) - \frac{\rho_t}{\epsilon} \tag{2–1}$$

where ψ is the electrostatic potential, $-q$ is the fundamental electron charge, ϵ is the permittivity of the semiconductor, and N_D^+ and N_A^- are the ionized donor and acceptor concentrations. The hole and electron concentrations are p and n. The volume charge density due to charged electron and hole traps is ρ_t. These may be neutral defect states with trapped carriers or donor or acceptor like states which are charged and empty.

2.1.2 Moments of the Boltzmann Transport Equation

The Boltzmann Transport Equation keeps track of all transitions between allowed carrier states in a semiconductor, conserving both energy and momentum. The occupancy function $f(\vec{r}, \vec{p}, t)$ gives the fraction of allowed states which are occupied. In general it is a function of position, momentum, and time but for electrons in a semiconductor in electric and thermal equilibrium it is the Fermi-Dirac distribution. In non-equilibrium the Boltzmann Transport Equation defines f as follows:

$$\frac{df}{dt} + \vec{v}\cdot\nabla_r f - \vec{F}\cdot\nabla_p f = s(\vec{r}, \vec{p}, t) + \left.\frac{\partial f}{\partial t}\right|_{Coll} \tag{2–2}$$

where $\vec{v}$ is the velocity of the carriers occupying states at the considered momentum, position and time. The force impinging on such carriers is $\vec{F}$. The term $s(\vec{r}, \vec{p}, t)$ accounts for the change in f due to interband carrier transitions to and from the considered position and momentum, and $\frac{\partial f}{\partial t}|_{Coll}$ accounts for changes in f due to intraband transitions from one momentum to another. The BTE is arranged here in this way to highlight the fact that terms on the left hand side are deterministic quantities governed by the electron gas and electrostatics. The terms on the right hand side involve collisions with phonons, photons and other non-carrier particles and are therefore stochastic. These right-hand-side terms provide the fluctuating quantities which cause intrinsic device noise.

By multiplying the BTE by some n-ordered functions of momentum $\phi(\vec{p})$ and summing over all allowed momenta, balance equations are defined which nearly account for all of the charge transport effects (but always some non-physical assumption must be made to close the system of equations such that they can be solved). Considering higher-order moments of the BTE, more of the effects of the physics can be captured, but the physical modeling of some terms becomes more uncertain because these terms are more difficult to visualize. As a result, it is desirable (for clarity of results as well as for computational efficiency) to keep the number of moments considered to the minimum needed to close the system of equations and to describe the pertinent physics.

Generally, a moment of the BTE yields a balance equation of the following form.

$$\frac{d}{dt}\left[\frac{1}{\Omega}\sum_p f\phi\right] + \nabla_r \cdot \left[\frac{1}{\Omega}\sum_p \vec{v} f\phi\right] - \vec{F}\cdot\left[\frac{1}{\Omega}\sum_p f\nabla_p\phi\right] = \frac{1}{\Omega}\sum_p s\phi + \frac{1}{\Omega}\sum_p \frac{\partial f}{\partial t}\Big|_{Coll}\phi \quad (2\text{–}3)$$

The validity of moving the $\frac{d}{dt}$ and $\nabla_r\cdot$ operations outside the first two terms and of the chain ruling of gradients to transform the third term is discussed in Lundstrom [6]. The last term is generally expressed by a relaxation time approximation as follows:

$$\frac{1}{\Omega}\sum_p \frac{\partial f}{\partial t}\Big|_{Coll}\phi = \langle\langle\frac{1}{\tau_\phi}\rangle\rangle\frac{1}{\Omega}\sum_p (f - f^0)\phi \quad (2\text{–}4)$$

where the relaxation time is defined by the ensemble average $\langle\langle 1/\tau_\phi \rangle\rangle$ of the following function.

$$\frac{1}{\tau_\phi(\vec{p})} = \sum_{p'} \left(1 - \frac{\phi(\vec{p}')}{\phi(\vec{p})}\right) S(\vec{p}, \vec{p}') \tag{2–5}$$

The balance equations associated with these moments have been rigorously derived previously [6, 7], but this bears repeating as the physical origins of each term in these equations should be understood in order to properly consider the random fluctuation of physical quantities in such systems (resulting from the stochastic terms on the right hand side of Eq. (2–3)).

2.1.2.1 Zeroeth order moment: carrier continuity equations

The carrier continuity equations result from considering the zeroeth-order moment ($\phi(\vec{p}) = 1$) of the BTE for electrons and holes. The electron continuity equation results from this moment (as in Eq. (2–3)) as follows:

$$\frac{d}{dt}\Big[n\Big] + \nabla_r \cdot \Big[n\vec{V}_n\Big] - 0 = [\mathrm{G}_n - \mathrm{R}_n] + 0 \tag{2–6}$$

where $\vec{V}_n$ is the average electron velocity $\langle\vec{v}\rangle$, and G_n and R_n are the electron generation and recombination rates, respectively. The third term is zero because the gradient $\nabla_p\phi = \nabla_p 1$ is zero. The second term on the right hand side is zero because $\phi(\vec{p}') = \phi(\vec{p}) = 1$ and therefore $1 - \frac{\phi(\vec{p}')}{\phi(\vec{p})} = 0$ for all $(\vec{p}, \vec{p}')$. This equation, condensed, and the corresponding equation for holes are given as follows:

$$\frac{dn}{dt} = -\nabla \cdot (n\vec{V}_n) + \mathrm{G}_n - \mathrm{R}_n \tag{2–7}$$

$$\frac{dp}{dt} = -\nabla \cdot (p\vec{V}_p) + \mathrm{G}_p - \mathrm{R}_p \tag{2–8}$$

2.1.2.2 First order moment: momentum balance equations

The momentum balance equations result from considering the first-order moment ($\phi(\vec{p}) = \vec{p} = m^*\vec{v}$) of the BTE for electrons and holes. They are vector-valued. The

momentum balance equation for electrons results from this moment as follows:

$$\frac{d}{dt}\left[n\vec{P}_n\right] + \nabla_r \cdot \left[n\hat{U}_n\right] - (-q\vec{E}n) = 0 + n\vec{C}_{P_n} \tag{2–9}$$

where $\vec{P}_n$ is the average electron momentum $\langle \hbar\vec{k}\rangle$, $\hat{U}_n$ is the kinetic energy tensor $\langle \vec{v}\ \hbar\vec{k}\rangle$, $\vec{E}$ is the electric field, and $\vec{C}_{P_n}$ is the change due to collisions in momentum per electron. The first term on the right hand side is zero because the random velocity of generated or recombined carriers is distributed with spherical symmetry such that the statistical average of $\vec{v}s(\vec{p})$ is zero. This equation, condensed, and the corresponding equation for holes are given as follows:

$$\frac{d(n\vec{P}_n)}{dt} = -\nabla \cdot (n\hat{U}_n) - nq\vec{E} + n\vec{C}_{P_n} \tag{2–10}$$

$$\frac{d(p\vec{P}_p)}{dt} = -\nabla \cdot (p\hat{U}_p) + pq\vec{E} + p\vec{C}_{P_p} \tag{2–11}$$

2.1.2.3 Second order moment: energy balance equations

The energy balance equations result from considering the second-order moment ($\phi(\vec{p}) = \mathrm{E}(\vec{p}) = \frac{|\vec{p}|^2}{2m^*}$) of the BTEs for electrons and holes. The energy balance equation for electrons results from this moment as follows:

$$\frac{d}{dt}\left[nW_n\right] + \nabla_r \cdot \left[n\vec{S}_n\right] - (-q\vec{E}) \cdot (n\vec{V}_n) = [\mathrm{G}_{W_n} - \mathrm{R}_{W_n}] + nC_{W_n} \tag{2–12}$$

where W_n is the average electron kinetic energy $\langle \mathrm{E}\rangle$, $\vec{S}_n$ is the average energy flux per carrier $\langle \mathrm{E}\vec{v}\rangle$, and G_{W_n} and R_{W_n} are the changes in kinetic energy due to particle generation and recombination events, respectively. The change due to collisions in kinetic energy per electron is C_{W_n}. This equation, condensed, and the corresponding equation for holes are given as follows:

$$\frac{d(nW_n)}{dt} = -\nabla \cdot (n\vec{S}_n) - q\vec{E} \cdot (n\vec{V}_n) + \mathrm{G}_{W_n} - \mathrm{R}_{W_n} + nC_{W_n} \tag{2–13}$$

$$\frac{d(pW_p)}{dt} = -\nabla \cdot (p\vec{S}_p) + q\vec{E} \cdot (p\vec{V}_p) + \mathrm{G}_{W_p} - \mathrm{R}_{W_p} + pC_{W_p} \tag{2–14}$$

2.1.2.4 Third order moment: heat flow balance equations

The heat flow balance equations result from considering the third-order moment ($\phi(\vec{p}) = \mathrm{E}(\vec{p})\vec{p}$) of the BTEs for electrons and holes. The heat flow balance equation for electrons results from this moment as follows.

$$\frac{d}{dt}\left[n\vec{Q}_n\right] + \nabla_r \cdot \left[n\hat{R}_n\right] - (-q\vec{E}) \cdot \left[nW_n\hat{I} + n\hat{U}_n\right] = 0 + n\vec{C}_{Q_n} \tag{2–15}$$

where $\vec{Q}_n$ is the average heat flow per electron $\langle \mathrm{E}\ \hbar\vec{k}\rangle$, $\hat{R}_n$ is the fourth-order moment tensor $\langle \vec{v}\,\mathrm{E}\ \hbar\vec{k}\rangle$, $\hat{I}$ is the unit tensor, and $\vec{C}_{Q_n}$ is the change due to collisions in heat flow per electron. The first term on the right hand side, similar to the one in the first-order moment, is zero on statistical average for carriers generated or recombining with spherically symmetric distributed momenta. This equation, condensed, and the corresponding equation for holes are given as follows:

$$\frac{d(n\vec{Q}_n)}{dt} = -\nabla \cdot (n\hat{R}_n) - q\vec{E} \cdot (nW_n\hat{I} + n\hat{U}_n) + n\vec{C}_{Q_n} \tag{2–16}$$

$$\frac{d(p\vec{Q}_p)}{dt} = -\nabla \cdot (p\hat{R}_p) + q\vec{E} \cdot (pW_p\hat{I} + p\hat{U}_p) + p\vec{C}_{Q_p} \tag{2–17}$$

2.1.3 Closure and Reduction Relations

The system of equations derived thus far is not solvable, as the rigorous computation of $\hat{R}_n$ would require a fifth-order moment, which would involve terms requiring even higher order moments, and so on. Also, it is desirable to reduce the number of solution variables to the minimum required to solve the system, in order to reduce the cost of solving the system. Therefore, closure relations are used to close the system, and reduction relations are used to eliminate variables. The closure and reduction relations used in this work are given as follows:

2.1.3.1 Momentum balance equation and related reduction relations

$$\begin{aligned}\vec{P}_n &= m_n^*\vec{V}_n, \quad \vec{C}_{P_n} = \frac{-q\vec{V}_n}{\mu_n^*} + \lambda_{P_n}\nabla\cdot\hat{U}_n, \quad \hat{U}_n = U_n\hat{I} = kT_n\hat{I} \\ \vec{P}_p &= m_p^*\vec{V}_p, \quad \vec{C}_{P_p} = \frac{-q\vec{V}_p}{\mu_p^*} + \lambda_{P_p}\nabla\cdot\hat{U}_p, \quad \hat{U}_p = U_p\hat{I} = kT_p\hat{I}\end{aligned} \tag{2–18}$$

where m_n^* and m_p^* are the electron and hole conductivity effective masses. The electron and hole mobilities are $\mu_n^* = \frac{q\langle\tau_{P_n}\rangle}{m_n^*}$ and $\mu_p^* = \frac{q\langle\tau_{P_p}\rangle}{m_p^*}$, where $\langle\tau_{P_n}\rangle$ and $\langle\tau_{P_p}\rangle$ are the electron and hole momentum relaxation times. The values λ_{P_n} and λ_{P_p} are factorless empirical parameters that model the behavior of the system in inhomogeneous field conditions, consistent with Monte Carlo computations [7]. The relations involving $\hat{U}_n$ and $\hat{U}_p$ reflect the equipartition energy approximation and define the carrier temperatures.

2.1.3.2 Energy balance equation and related reduction relations

$$\begin{aligned}W_n &= \frac{3}{2}kT_n, \quad C_{W_n} = \frac{-(W_n - W_n^0)}{\langle\tau_{W_n}\rangle}, \quad W_n^0 = \frac{3}{2}kT_L \\ W_p &= \frac{3}{2}kT_p, \quad C_{W_p} = \frac{-(W_p - W_p^0)}{\langle\tau_{W_p}\rangle}, \quad W_p^0 = \frac{3}{2}kT_L\end{aligned} \tag{2–19}$$

The relations involving W_n and W_p reflect the approximation that the carrier kinetic energies are entirely due to random thermal motion rather than organized drifting motion; i.e., $\vec{v} = \langle\vec{v}\rangle + \delta\vec{v}$ and $W_n = \langle\frac{1}{2}m^*|\vec{v}|^2\rangle \approx \langle\frac{1}{2}m^*|\delta\vec{v}|^2\rangle = \frac{3}{2}kT_n$. τ_{W_n} and τ_{W_p} are the electron and hole energy relaxation times.

2.1.3.3 Heat flow balance equation and related reduction and closure relations

$$\begin{aligned}\vec{Q}_n &= m_n^*\vec{S}_n, \quad \vec{C}_{Q_n} = \frac{-q\vec{S}_n}{\mu_{S_n}^*} + \lambda_{Q_n}\nabla\cdot\hat{R}_n, \quad \hat{R}_n = R_n\hat{I} = \frac{10}{9}W_n^2\hat{I} \\ \vec{Q}_p &= m_p^*\vec{S}_p, \quad \vec{C}_{Q_p} = \frac{-q\vec{S}_p}{\mu_{S_p}^*} + \lambda_{Q_p}\nabla\cdot\hat{R}_p, \quad \hat{R}_p = R_p\hat{I} = \frac{10}{9}W_p^2\hat{I}\end{aligned} \tag{2–20}$$

The electron and hole heat flow mobilities are $\mu_{S_n}^* = \frac{q\langle\tau_{Q_n}\rangle}{m_n^*}$ and $\mu_{S_p}^* = \frac{q\langle\tau_{Q_p}\rangle}{m_p^*}$, where $\langle\tau_{Q_n}\rangle$ and $\langle\tau_{Q_p}\rangle$ are the electron and hole heat flow relaxation times. The values λ_{Q_n} and λ_{Q_p} are factorless empirical parameters that model the behavior of the system in inhomogeneous

field conditions, consistent with Monte Carlo computations [7]. The relations involving $\hat{R}_n$ and $\hat{R}_p$ reflect the equipartition energy approximation and close the system of equations. Their validity has also been verified by Monte Carlo computations [7].

2.1.3.4 PE and first four BTE moments, closed and summarized

The system of equations thus derived and closed can be summarized as follows:

$$\nabla^2\psi = -\frac{q}{\epsilon}(p - n + N_D^+ - N_A^-) - \frac{\rho_t}{\epsilon} \tag{2–21}$$

$$\frac{dn}{dt} = -\nabla\cdot(n\vec{V}_n) + \mathrm{G}_n - \mathrm{R}_n \tag{2–22}$$

$$\frac{dp}{dt} = -\nabla\cdot(p\vec{V}_p) + \mathrm{G}_p - \mathrm{R}_p \tag{2–23}$$

$$m_n^*\frac{d(n\vec{V}_n)}{dt} = -\nabla(nkT_n) - qn\vec{E} - n\left(\frac{q\vec{V}_n}{\mu_n^*} - \lambda_{P_n}\nabla(kT_n)\right) \tag{2–24}$$

$$m_p^*\frac{d(p\vec{V}_p)}{dt} = -\nabla(pkT_p) + qp\vec{E} - p\left(\frac{q\vec{V}_p}{\mu_p^*} - \lambda_{P_p}\nabla(kT_p)\right) \tag{2–25}$$

$$\frac{3}{2}k\frac{d(nT_n)}{dt} = -\nabla\cdot(n\vec{S}_n) - q\vec{E}\cdot(n\vec{V}_n) + \mathrm{G}_{W_n} - \mathrm{R}_{W_n} - \frac{3}{2}nk\frac{T_n - T_L}{\langle\tau_{W_n}\rangle} \tag{2–26}$$

$$\frac{3}{2}k\frac{d(pT_p)}{dt} = -\nabla\cdot(p\vec{S}_p) + q\vec{E}\cdot(p\vec{V}_p) + \mathrm{G}_{W_p} - \mathrm{R}_{W_p} - \frac{3}{2}pk\frac{T_p - T_L}{\langle\tau_{W_p}\rangle} \tag{2–27}$$

$$m_n^*\frac{d(n\vec{S}_n)}{dt} = -\nabla\left(\frac{5}{2}nk^2T_n^2\right) - q\vec{E}\left(\frac{5}{2}nkT_n\right) - n\left(\frac{q\vec{S}_n}{\mu_{S_n}^*} - \lambda_{Q_n}\nabla\left(\frac{5}{2}k^2T_n^2\right)\right) \tag{2–28}$$

$$m_p^*\frac{d(p\vec{S}_p)}{dt} = -\nabla\left(\frac{5}{2}pk^2T_p^2\right) + q\vec{E}\left(\frac{5}{2}pkT_p\right) - p\left(\frac{q\vec{S}_p}{\mu_{S_p}^*} - \lambda_{Q_p}\nabla\left(\frac{5}{2}k^2T_p^2\right)\right) \tag{2–29}$$

This four-moment system is not commonly solved, as it is very complex, and the number of variables to be solved is still quite high (9 variables for 1-D problems, 13 for 2-D problems and 17 for 3-D problems). Further approximations are therefore made to get to the hydrodynamic systems that are commonly solved. However, this system will be useful for determining where fluctuations couple into the system and how noise simulations should be extended to include higher-order moments.

2.1.4 Hydrodynamic Model

The first reduction to the equations derived thus far involves the quasi-stationary approximation with regard to the heat flow balance equations, namely that the time

derivative terms on the left hand side are negligible compared with any of the terms on the ride hand side. These equations are then reduced from partial differential equations to vector expressions for the heat flow. This eliminates 2 to 6 variables (depending on the dimensionality of the solution space) from the solution set. The remaining system constitutes the hydrodynamic model and consists of the first seven previous Eqs. (2–21 – 2–27) with the remaining two auxiliary relations for heat flow, as follows:

$$
\begin{aligned}
\nabla^2\psi &= -\frac{q}{\epsilon}(p - n + N_D^+ - N_A^-) - \frac{\rho_t}{\epsilon} \\
\frac{dn}{dt} &= -\nabla\cdot(n\vec{V}_n) + \mathrm{G}_n - \mathrm{R}_n \\
\frac{dp}{dt} &= -\nabla\cdot(p\vec{V}_p) + \mathrm{G}_p - \mathrm{R}_p \\
m_n^*\frac{d(n\vec{V}_n)}{dt} &= -\nabla(nkT_n) - qn\vec{E} - n\left(\frac{q\vec{V}_n}{\mu_n^*} - \lambda_{P_n}\nabla(kT_n)\right) \\
m_p^*\frac{d(p\vec{V}_p)}{dt} &= -\nabla(pkT_p) + qp\vec{E} - p\left(\frac{q\vec{V}_p}{\mu_p^*} - \lambda_{P_p}\nabla(kT_p)\right) \\
\frac{3}{2}k\frac{d(nT_n)}{dt} &= -\nabla\cdot(n\vec{S}_n) - q\vec{E}\cdot(n\vec{V}_n) + \mathrm{G}_{W_n} - \mathrm{R}_{W_n} - \frac{3}{2}nk\frac{T_n - T_L}{\langle\tau_{W_n}\rangle} \\
\frac{3}{2}k\frac{d(pT_p)}{dt} &= -\nabla\cdot(p\vec{S}_p) + q\vec{E}\cdot(p\vec{V}_p) + \mathrm{G}_{W_p} - \mathrm{R}_{W_p} - \frac{3}{2}pk\frac{T_p - T_L}{\langle\tau_{W_p}\rangle} \\
\vec{S}_n &= -\frac{\mu_{S_n}^*}{q}\left[\frac{5}{2}kT_nq\vec{E} + \frac{5}{2}k^2T_n^2\frac{\nabla n}{n} + (1-\lambda_{Q_n})\nabla\left(\frac{5}{2}k^2T_n^2\right)\right] \qquad (2\text{–}30) \\
\vec{S}_p &= -\frac{\mu_{S_p}^*}{q}\left[-\frac{5}{2}kT_pq\vec{E} + \frac{5}{2}k^2T_p^2\frac{\nabla p}{p} + (1-\lambda_{Q_p})\nabla\left(\frac{5}{2}k^2T_p^2\right)\right] \qquad (2\text{–}31)
\end{aligned}
$$

Thus the system to be solved is reduced to have a solution set of up to 11 variables: ψ, n, p, V_{nx}, V_{ny}, V_{nz}, V_{px}, V_{py}, V_{pz}, T_n, and T_p.

2.1.5 Reduced Hydrodynamic, or "Energy Balance" Model

The next analogous reduction to the equations derived thus far involves the quasi-stationary approximation with regard to the momentum balance equations, namely that the time derivative terms on the left hand side are negligible compared with any of the terms on the ride hand side. These equations are also reduced from partial differential equations to vector expressions for the carrier velocities. This eliminates an additional 2 to

6 variables (depending on the dimensionality) from the solution set. The remaining system constitutes the "energy balance" model and consists of Poisson's equation (2–21), the electron and hole continuity equations (2–22 and 2–23) and the electron and hole energy balance equations (2–26 and 2–27), with the auxiliary relations for heat flow (Eqs. (2–30 and 2–31)) and the additional two auxiliary relations for carrier velocities.

$$
\begin{aligned}
\nabla^2\psi &= -\frac{q}{\epsilon}(p - n + N_D^+ - N_A^-) - \frac{\rho_t}{\epsilon} \\
\frac{dn}{dt} &= -\nabla\cdot(n\vec{V}_n) + \mathrm{G}_n - \mathrm{R}_n \\
\frac{dp}{dt} &= -\nabla\cdot(p\vec{V}_p) + \mathrm{G}_p - \mathrm{R}_p \\
\vec{V}_n &= -\frac{\mu_n^*}{q}\left[q\vec{E} + kT_n\frac{\nabla n}{n} + (1-\lambda_{P_n})\nabla(kT_n)\right] && (2\text{–}32) \\
\vec{V}_p &= -\frac{\mu_p^*}{q}\left[-q\vec{E} + kT_p\frac{\nabla p}{p} + (1-\lambda_{P_p})\nabla(kT_p)\right] && (2\text{–}33) \\
\frac{3}{2}k\frac{d(nT_n)}{dt} &= -\nabla\cdot(n\vec{S}_n) - q\vec{E}\cdot(n\vec{V}_n) + \mathrm{G}_{W_n} - \mathrm{R}_{W_n} - \frac{3}{2}nk\frac{T_n - T_L}{\langle\tau_{W_n}\rangle} \\
\frac{3}{2}k\frac{d(pT_p)}{dt} &= -\nabla\cdot(p\vec{S}_p) + q\vec{E}\cdot(p\vec{V}_p) + \mathrm{G}_{W_p} - \mathrm{R}_{W_p} - \frac{3}{2}pk\frac{T_p - T_L}{\langle\tau_{W_p}\rangle} \\
\vec{S}_n &= -\frac{\mu_{S_n}^*}{q}\left[\frac{5}{2}kT_nq\vec{E} + \frac{5}{2}k^2T_n^2\frac{\nabla n}{n} + (1-\lambda_{Q_n})\nabla\left(\frac{5}{2}k^2T_n^2\right)\right] \\
\vec{S}_p &= -\frac{\mu_{S_p}^*}{q}\left[-\frac{5}{2}kT_pq\vec{E} + \frac{5}{2}k^2T_p^2\frac{\nabla p}{p} + (1-\lambda_{Q_p})\nabla\left(\frac{5}{2}k^2T_p^2\right)\right]
\end{aligned}
$$

Thus the system to be solved is reduced to have a solution set of 5 variables: ψ, n, p, T_n, and T_p.

To avoid the direct computation of the vector particle velocity, the Joule heating terms of the energy balance equations (such as $-q\vec{E}\cdot(n\vec{V}_n)$) are typically rearranged as follows [2].

$$
-q\vec{E}\cdot(n\vec{V}_n) = q\nabla\cdot(\psi n\vec{V}_n) - q\psi\nabla\cdot(n\vec{V}_n) = q\nabla\cdot(\psi n\vec{V}_n) + q\psi\left(\frac{dn}{dt} - \mathrm{G}_n + \mathrm{R}_n\right) \quad (2\text{–}34)
$$

$$
q\vec{E}\cdot(p\vec{V}_p) = -q\nabla\cdot(\psi p\vec{V}_p) + q\psi\nabla\cdot(p\vec{V}_p) = -q\nabla\cdot(\psi p\vec{V}_p) - q\psi\left(\frac{dp}{dt} - \mathrm{G}_p + \mathrm{R}_p\right) \quad (2\text{–}35)
$$

The $\nabla\cdot(\psi n\vec{V}_n)$ terms can be discretized using Sharfetter-Gummel type methods [2].

2.1.6 Drift-Diffusion Model

Further reduction of the system can be made by considering the electrons and holes to be near thermal equilibrium, such that $T_n \approx T_p \approx T_L$. For this case, the energy balance equations can be eliminated and some terms can be dropped from the expressions for carrier velocities (Eqs. (2–32) and (2–33)). The remaining system constitutes the drift-diffusion model, and consists of the first three equations of the previously derived systems, and the simplified auxiliary relations for the carrier velocities, as follows.

$$\begin{aligned}
\nabla^2\psi &= -\frac{q}{\epsilon}(p - n + N_D^+ - N_A^-) - \frac{\rho_t}{\epsilon} \\
\frac{dn}{dt} &= -\nabla\cdot(n\vec{V}_n) + \mathrm{G}_n - \mathrm{R}_n \\
\frac{dp}{dt} &= -\nabla\cdot(p\vec{V}_p) + \mathrm{G}_p - \mathrm{R}_p \\
\vec{V}_n &= -\frac{\mu_n^*}{q}\left[q\vec{E} + kT_L\frac{\nabla n}{n} + (1-\lambda_{P_n})\nabla(kT_L)\right] && (2\text{–}36) \\
\vec{V}_p &= -\frac{\mu_p^*}{q}\left[-q\vec{E} + kT_L\frac{\nabla p}{p} + (1-\lambda_{P_p})\nabla(kT_L)\right] && (2\text{–}37)
\end{aligned}$$

Thus in the most simple case of bipolar transport the system to be solved is reduced to a solution set of 3 variables: ψ, n and p.

2.2 Implementation of Surface Mobility Models in FLOODS

In order to simulate the noise in SOI devices, it is first necessary to be able to simulate the DC and AC characteristics of the device with reasonable accuracy. This requires the use of a mobility model that takes into account the degradation of carrier mobility in semiconductor devices (such as SOI MOSFETs) in which the carriers are tightly bound near an insulator surface.

In addition (and more importantly), the impedance field noise simulation available in FLOODS has recently been extended [28] to include trapping at silicon/silicon dioxide interfaces and tunneling between these interface traps and traps located in the oxide. This noisy process provides slow enough transitions to produce low frequency Lorentzian-shaped noise components, and the distribution of oxide traps in position can be

produce an exponential distribution of time constants suitable for $1/f$ or $1/f$-like noise. While $1/f$-like noise is understood to be caused by the fundamental noise mechanism of number fluctuation, it is true that carriers trapped in the oxide cause fluctuations in the electric field which binds the carriers in the channel to the surface. Therefore, the effective mobility of the carriers in the channel may fluctuate as a secondary effect. While this is not expected to dominate the noise spectrum, it may have an effect on the Green's functions produced by the system of equations in that it gives an extra coupling path between the trapped carrier continuity equation in the oxide node and the external device contact (the charging of the trap now couples to Poisson's Equation and, in addition, the carrier continuity equation at the interface node).

It is important to note that even though the surface mobility models that have been published are based on some expectation of their physical form, they are empirically shaped to fit macroscopic "effective" mobilities which are obtained from compact model-type expressions matched to measured data. Therefore, the coupling from the traps in the oxide to the mobility modeled in the channel should be viewed as a tool to give possible physical insight and qualitative understanding, rather than a rigorously accurate quantitative result. The surface mobility model parameters published may vary wildly from those required to match the dependence of carrier mobilities on electric field in different processes with differing oxidation recipes or impurities present near the interface. Also, the model is empirically determined for single-gate bulk Silicon MOSFETs and while it is expected to apply to the partially depleted SOI devices in this study, results may deviate if the model is applied to highly scaled fully depleted SOI MOSFETs or double-gate MOSFETs where the carriers are expected to interact with front and back interfaces or where the electric field distribution is very different in the inversion layer (as in symmetric double-gate structures). These models also would likely give errant results in a system such as the density gradient system [5] for accounting for quantum confinement effects where the carriers are displaced a distance from the interface.

Early surface mobility models used the distance from a semiconductor interface to model the decrease in mobility [36]. This is non-physical, as it is expected that tighter electrostatic binding to a surface should further increase the scattering of carriers by the roughness of the surface and by surface acoustic phonons. Modern surface mobility models ([37], [10]) empirically model the surface mobility by degrading the mobility as a function of electric field perpendicular to the interface. Some implementations have used a non-locally computed "effective" surface field computed throughout the inversion layer. This would be expected to give the best fit to the macroscopic "effective" mobility data, but causes some difficulty in implementation, as it yields nonzero derivative terms which are far off the diagonal of the Jacobian matrix, increasing the cost of solving the numerical system and requiring difficult implementation for a generalized script-based simulator such as FLOODS for problems in which small-signal AC solutions are required. Some implementations have used the local field perpendicular to the nearest interface (the "vertical" field is sometimes used, limiting the applicability of the implementation to planar MOSFETs). Some have used the electric field perpendicular to the edges in the mesh (the assumption being that if there is much current flowing through the edge then it must be aligned closely with the direction of the current flow,and if the perpendicular field is high for this case, then the edge must be located near to a surface-binding field). While this may not be as accurate as using the vertical field, it does allow the mobility model to be used in a wider variety of geometries. The exact implementation does not seem to be that important [38] as in the limits of dense meshes and high surface fields (which are the cases that are of most concern) these assumptions become more valid.

2.2.1 Low Kinetic Energy Mobility Formulation

The surface mobility model implemented in FLOODS for this work is that presented by Darwish, et. al [10]. This model was formulated as an update to the Lombardi model [37] which is similar in form but under-predicts the degradation of the mobility at very high electric fields in scaled processes which are expected to have similar surface

mobility model parameters to those of their less highly scaled predecessors, due to similar oxidation processing. The Darwish model degrades the bulk mobility (μ_b) by using Mathiessen's Rule to reciprocally combine it with two other mobility terms, as follows.

$$\frac{1}{\mu_0(\vec{r})} = \frac{1}{\mu_b(\vec{r})} + \frac{1}{\mu_{ac}(\vec{r})} + \frac{1}{\mu_{sr}(\vec{r})} \tag{2–38}$$

The result μ_0 is the low kinetic energy mobility which will in turn be degraded for hot carrier effects, as will be discussed later. The values μ_{ac} and μ_{sr} are mobility terms which account for surface acoustic phonon scattering and surface roughness scattering, respectively. The surface acoustic phonon scattering term is computed as follows.

$$\mu_{ac}(\vec{r}) = \left(\frac{B}{E_\perp(\vec{r})} \left(\frac{T_L}{300} \right)^\kappa + \frac{C N_I^\tau(\vec{r})}{E_\perp^{1/3}(\vec{r})} \right) \left(\frac{300}{T_L} \right)^\kappa \tag{2–39}$$

where B and C are based on physically derived quantities, but are expected to vary with fixed interface charge and are therefore treated as fit parameters. The value τ is an empirical fit parameter, and κ is the temperature dependence of the probability of surface phonon scattering (1.7 for electrons and 0.9 for holes). The value $N_I = N_D^+ + N_A^-$ is the total density of ionized impurities. The surface roughness scattering term (dominant for high perpendicular fields) is computed as follows.

$$\mu_{sr}(\vec{r}) = \frac{\delta}{E_\perp^\gamma(\vec{r})} \tag{2–40}$$

where δ is a fit parameter which depends on the oxidation process, and is expected to be vary wildly from process to process. The parameter γ is given a weak dependence on inversion charge (it is held constant in the Lombardi formulation) as follows.

$$\gamma = A + \frac{\alpha n(\vec{r})}{N_I^\eta(\vec{r})} \tag{2–41}$$

where A, α, and η are fitting parameters.

2.2.2 Hot Carrier Mobility

Electrons and holes in Silicon are characterized by velocity that saturates under the condition of high homogeneous field, or high average kinetic energy. In drift-diffusion simulations, the accelerating electric field (parallel to the direction of current flow) is used to model the velocity saturation effect, though in highly scaled devices the field is far from homogeneous and the kinetic energy of the electron distribution is a more appropriate and physical measure for modeling this effect. The Darwish mobility model was originally developed for use in drift-diffusion simulations, and the velocity saturation expression used was that of Hänsch, as follows.

$$\mu(\vec{r}) = \frac{2\mu_0(\vec{r})}{1 + \left(1 + 4\left(\frac{\mu_0(\vec{r})E_{\parallel}(\vec{r})}{v_{sat}}\right)^2\right)^{\frac{1}{2}}} \tag{2–42}$$

In the context of a hydrodynamic simulation, the velocity saturation effect should rather be modeled as a function of average kinetic energy or electron temperature. A common approach used for this is to consider the electron or hole energy balance equation under the condition of a long, homogeneous field. This yields an expression for carrier temperature as a function of such a long stationary homogeneous field E_s. The inverse of this function is expressed as follows (for electrons).

$$E_s = \sqrt{\frac{3}{2}\frac{k(T_n - T_L)}{q\mu_n^*\tau_{E_n}}} \tag{2–43}$$

Since this expression is a function of the overall mobility, the velocity saturation expression must be rearranged algebraically. The velocity saturation expression formulated by Canali is more easily rearranged, and is expressed for drift-diffusion and for hydrodynamic simulation as follows.

$$\mu(\vec{r}) = \frac{\mu_0(\vec{r})}{\left(1 + \left(\frac{\mu_0(\vec{r})E_{\parallel}(\vec{r})}{v_{sat}}\right)^{\beta}\right)^{1/\beta}} \tag{2–44}$$

$$\mu(\vec{r}) = \frac{\mu_0(\vec{r})}{\left(\sqrt{1+\frac{1}{4}\left(\frac{3}{2}\frac{\mu_0 k(T_n-T_L)}{q\tau_{E_n}v_{sat}^2}\right)^\beta} + \sqrt{\frac{1}{4}\left(\frac{3}{2}\frac{\mu_0 k(T_n-T_L)}{q\tau_{E_n}v_{sat}^2}\right)^\beta}\right)^{1/\beta}} \tag{2–45}$$

where β is typically chosen as 2 for electrons and 1 for holes.

2.2.3 Implementation-Specific Details

In the interest of using this mobility model for small-signal AC or impedance field noise simulation, it is important once again to note that *exact derivatives of the partial differential equations with respect to the solution variables are required.* The utility of the Alagator scripting format for FLOODS is that the equation parser knows how to take analytical derivatives of simple expressions. Therefore, the only primary concern is that of computing the transverse electric field, which is not a flux term but depends on the potential at more than two nodes. This problem has been addressed by modifying FLOODS to allow the assembly of the Jacobian matrix by triangular faces or 3-D elements rather than by nodes and edges only.

An operator "`trans(a)`" has been written which computes the magnitude of the electric field perpendicular to mesh edges in an element, as a function of the potential at the other nodes in the element. A vector field is first computed for the element using the method of least-squares, as follows.

$$\begin{bmatrix} \sum_{i=1}^N x_i^2 & \sum x_i y_i & \sum x_i z_i & \sum x_i \\ \sum x_i y_i & \sum y_i^2 & \sum y_i z_i & \sum y_i \\ \sum x_i z_i & \sum y_i z_i & \sum z_i^2 & \sum z_i \\ \sum x_i & \sum y_i & \sum z_i & N \end{bmatrix} \begin{bmatrix} E_x \\ E_y \\ E_z \\ \psi|_{\vec{r}=0} \end{bmatrix} = \begin{bmatrix} x_1 & x_2 & \dots & x_N \\ y_1 & y_2 & \dots & y_N \\ z_1 & z_2 & \dots & z_N \\ 1 & 1 & \dots & 1 \end{bmatrix} \begin{bmatrix} \psi_1 \\ \vdots \\ \psi_N \end{bmatrix} \tag{2–46}$$

where N is the number of nodes in the element, and x_i, y_i, z_i, and ψ_i are the x, y, and z coordinates and potential at node i, respectively. The 4x4 matrix on the left hand side is inverted and multiplied by the 4xN matrix on the right hand side, and the first 3 rows are stored as a 3xN matrix which depends only on the geometry of the element and therefore only needs to be computed once per element. This matrix, multiplied by the Nx1 vector

of any solution variable's values at the N nodes to yield the x, y, and z components of the vector gradient for the element (E_x, E_y, and E_z, for psi as the argument). The component perpendicular to an edge is then computed as follows.

$$E_{\perp ij} = \sqrt{(1 - \Delta x_{ij}/l_{ij})E_x^2 + (1 - \Delta y_{ij}/l_{ij})E_y^2 + (1 - \Delta z_{ij}/l_{ij})E_z^2} \tag{2–47}$$

If it is desired to compute $E_\perp$ as the field perpendicular to the nearest interface rather than an edge, the same vector field for the element can be used, and the component is computed in the direction of the nearest interface node (in this case the result would be the same for each edge in the element).

2.3 Implementation of the Energy Balance Transport Equations in FLOODS

FLOODS uses the standard generalized box discretization technique to solve the PDEs which are specified in strings passed to the Alagator parser in Tcl scripts. The Sharfetter-Gummel discretization method [39] provides a numerically stable expression for any edge-evaluated flux of the form $\vec{f} = (x\nabla y - c\nabla x)$ where c is constant along the edge, y varies linearly along the edge, and x varies non-linearly. The electron flow in a drift-diffusion system $n\vec{V}_n$ in Equation 2–36 fits this form (and is indeed the expression this was originally derived for). The discretized flux along an edge between nodes i and j is then expressed as follows.

$$f_{ij} = \frac{c}{l_{ij}} \left[x_i B\left(\frac{(y_i - y_j)}{c}\right) - x_j B\left(\frac{-(y_i - y_j)}{c}\right)\right] \tag{2–48}$$

$B(z) = z/(exp(z) - 1)$ is the Bernoulli function. This expression has been used for drift diffusion transport, scripted as "`c*sgrad(x,y/c)`" but in the energy balance transport model the electron flow $n\vec{V}_n$ in Equation 2–32 includes the electron temperature T_n, which varies linearly across an edge. Fortunately, a Sharfetter-Gummel-like discretization has been derived [40] which provides a numerically stable expression for those fluxes where the

c term varies along the edge, expressed as follows.

$$f_{ij} = \frac{c_{if}}{l_{ij}} \left[x_i B \left(\frac{(y_i - y_j)}{c_{ij}} \right) - x_j B \left(\frac{-(y_i - y_j)}{c_{ij}} \right) \right] \tag{2–49}$$

$$c_{ij} = \frac{c_i - c_j}{\ln(c_i/c_j)} \tag{2–50}$$

An operator named "`hdsgrad(x,y,c)`" has been implemented which evaluates this discretized expression and provides its full and complete derivatives with respect to any arbitrary variable, provided (by FLOODS) the derivatives of the arguments with respect to the same arbitrary variable. The function f_{ij} can then be scripted as "`hdsgrad(x,y,c)`," and the electron flow in the energy balance formulation can be scripted as "`($mun/$q)*hdsgrad(Elec, $q*DevPsi-(1-$lamp)*($Un), $Un)`." "`$mun`" is the Tcl variable representing the electron mobiliy, "`$q`" is the fundamental charge, "`$Un`" is the electron thermal energy kT_n, "`Elec`" and "`DevPsi`" are n and ψ, respectively, and "`$lamp`" is from the value λ_{P_n} from the energy balance closure relations.

The electron heat flux $n\vec{S}_n$ is rearranged to follow this Sharfetter-Gummel like form as follows and similarly scripted.

$$n\vec{S}_n = \frac{\mu_{S_n}}{q} \left[\frac{5}{2} kT_n n \nabla \left(q\psi + (2\lambda_{Q_n} - 1)\frac{5}{2} kT_n \right) - \frac{5}{2} kT_n \nabla \left(\frac{5}{2} kT_n n \right) \right] \tag{2–51}$$

The Joule heating term $q\nabla\psi \cdot (n\vec{V}_n)$ is recast as $\nabla \cdot (q\psi n\vec{V}_n) - q\psi(\frac{dn}{dt} - G_n + R_n)$. The first term requires the vector $q\psi n\vec{V}_n$ to be computed along edges, and can be discretized by multiplying the particle flow expression by the average potential along the edge. This is scripted as "`Devpsi*$mun*hdsgrad(Elec, $q*DevPsi-(1-$lamp)*$Un, $Un)`."

Finally, the energy relaxation terms are observed to be problematic, particularly in depletion regions where the carrier density gets very small. To avoid these convergence problems, a small density (on the order of $10^3 cm^{-3}$) is added to the carrier density in the energy relaxation terms. This greatly improves the convergence by ensuring a very small but finite energy relaxation in depletion regions.

2.4 Impact Ionization

In order to accurately capture the floating body effect in SOI devices which gives rise to the excess noise [1], it is necessary to model the electron impact ionization which generates holes to elevate the bias of the floating body.

The most accurate methods of computing impact ionization rates involve direct solution of the Boltzmann Transport Equation, or indirect solution via Shockley's Lucky Electron model in order to accurately compute the number of carriers that have sufficient energy and momentum to excite an electron from the local distribution of valence band electrons to the conduction band. However, within the scope of this work (numerical simulation via BTE moments) some assumption must be made to model the impact ionization rate. Common assumptions are that the local electron distribution is functionally similar to the equilibrium distribution, displaced in energy, and that the displacement of this function in energy is related only to the local electric field. The first assumption is all that is required for simulation within the hydrodynamic or energy-balance models, as the energy displacement is directly related to the electron temperature. For drift-diffusion simulation it is necessary to do extra non-local computation such as shooting methods or lucky-electron post-processing to ascertain the kinetic energy of the carriers if the second assumption is not made. These methods are not necessarily appropriate for noise simulation, however, as the derivatives of these terms are not available for inclusion in the AC Jacobian matrix. This leaves us with the traditional assumption that the impact ionization rates can be modelled as a function of local electric field (parallel to current flow).

Since impact ionization is caused by a fraction of the carriers moving through a locality in the semiconductor, it's rate is usually modeled as follows.

$$\mathrm{G}_{II} = \alpha_n \vec{J}_n + \alpha_p \vec{J}_p \tag{2–52}$$

where α_n and α_p are the electron and hole impact ionization coefficients, respectively. In n-channel FETs, electron impact ionization dominates, and hole impact ionization is usually at most a second-order effect; the second term can generally be ignored (or the first term, in p-channel FETs). For long homogeneous semiconductors in which the carrier distribution is allowed to reach a quasi-equilibrium in a constant electric field [2], the coefficients are found to follow the Chynoweth relation [41], as used by van Overstraeten [42].

$$\alpha(E_{\parallel}) = Ae^{(-B/E_{\parallel})} \tag{2–53}$$

where A and B are fit parameters that have been previously characterized for the homogeneous field case.

The extension of this impact ionization model to energy-balance or hydrodynamic simulation involves the assumption that in a scaled device the relationship of impact ionization rate to average carrier kinetic energy is the same as that in a long semiconductor with homogeneous field (consistent with the previous assumptions). The equation relating a homogeneous electric field to carrier temperature (Equation 2–43) is used to derive the following relationship.

$$\alpha_n(T_n) = Ae^{\left(B\sqrt{\frac{2q\mu_n^*\tau_{E_n}}{3k(T_n-T_L)}}\right)} \tag{2–54}$$

Since in highly scaled devices the carrier distribution does not reach an equilibrium and in light of the assumptions made in deriving these expressions as well as the dependence on carrier energy on defect-related scattering rates, it is not expected that the parameters A and B should agree between accurately calibrated drift-diffusion and hydrodynamic models, nor should they necessarily agree with previously determined empirical values. Therefore, for the purposes of matching measurements to simulations in this work they are treated as fit parameters.

2.5 Impedance Field Simulation of Velocity Fluctuation Noise

The impedance field method has been used previously [26, 27] to simulate noise in semiconductor devices using FLOODS [43, 44]. Local noise fluctuations are modeled using first-principle physics and their mapping to the external circuit are computed using the Green's functions, which describe the effect of a small signal AC-fluctuation in one of the system's PDEs at an internal node on the potential or current at a contact.

To simulate physical fluctuation mechanisms using advanced transport models such as those in section 2.1, it is necessary to trace the fluctuation terms through their origins in the BTE (Eq. (2–2)) to each contribution to the system of equations. This is done for velocity fluctuation noise in the following section.

2.5.1 Velocity Fluctuation Noise Simulation

Velocity fluctuations are caused by intraband transitions of particles from one momentum state to another due to collisions with phonons, randomly located ionized impurities, and other particles. Electrons scatter, gaining or losing momentum. Microscopically, the collision term of the BTE can be described by a statistical mean component and a stochastic component, which fluctuates randomly and with a zero statistical mean.

$$\frac{\partial f}{\partial t}\Big|_{Coll}(\vec{p}) = \sum_{p'} \left(\frac{\phi(\vec{p}')}{\phi(\vec{p})} - 1 \right) S(\vec{p}, \vec{p}') f(\vec{p}) + \gamma_f = -\frac{f(\vec{p})}{\tau(\vec{p})} + \gamma_f \tag{2–55}$$

where γ_f is a Langevin noise source which represents a fluctuation in $\frac{\partial f}{\partial t}\Big|_{Coll}$. These fluctuations can also be characterized by a fluctuation over a short time τ in the average electron and hole velocities around a statistical mean value.

$$\vec{V}_n = \frac{1}{n} \sum_p \vec{v} f = \overline{\vec{V}_n} + \frac{1}{n} \sum_p \vec{v} \gamma_f \tau = \overline{\vec{V}_n} + \vec{\gamma}_{v_n} \tau \tag{2–56}$$

Since these fluctuations are caused by collisions with phonons and other particles, their associated Langevin noise sources are inserted into the system's partial differential equations through those terms derived from the collision term of the BTE (Eq. (2–2)). This should be considered for each moment individually. For the zeroeth-order moment,

the collision term of the BTE is zero, since for every collision a positive $\partial f/\partial t$ at one momentum $\vec{p}$ is offset by an equal negative $\partial f/\partial t$ at a different momentum $\vec{p}'$. For the first-order moment, the collision term is characterized as follows.

$$\frac{1}{\Omega}\sum_p \vec{p}\frac{\partial f}{\partial t}\Big|_{coll} = n\vec{C}_{P_n} + \frac{1}{\Omega}\sum_p \vec{p}\gamma_f = -n\left(\frac{\vec{P}_n}{\langle\tau_{P_n}\rangle} - \lambda_{P_n}\nabla(kT_n)\right) + m_n^* n\vec{\gamma}_{v_n} \tag{2–57}$$

For the second-order moment, this term is characterized as follows.

$$\frac{1}{\Omega}\sum_p \frac{|\vec{p}|^2}{2m_n^*}\frac{\partial f}{\partial t}\Big|_{coll} = nC_{E_n} + \frac{1}{\Omega}\sum_p \frac{|\vec{p}|^2}{2m_n^*}\gamma_f = -\frac{3}{2}nk\frac{T_n - T_L}{\langle\tau_{W_n}\rangle} + n\gamma_{w_n} \tag{2–58}$$

If the collisions are considered to be nearly elastic such that $|\vec{p}| \approx |\vec{p}'|$, γ_{w_n} can be assumed to be zero. For the third-order moment, this term is characterized as follows.

$$\frac{1}{\Omega}\sum_p \frac{|\vec{p}|^2}{2m_n^*}\vec{p}\frac{\partial f}{\partial t}\Big|_{coll} = n\vec{C}_{Q_n} + \frac{1}{\Omega}\sum_p \frac{|\vec{p}|^2}{2m_n^*}\vec{p}\gamma_f = -n\left(\frac{\vec{Q}_n}{\langle\tau_{Q_n}\rangle} - \lambda_{Q_n}\nabla(\frac{5}{2}k^2T_n^2)\right) + m_n^* n\vec{\gamma}_{s_n} \tag{2–59}$$

By examination of the derivation of the third-order moment, compared to the derivation of the first-order moment, it becomes obvious that $\vec{\gamma}_{s_n}$ can be related to $\vec{\gamma}_{v_n}$ as follows.

$$\vec{\gamma}_{s_n} = \frac{5}{2}kT_n\vec{\gamma}_{v_n} \tag{2–60}$$

Therefore, the velocity fluctuation Langevin sources $\vec{\gamma}_{v_n}$ and $\vec{\gamma}_{v_p}$ enter the system of equations derived from the first four moments of the BTE as follows. Note that the asterisks to denote effective masses and mobilities are omitted so they will not be confused

with complex conjugates in the later phasor expressions.

$$\nabla^2\psi = -\frac{q}{\epsilon}(p - n + N_D^+ - N_A^-) - \frac{\rho_t}{\epsilon}$$

$$\frac{dn}{dt} = -\nabla\cdot(n\vec{V}_n) + \mathrm{G}_n - \mathrm{R}_n$$

$$\frac{dp}{dt} = -\nabla\cdot(p\vec{V}_p) + \mathrm{G}_p - \mathrm{R}_p$$

$$m_n\frac{d(n\vec{V}_n)}{dt} = -\nabla(nkT_n) - qn\vec{E} - n\left(\frac{q\vec{V}_n}{\mu_n} - \lambda_{P_n}\nabla(kT_n)\right) + m_n n\vec{\gamma}_{v_n} \tag{2–61}$$

$$m_p\frac{d(p\vec{V}_p)}{dt} = -\nabla(pkT_p) + qp\vec{E} - p\left(\frac{q\vec{V}_p}{\mu_p} - \lambda_{P_p}\nabla(kT_p)\right) + m_p p\vec{\gamma}_{v_p} \tag{2–62}$$

$$\frac{3}{2}k\frac{d(nT_n)}{dt} = -\nabla\cdot(n\vec{S}_n) - q\vec{E}\cdot(n\vec{V}_n) + \mathrm{G}_{W_n} - \mathrm{R}_{W_n} - \frac{3}{2}nk\frac{T_n - T_L}{\langle\tau_{W_n}\rangle}$$

$$\frac{3}{2}k\frac{d(pT_p)}{dt} = -\nabla\cdot(p\vec{S}_p) + q\vec{E}\cdot(p\vec{V}_p) + \mathrm{G}_{W_p} - \mathrm{R}_{W_p} - \frac{3}{2}pk\frac{T_p - T_L}{\langle\tau_{W_p}\rangle}$$

$$m_n\frac{d(n\vec{S}_n)}{dt} = -\nabla\Big(\frac{5}{2}nk^2T_n^2\Big) - q\vec{E}\Big(\frac{5}{2}nkT_n\Big) - n\left(\frac{q\vec{S}_n}{\mu_{S_n}} - \lambda_{Q_n}\nabla\Big(\frac{5}{2}k^2T_n^2\Big)\right) + \frac{5}{2}kT_n m_n n\vec{\gamma}_{v_n} \tag{2–63}$$

$$m_p\frac{d(p\vec{S}_p)}{dt} = -\nabla\Big(\frac{5}{2}pk^2T_p^2\Big) + q\vec{E}\Big(\frac{5}{2}pkT_p\Big) - p\left(\frac{q\vec{S}_p}{\mu_{S_p}} - \lambda_{Q_p}\nabla\Big(\frac{5}{2}k^2T_p^2\Big)\right) + \frac{5}{2}kT_p m_p p\vec{\gamma}_{v_p} \tag{2–64}$$

The fluctuation of voltage $\tilde{V}_c$ at the considered external contact is then given as follows.

$$\tilde{V}_c = \iiint_r \left(\begin{array}{l}\vec{G}_{P_n}\cdot(m_n n\vec{\gamma}_{v_n}) + \vec{G}_{P_p}\cdot(m_p p\vec{\gamma}_{v_p}) \\ \qquad + \vec{G}_{Q_n}\cdot\Big(\frac{5}{2}kT_n m_n n\vec{\gamma}_{v_n}\Big) + \vec{G}_{Q_p}\cdot\Big(\frac{5}{2}kT_p m_p p\vec{\gamma}_{v_p}\Big)\end{array}\right) d^3r \tag{2–65}$$

where $\vec{G}_{P_n}$, $\vec{G}_{P_p}$, $\vec{G}_{Q_n}$ and $\vec{G}_{Q_p}$ are the Green's functions associated with the vector-valued electron and hole momentum balance equations and electron and hole heat flow balance equations, respectively. The power spectral density $S_V = 2T\overline{\tilde{V}_c^*\tilde{V}_c}$ is computed as follows.

$$S_V = 2T\overline{\iiint_{r_i}\left(\begin{array}{l}\vec{G}^*_{P_n}\cdot(m_n n\vec{\gamma}^*_{v_n}) + \ldots \\ \ldots\vec{G}^*_{Q_p}\cdot\Big(\frac{5}{2}kT_p m_p p\vec{\gamma}^*_{v_p}\Big)\end{array}\right) d^3r_i \iiint_{r_j}\left(\begin{array}{l}\vec{G}_{P_n}\cdot(m_n n\vec{\gamma}_{v_n}) + \ldots \\ \ldots\vec{G}_{Q_p}\cdot\Big(\frac{5}{2}kT_p m_p p\vec{\gamma}_{v_p}\Big)\end{array}\right) d^3r_j} \tag{2–66}$$

where T is the length of the time window of the measurement. If the implicit approximation is made that the noise sources $\vec{\gamma}_{v_n}$ and $\vec{\gamma}_{v_p}$ are statistically independent in position, the following approximation can be made.

$$2T\overline{\vec{\gamma}^*_{v_n}(\vec{r}_i)\vec{\gamma}_{v_n}(\vec{r}_j)} = \hat{K}_{v_n v_n}\delta(\vec{r}_i - \vec{r}_j) \tag{2–67}$$

where $\hat{K}_{v_n v_n}$ is the local noise strength tensor of electron velocity fluctuations, and $\delta(\vec{r})$ is the Dirac delta function. The local noise strengths can be evaluated using Monte Carlo computations to directly compute the various local noise strength tensors as Fourier transforms of the velocity-velocity, velocity-energy and energy-energy correlation functions, as has been shown previously [32, 45, 46]. The advantage of this is that γ_{w_n} and γ_{w_p} can be computed for inelastic scattering mechanisms without any further physical modeling. The downside is that the Monte-Carlo computations can only be feasibly performed at RF frequencies and higher. An alternative method to evaluate these expressions is using the local noise strength spectral tensors that follow, consistent with Milatz' theorem.

$$\hat{K}_{v_n v_n} = \frac{4D_n}{n\langle\tau_{P_n}\rangle^2}\hat{I} \tag{2–68}$$

$$\hat{K}_{v_p v_p} = \frac{4D_p}{p\langle\tau_{P_p}\rangle^2}\hat{I} \tag{2–69}$$

$$\overline{\vec{\gamma}^*_{v_n}(\vec{r}_i)\vec{\gamma}_{v_p}(\vec{r}_j)} = \overline{\vec{\gamma}^*_{v_p}(\vec{r}_i)\vec{\gamma}_{v_n}(\vec{r}_j)} = 0 \tag{2–70}$$

where D_n and D_p are the electron and hole diffusivities. These diffusivities are typically modeled using Einstein's relation $\frac{D}{\mu} = \frac{kT}{q}$ with either the carrier temperatures or the lattice temperature. Recent work [45] has shown that neither temperature gives strictly accurate local noise strengths, but that the correctly computed values, using the Fourier transform of the velocity autocorrelation function computed from Monte Carlo simulations, is somewhere in between the lattice and carrier temperatures. The published figures of that work suggest that using an average of the two temperatures will be closer than using either one, and this is satisfying since the scattering process involves collisions

between carriers (characterized by the carrier temperature) and phonons (characterized by the lattice temperature).

With the $\overline{\vec{\gamma}^*\vec{\gamma}}$ terms modeled as above, the power spectral density expression can then be simplified as follows.

$$S_V = \iiint_r \left(\begin{array}{c} m_n^2 n^2 \vec{G}^*_{P_n} \cdot \hat{K}_{v_n v_n} \cdot \vec{G}_{P_n} + \frac{5}{2} k T_n m_n^2 n^2 \vec{G}_{P_n^*} \cdot \hat{K}_{v_n v_n} \cdot \vec{G}_{Q_n} + \ldots \\ \ldots + \frac{5}{2} k T_p m_p^2 p^2 \vec{G}^*_{Q_p} \cdot \hat{K}_{v_p v_p} \cdot \vec{G}_{P_p} + \frac{25}{4} k^2 T_p^2 m_p^2 p^2 \vec{G}^*_{Q_p} \cdot \hat{K}_{v_p v_p} \cdot \vec{G}_{Q_p} \end{array} \right) d^3 r \tag{2–71}$$

As mentioned previously, this complete four-moment BTE-based system of equations is not typically solved due to its complexity, so for the simpler transport models the Langevin noise source terms must be appropriately folded into the remaining PDEs.

2.5.1.1 Hydrodynamic model with velocity fluctuation noise

To correctly place the Langevin noise terms in the hydrodynamic model, the Langevin terms are folded into the remaining PDEs from the heat flow balance equations. First the quasi-stationary expressions for the carrier heat flows are rearranged as follows.

$$\vec{S}_n = -\frac{\mu_{S_n}}{q} \left[\frac{5}{2} k T_n q \vec{E} + \frac{5}{2} k^2 T_n^2 \frac{\nabla n}{n} + (1 - \lambda_{Q_n}) \nabla \left(\frac{5}{2} k^2 T_n^2 \right) \right] + \frac{5}{2} k T_n \langle \tau_{Q_n} \rangle \vec{\gamma}_{v_n} = \overline{\vec{S}_n} - \frac{\vec{\xi}_{s_n}}{n} \tag{2–72}$$

$$\vec{S}_p = -\frac{\mu_{S_p}}{q} \left[-\frac{5}{2} k T_p q \vec{E} + \frac{5}{2} k^2 T_p^2 \frac{\nabla p}{p} + (1 - \lambda_{Q_p}) \nabla \left(\frac{5}{2} k^2 T_p^2 \right) \right] + \frac{5}{2} k T_p \langle \tau_{Q_p} \rangle \vec{\gamma}_{v_p} = \overline{\vec{S}_p} + \frac{\vec{\xi}_{s_p}}{p} \tag{2–73}$$

where $\vec{\xi}_{s_n} = -\frac{5}{2} k T_n \frac{\mu_{S_n}}{\mu_n} \langle \tau_{P_n} \rangle n \vec{\gamma}_{v_n}$ and $\vec{\xi}_{s_p} = \frac{5}{2} k T_p \frac{\mu_{S_p}}{\mu_p} \langle \tau_{P_p} \rangle p \vec{\gamma}_{v_p}$ are the Langevin terms recast as fluctuators for the total carrier heat flow $-n\vec{S}_n$ or $p\vec{S}_p$.

The hydrodynamic system of equations with velocity fluctuation Langevin noise sources can then be expressed as follows.

$$
\begin{aligned}
\nabla^2\psi &= -\frac{q}{\epsilon}(p - n + N_D^+ - N_A^-) - \frac{\rho_t}{\epsilon} \\
\frac{dn}{dt} &= -\nabla\cdot(n\vec{V}_n) + \mathrm{G}_n - \mathrm{R}_n \\
\frac{dp}{dt} &= -\nabla\cdot(p\vec{V}_p) + \mathrm{G}_p - \mathrm{R}_p \\
m_n\frac{d(n\vec{V}_n)}{dt} &= -\nabla(nkT_n) - qn\vec{E} - n\left(\frac{q\vec{V}_n}{\mu_n} - \lambda_{P_n}\nabla(kT_n)\right) + m_n n\vec{\gamma}_{v_n} \\
m_p\frac{d(p\vec{V}_p)}{dt} &= -\nabla(pkT_p) + qp\vec{E} - p\left(\frac{q\vec{V}_p}{\mu_p} - \lambda_{P_p}\nabla(kT_p)\right) + m_p p\vec{\gamma}_{v_p} \\
\frac{3}{2}k\frac{d(nT_n)}{dt} &= -\nabla\cdot(n\overline{\vec{S}_n}) - q\vec{E}\cdot(n\vec{V}_n) + \mathrm{G}_{W_n} - \mathrm{R}_{W_n} - \frac{3}{2}nk\frac{T_n - T_L}{\langle\tau_{W_n}\rangle} + \nabla\cdot(\vec{\xi}_{s_n}) \qquad (2\text{–}74) \\
\frac{3}{2}k\frac{d(pT_p)}{dt} &= -\nabla\cdot(p\overline{\vec{S}_p}) + q\vec{E}\cdot(p\vec{V}_p) + \mathrm{G}_{W_p} - \mathrm{R}_{W_p} - \frac{3}{2}pk\frac{T_p - T_L}{\langle\tau_{W_p}\rangle} - \nabla\cdot(\vec{\xi}_{s_p}) \qquad (2\text{–}75) \\
\overline{\vec{S}_n} &= -\frac{\mu_{S_n}}{q}\left[\frac{5}{2}kT_n q\vec{E} + \frac{5}{2}k^2T_n^2\frac{\nabla n}{n} + (1-\lambda_{Q_n})\nabla\left(\frac{5}{2}k^2T_n^2\right)\right] \\
\overline{\vec{S}_p} &= -\frac{\mu_{S_p}}{q}\left[-\frac{5}{2}kT_p q\vec{E} + \frac{5}{2}k^2T_p^2\frac{\nabla p}{p} + (1-\lambda_{Q_p})\nabla\left(\frac{5}{2}k^2T_p^2\right)\right]
\end{aligned}
$$

The fluctuation of voltage at the considered external contact is then given as follows.

$$
\tilde{V}_c = \iiint_r \left(\vec{G}_{P_n}\cdot(m_n n\vec{\gamma}_{v_n}) + \vec{G}_{P_p}\cdot(m_p p\vec{\gamma}_{v_p}) + (\nabla G_{E_n})\cdot(\vec{\xi}_{s_n}) - (\nabla G_{E_p})\cdot(\vec{\xi}_{s_p})\right) d^3r \qquad (2\text{–}76)
$$

where G_{E_n} and G_{E_p} are the scalar-valued Green's functions associated with the electron and hole energy balance equations, respectively. The power spectral density of the noise at the contact is given as follows.

$$
S_V = 2T\overline{\iiint_{r_i}\begin{pmatrix}\vec{G}^*_{P_n}\cdot(m_n n\vec{\gamma}^*_{v_n}) + \dots \\ \dots - (\nabla G_{E_p})^*\cdot(\vec{\xi}_{s_p})^*\end{pmatrix} d^3r_i \iiint_{r_j}\begin{pmatrix}\vec{G}_{P_n}\cdot(m_n n\vec{\gamma}_{v_n}) + \dots \\ \dots - (\nabla G_{E_p})\cdot(\vec{\xi}_{s_p})\end{pmatrix} d^3r_j} \qquad (2\text{–}77)
$$

The additional local noise spectral tensors can be expressed as follows, in accordance with Milatz' theorem, as in the previous section.

$$\overline{\vec{\gamma}^*_{v_n}(\vec{r}_i)\vec{\xi}_{S_n}(\vec{r}_j)} = \overline{\vec{\xi}^*_{S_n}(\vec{r}_i)\vec{\gamma}_{v_n}(\vec{r}_j)} = -10kT_n\frac{\mu_{S_n}}{\mu_n}\frac{D_n}{\langle\tau_{P_n}\rangle}\hat{I}\frac{\delta(\vec{r}_i-\vec{r}_j)}{2T} = \hat{K}_{v_nS_n}\frac{\delta(\vec{r}_i-\vec{r}_j)}{2T} \quad (2\text{–}78)$$

$$\overline{\vec{\gamma}^*_{v_p}(\vec{r}_i)\vec{\xi}_{S_p}(\vec{r}_j)} = \overline{\vec{\xi}^*_{S_p}(\vec{r}_i)\vec{\gamma}_{v_p}(\vec{r}_j)} = 10kT_p\frac{\mu_{S_p}}{\mu_p}\frac{D_p}{\langle\tau_{P_p}\rangle}\hat{I}\frac{\delta(\vec{r}_i-\vec{r}_j)}{2T} = \hat{K}_{v_pS_p}\frac{\delta(\vec{r}_i-\vec{r}_j)}{2T} \quad (2\text{–}79)$$

$$\overline{\vec{\gamma}^*_{v_\alpha}(\vec{r}_i)\vec{\xi}_{S_\beta}(\vec{r}_j)} = \overline{\vec{\xi}^*_{S_\beta}(\vec{r}_i)\vec{\gamma}_{v_\alpha}(\vec{r}_j)} = 0 \quad (2\text{–}80)$$

$$\overline{\vec{\xi}^*_{S_n}(\vec{r}_i)\vec{\xi}_{S_n}(\vec{r}_j)} = 25k^2T_n^2\frac{\mu_{S_n}^2}{\mu_n^2}D_n n\hat{I}\frac{\delta(\vec{r}_i-\vec{r}_j)}{2T} = \hat{K}_{S_nS_n}\frac{\delta(\vec{r}_i-\vec{r}_j)}{2T} \quad (2\text{–}81)$$

$$\overline{\vec{\xi}^*_{S_p}(\vec{r}_i)\vec{\xi}_{S_p}(\vec{r}_j)} = 25k^2T_p^2\frac{\mu_{S_p}^2}{\mu_p^2}D_p p\hat{I}\frac{\delta(\vec{r}_i-\vec{r}_j)}{2T} = \hat{K}_{S_pS_p}\frac{\delta(\vec{r}_i-\vec{r}_j)}{2T} \quad (2\text{–}82)$$

$$\overline{\vec{\xi}^*_{S_n}(\vec{r}_i)\vec{\xi}_{S_p}(\vec{r}_j)} = \overline{\vec{\xi}^*_{S_p}(\vec{r}_i)\vec{\xi}_{S_n}(\vec{r}_j)} = 0 \quad (2\text{–}83)$$

where α represents either n or p, and β represents the opposite choice. This results in the following simplified expression for S_V.

$$S_V = \iiint_r \begin{pmatrix} m_n^2n^2\vec{G}^*_{P_n}\cdot\hat{K}_{v_nv_n}\cdot\vec{G}_{P_n} + m_nn\vec{G}^*_{P_n}\cdot\hat{K}_{v_nS_n}\cdot(\nabla G_{E_n}) + \dots \\ \dots - m_pp(\nabla G_{E_p})^*\cdot\hat{K}_{v_pS_p}\cdot\vec{G}_{P_p} + (\nabla G_{E_p})^*\cdot\hat{K}_{S_pS_p}\cdot(\nabla G_{E_p}) \end{pmatrix} d^3r \quad (2\text{–}84)$$

This type of impedance field noise simulation has been performed previously as in [32, 46] and has been referred to as "acceleration fluctuation" noise since the noise sources appear opposite the $\frac{d(n\vec{V}_n)}{dt}$ terms.

2.5.1.2 Energy balance model with velocity fluctuation noise

To correctly place the Langevin noise terms in the energy balance model, the Langevin terms are folded into the remaining PDEs from the momentum balance equations. First the stationary expressions for the carrier velocities are rearranged as follows.

$$\vec{V}_n = -\frac{\mu_n}{q}\left[q\vec{E} + kT_n\frac{\nabla n}{n} + (1-\lambda_{P_n})\nabla(kT_n)\right] + \langle\tau_{P_n}\rangle\vec{\gamma}_{v_n} = \overline{\vec{V}_n} - \frac{\vec{\xi}_n}{qn} \quad (2\text{–}85)$$

$$\vec{V}_p = -\frac{\mu_p}{q}\left[-q\vec{E} + kT_p\frac{\nabla p}{p} + (1-\lambda_{P_p})\nabla(kT_p)\right] + \langle\tau_{P_p}\rangle\vec{\gamma}_{v_p} = \overline{\vec{V}_p} + \frac{\vec{\xi}_p}{qp} \quad (2\text{–}86)$$

where $\vec{\xi}_n = -qn\langle\tau_{P_n}\rangle\vec{\gamma}_{v_n}$ and $\vec{\xi}_p = qp\langle\tau_{P_p}\rangle\vec{\gamma}_{v_p}$ are the Langevin terms recast as fluctuators for the total carrier current density $\vec{J}_n = -qn\vec{V}_n$ or $\vec{J}_p = qp\vec{V}_p$. The total carrier heat flow fluctuators can be expressed relative to the current density fluctuators as $\vec{\xi}_{S_n} = \left(\frac{5}{2}\frac{kT_n}{q}\frac{\mu_{S_n}}{\mu_n}\right)\vec{\xi}_n$ and $\vec{\xi}_{S_p} = \left(\frac{5}{2}\frac{kT_p}{q}\frac{\mu_{S_p}}{\mu_p}\right)\vec{\xi}_p$. The energy balance model's system of equations with velocity fluctuation Langevin noise sources can then be expressed as follows.

$$\nabla^2\psi = -\frac{q}{\epsilon}(p - n + N_D^+ - N_A^-) - \frac{\rho_t}{\epsilon}$$

$$\frac{dn}{dt} = -\nabla\cdot(n\overline{\vec{V}_n}) + \mathrm{G}_n - \mathrm{R}_n + \frac{1}{q}\nabla\cdot(\vec{\xi}_n) \tag{2–87}$$

$$\frac{dp}{dt} = -\nabla\cdot(p\overline{\vec{V}_p}) + \mathrm{G}_p - \mathrm{R}_p - \frac{1}{q}\nabla\cdot(\vec{\xi}_p) \tag{2–88}$$

$$\overline{\vec{V}_n} = -\frac{\mu_n}{q}\left[q\vec{E} + kT_n\frac{\nabla n}{n} + (1-\lambda_{P_n})\nabla(kT_n)\right]$$

$$\vec{V}_p = -\frac{\mu_p}{q}\left[-q\vec{E} + kT_p\frac{\nabla p}{p} + (1-\lambda_{P_p})\nabla(kT_p)\right]$$

$$\frac{3}{2}k\frac{d(nT_n)}{dt} = -\nabla\cdot(n\overline{\vec{S}_n}) + q\nabla\cdot(\psi n\overline{\vec{V}_n}) + q\psi\Big(\frac{dn}{dt} - \mathrm{G}_n + \mathrm{R}_n\Big) + \mathrm{G}_{W_n} - \mathrm{R}_{W_n} - \frac{3}{2}nk\frac{T_n - T_L}{\langle\tau_{W_n}\rangle} + \nabla\cdot(\vec{\xi}_{s_n}) - \nabla\cdot(\psi\vec{\xi}_n) \tag{2–89}$$

$$\frac{3}{2}k\frac{d(pT_p)}{dt} = -\nabla\cdot(p\overline{\vec{S}_p}) - q\nabla\cdot(\psi p\overline{\vec{V}_p}) - q\psi\Big(\frac{dp}{dt} - \mathrm{G}_p + \mathrm{R}_p\Big) + \mathrm{G}_{W_p} - \mathrm{R}_{W_p} - \frac{3}{2}pk\frac{T_p - T_L}{\langle\tau_{W_p}\rangle} - \nabla\cdot(\vec{\xi}_{s_p}) + \nabla\cdot(\psi\vec{\xi}_p) \tag{2–90}$$

$$\overline{\vec{S}_n} = -\frac{\mu^*_{S_n}}{q}\left[\frac{5}{2}kT_nq\vec{E} + \frac{5}{2}k^2T_n^2\frac{\nabla n}{n} + (1-\lambda_{Q_n})\nabla\Big(\frac{5}{2}k^2T_n^2\Big)\right]$$

$$\overline{\vec{S}_p} = -\frac{\mu^*_{S_p}}{q}\left[-\frac{5}{2}kT_pq\vec{E} + \frac{5}{2}k^2T_p^2\frac{\nabla p}{p} + (1-\lambda_{Q_p})\nabla\Big(\frac{5}{2}k^2T_p^2\Big)\right]$$

The fluctuation of voltage at the considered external contact is then given as follows.

$$\tilde{V}_c = \iiint_r \left(\frac{1}{q}\nabla G_n\cdot\vec{\xi}_n - \frac{1}{q}\nabla G_p\cdot\vec{\xi}_p + \nabla G_{E_n}\cdot(\vec{\xi}_{s_n} - \psi\vec{\xi}_n) - \nabla G_{E_p}\cdot(\vec{\xi}_{s_p} - \psi\vec{\xi}_p)\right)d^3r \tag{2–91}$$

where G_n and G_p are the scalar-valued Green's functions associated with the electron and hole continuity equations, respectively. The power spectral density of the noise at the

contact is given as follows.

$$S_V = 2T \overline{\iiint_{r_i} \begin{pmatrix} \frac{1}{q}\nabla G_n^* \cdot \vec{\xi}_n^* - \dots \\ \dots - \nabla G_{E_p}^* \cdot (\vec{\xi}_{s_p}^* - \psi \xi_p^*) \end{pmatrix} d^3 r_i \iiint_{r_j} \begin{pmatrix} \frac{1}{q}\nabla G_n \cdot \vec{\xi}_n - \dots \\ \dots - (\nabla G_{E_p}) \cdot (\vec{\xi}_{s_p} - \psi \xi_p) \end{pmatrix} d^3 r_j} \tag{2–92}$$

The additional local noise strength spectral tensors can be expressed as follows, also in accordance with Milatz' theorem as in the previous sections.

$$\overline{\vec{\xi}_n^*(\vec{r}_i)\vec{\xi}_n(\vec{r}_j)} = 4q^2 n D_n \hat{I} \frac{\delta(\vec{r}_i - \vec{r}_j)}{2T} = \hat{K}_{j_n j_n} \frac{\delta(\vec{r}_i - \vec{r}_j)}{2T} \tag{2–93}$$

$$\overline{\vec{\xi}_p^*(\vec{r}_i)\vec{\xi}_p(\vec{r}_j)} = 4q^2 p D_p \hat{I} \frac{\delta(\vec{r}_i - \vec{r}_j)}{2T} = \hat{K}_{j_p j_p} \frac{\delta(\vec{r}_i - \vec{r}_j)}{2T} \tag{2–94}$$

$$\overline{\vec{\xi}_n^*(\vec{r}_i)\vec{\xi}_p(\vec{r}_j)} = \overline{\vec{\xi}_p^*(\vec{r}_i)\vec{\xi}_n(\vec{r}_j)} = 0 \tag{2–95}$$

$$\overline{\vec{\xi}_n^*(\vec{r}_i)\vec{\xi}_{S_n}(\vec{r}_j)} = 10\frac{kT_n}{q}\frac{\mu_{S_n}}{\mu_n} q^2 n D_n \hat{I} \frac{\delta(\vec{r}_i - \vec{r}_j)}{2T} = \hat{K}_{j_n S_n} \frac{\delta(\vec{r}_i - \vec{r}_j)}{2T} \tag{2–96}$$

$$\overline{\vec{\xi}_p^*(\vec{r}_i)\vec{\xi}_{S_p}(\vec{r}_j)} = 10\frac{kT_p}{q}\frac{\mu_{S_p}}{\mu_p} q^2 p D_p \hat{I} \frac{\delta(\vec{r}_i - \vec{r}_j)}{2T} = \hat{K}_{j_p S_p} \frac{\delta(\vec{r}_i - \vec{r}_j)}{2T} \tag{2–97}$$

$$\overline{\vec{\xi}_\alpha^*(\vec{r}_i)\vec{\xi}_{S_\beta}(\vec{r}_j)} = \overline{\vec{\xi}_{S_\beta}^*(\vec{r}_i)\vec{\xi}_\alpha(\vec{r}_j)} = 0 \tag{2–98}$$

$$\overline{\vec{\xi}_{S_n}^*(\vec{r}_i)\vec{\xi}_{S_n}(\vec{r}_j)} = 25k^2 T_n^2 \frac{\mu_{S_n}^2}{\mu_n^2} D_n n \hat{I} \frac{\delta(\vec{r}_i - \vec{r}_j)}{2T} = \hat{K}_{S_n S_n} \frac{\delta(\vec{r}_i - \vec{r}_j)}{2T}$$

$$\overline{\vec{\xi}_{S_p}^*(\vec{r}_i)\vec{\xi}_{S_p}(\vec{r}_j)} = 25k^2 T_p^2 \frac{\mu_{S_p}^2}{\mu_p^2} D_p p \hat{I} \frac{\delta(\vec{r}_i - \vec{r}_j)}{2T} = \hat{K}_{S_p S_p} \frac{\delta(\vec{r}_i - \vec{r}_j)}{2T}$$

$$\overline{\vec{\xi}_{S_n}^*(\vec{r}_i)\vec{\xi}_{S_p}(\vec{r}_j)} = \overline{\vec{\xi}_{S_p}^*(\vec{r}_i)\vec{\xi}_{S_n}(\vec{r}_j)} = 0$$

It is important to note that since $\vec{\xi}_n$, $\vec{\xi}_p$, $\vec{\xi}_{S_n}$, and $\vec{\xi}_{S_p}$ originate in the same collision term of the BTE (Eq. (2–2)) as $\vec{\gamma}_{v_n}$ in the acceleration fluctuation scheme, the approximation that these sources are statistically independent of position has not lost any validity, and this model is as accurate relative to the acceleration scheme as the quasi-stationary approximation for $\vec{V}_n$ and $\vec{V}_p$ are appropriate. While the fluctuation in velocity of a single carrier flowing through a semiconductor (as in Monte Carlo computation) may be correlated over short distances, the fluctuations in average carrier distribution velocity $\vec{V}_n$ are not.

The above relations give the following simplified expression for the power spectral density.

$$S_V = \iiint\limits_r \left(\begin{array}{l} \frac{1}{q^2}\nabla G_n^* \cdot \hat{K}_{j_n j_n} \cdot \nabla G_n + \frac{1}{q}\nabla G_n^* \cdot (\hat{K}_{j_n S_n} - \psi \hat{K}_{j_n j_n}) \cdot \nabla G_{E_n} + \ldots \\ \ldots + \nabla G_{E_p}^* \cdot (\hat{K}_{S_p S_p} - 2\psi \hat{K}_{j_p S_p} + \psi^2 \hat{K}_{j_p j_p}) \cdot \nabla G_{E_p} \end{array} \right) d^3 r \quad (2\text{–}99)$$

2.5.1.3 Drift-diffusion model with velocity fluctuation noise

The placement of the Langevin noise terms in the drift-diffusion model is well known, and is easily obtained from the previous formulation simply by ignoring the energy balance and heat flow balance equations and taking T_n and T_p as T_L. The drift-diffusion model's system of equations with velocity fluctuation Langevin noise sources can then be expressed as follows.

$$\begin{aligned} \nabla^2 \psi &= -\frac{q}{\epsilon}(p - n + N_D^+ - N_A^-) - \frac{\rho_t}{\epsilon} \\ \frac{dn}{dt} &= -\nabla \cdot (n\overline{\vec{V_n}}) + \mathrm{G}_n - \mathrm{R}_n + \frac{1}{q}\nabla \cdot (\vec{\xi_n}) \\ \frac{dp}{dt} &= -\nabla \cdot (p\overline{\vec{V_p}}) + \mathrm{G}_p - \mathrm{R}_p - \frac{1}{q}\nabla \cdot (\vec{\xi_p}) \\ \overline{\vec{V_n}} &= -\frac{\mu_n}{q}\left[q\vec{E} + kT_n\frac{\nabla n}{n} + (1 - \lambda_{P_n})\nabla(kT_L)\right] \\ \overline{\vec{V_p}} &= -\frac{\mu_p}{q}\left[-q\vec{E} + kT_p\frac{\nabla p}{p} + (1 - \lambda_{P_p})\nabla(kT_L)\right] \end{aligned}$$

The fluctuation of voltage at the considered external contact is then given as follows.

$$\tilde{V}_c = \iiint\limits_r \left(\frac{1}{q}\nabla G_n \cdot \vec{\xi_n} - \frac{1}{q}\nabla G_p \cdot \vec{\xi_p} \right) d^3 r \quad (2\text{–}100)$$

The power spectral density of the noise at the contact is given as follows.

$$S_V = 2T \overline{\iiint\limits_{r_i} \left(\frac{1}{q}\nabla G_n^* \cdot \vec{\xi_n^*} - \frac{1}{q}\nabla G_p^* \cdot \vec{\xi_p^*} \right) d^3 r_i \iiint\limits_{r_j} \left(\frac{1}{q}\nabla G_n \cdot \vec{\xi_n} - \frac{1}{q}\nabla G_p \cdot \vec{\xi_p} \right) d^3 r_j} \quad (2\text{–}101)$$

This expression is evaluated using Milatz' theorem which gives the following local noise strength spectral tensors, as shown previously.

$$\overline{\vec{\xi}_n^*(\vec{r}_i)\vec{\xi}_n(\vec{r}_j)} = (4q^2 D_n n)\hat{I}\frac{\delta(\vec{r}_i - \vec{r}_j)}{2T} = \hat{K}_{j_n j_n}\frac{\delta(\vec{r}_i - \vec{r}_j)}{2T}$$
$$\overline{\vec{\xi}_p^*(\vec{r}_i)\vec{\xi}_p(\vec{r}_j)} = (4q^2 D_p p)\hat{I}\frac{\delta(\vec{r}_i - \vec{r}_j)}{2T} = \hat{K}_{j_p j_p}\frac{\delta(\vec{r}_i - \vec{r}_j)}{2T}$$
$$\overline{\vec{\xi}_n^*(\vec{r}_i)\vec{\xi}_p(\vec{r}_j)} = \overline{\vec{\xi}_p^*\vec{\xi}_n} = 0$$

These expressions in turn give the greatly simplified expression for power spectral density, as follows.

$$S_V = \iiint_r \left(\frac{1}{q^2}\nabla G_n^* \cdot \hat{K}_{j_n j_n} \cdot \nabla G_n + \frac{1}{q^2}\nabla G_p^* \cdot \hat{K}_{j_p j_p} \cdot \nabla G_p\right) d^3 r \tag{2–102}$$

2.5.2 Comparison of Velocity Fluctuation Noise Simulation with Energy Balance and with Drift-Diffusion Models

2.5.2.1 One Dimensional $n^+/n/n^+$ Resistor Simulations

Velocity fluctuation noise simulations were performed on $n^+/n/n^+$ resistors, using the energy balance and drift-diffusion models simulated by FLOODS. The thickness of the n^+ regions considered were $0.5\mu m$. The doping density was 10^{18} cm^{-3} in the n^+ regions and 10^{17} cm^{-3} in the lower doped regions. The low-field carrier mobilities used were given by the Klaassen Model [8, 9], and the velocity saturation relations used follow the Canali model for Drift-Diffusion and its Energy Balance equivalent [38], with electron and hole saturation velocities of $1.07 \cdot 10^7$ cm/s and $8.37 \cdot 10^6$ cm/s, respectively. The ratio of heat flow mobility to carrier mobility was chosen to be 0.8 and the inhomogeneity parameters λ_{P_n} and λ_{Q_n} were chosen to be zero. The diffusivity used to compute local noise strength for the energy balance model uses Einstein's relation with the low kinetic energy mobility and the average of the carrier and lattice temperatures as discussed previously.

Fig. 2-1 shows the doping concentration and the electron temperature computed using the energy balance model for a $0.1\mu m$ resistor with a bias of $25mV$. The effects of

Peltier cooling and Joule heating as the electrons move from left to right can clearly be seen. Fig. 2-2 shows the contributions to velocity fluctuation noise (the quantity inside the integral of Eqs. (2–101) and (2–92)). This result is in qualitative agreement with the results published for the full hydrodynamic and drift-diffusion models by Jungemann, et. al. [46]. The effect of the energy balance model on the local noise contribution is to enhance it where the temperature increases in the direction of average carrier velocity (the force due to the temperature gradient assists the flow of carriers) and to diminish the noise contribution when the temperature decreases in the direction of the average carrier velocity (the force due to the temperature gradient opposes the flow of carriers). Fig. 2-4 shows the total velocity fluctuation noise for several lengths of the lowly doped region, for simulations using both the energy balance and drift-diffusion models and at two bias points. The points for the $0.1\mu m$ resistor at $25mV$ or $0.5V$ bias are the integral of the curves in Figs. 2-2 and 2-3. This figure shows that the energy balance model predicts lower overall velocity fluctuation noise than drift-diffusion, and this effect is enhanced at higher bias. This is further illustrated by Fig. 2-5, which shows the ratio of the noise predicted by the energy balance model to that predicted by the drift-diffusion model for the same resistors and at the same bias points.

2.5.2.2 nMOSFET Simulations

Velocity fluctuation noise simulations were also performed on a $0.25\mu m$ n-channel MOSFET, using the energy balance and drift-diffusion models simulated by FLOODS. The considered device has a $30\mathring{A}$ gate oxide, and is typical of recent transistor designs, with $100nm$ shallow source and drain extensions to reduce 2D short channel effects. The transport parameters used in the drift-diffusion and energy balance models were the same as those used in the resistor simulations. The Darwish mobility model was included to degrade the mobility in the channel due to surface scattering.

Fig. 2-6 depicts the doping profile of the device, on a log scale. This provides a picture of the geometry of the device with shallow n^+ source/drain extensions. Fig. 2-7

shows the contribution of the local velocity fluctuations to the drain current noise for the drift-diffusion model in the linear region of operation. Fig. 2-8 shows the contribution of the local velocity fluctuations to the drain current noise for the energy balance model, for the same bias. Both cases clearly show that velocity fluctuations only couple out from the channel. Also, the total simulated noise in both cases is in good agreement with the theoretical result of $4kTg_{d0}$ where g_{d0} was computed at a very low drain bias by the simulator. These results were also in qualitative agreement with those exhibited in the resistor results, in that the energy balance model predicts slightly lower velocity fluctuation noise.

2.6 Impedance Field Simulation of Number Fluctuation Noise

In this section the fluctuation terms for number fluctuations are traced through their origins in the BTE (2–2) to each contribution to the system of equations for each transport model.

2.6.1 Number Fluctuation Noise Simulation

Number fluctuations are caused by either interband transitions of particles or tunneling from one location to another. These transitions (except for the case of carrier tunneling) involve collisions with phonons, photons, or other carriers. As with any other transition, both energy and momentum must be conserved. Microscopically, the interband carrier transition term of the BTE can be described by a statistical mean component and a stochastic component, which fluctuates randomly and with a zero statistical mean.

$$s(\vec{r},\vec{p},t) = \overline{s(\vec{r},\vec{p},t)} + \gamma_f \tag{2–103}$$

where γ_f is a Langevin noise source which represents a fluctuation in $s(\vec{r},\vec{p},t)$. Langevin noise sources must be inserted into the PDE's of the transport model through those terms derived from the interband transition term of the BTE. This should be considered for each moment individually.

For the zeroeth-order moment, the interband transition term is characterized as follows.

$$\frac{1}{\Omega}\sum_{p} s(\vec{r},\vec{p},t) = [\mathrm{G}_n - \mathrm{R}_n] + \frac{1}{\Omega}\sum_{p}\gamma_f = \mathrm{G}_n - \mathrm{R}_n + \gamma_n \tag{2–104}$$

In the case of bulk or surface traps, there will also be a first-order moment and corresponding term for trapped electrons. For the first-order moment, this term is characterized as follows.

$$\frac{1}{\Omega}\sum_{p} \vec{p}s(\vec{r},\vec{p},t) = 0 + \frac{1}{\Omega}\sum_{p}\vec{p}\gamma_f = \vec{\gamma}_{v_n} \tag{2–105}$$

Since the direction of the momentum of generated or recombining carriers is random (resulting in the zero statistical mean component), it follows that the effect of number fluctuations on the average momentum of the carrier distribution is small, and $\vec{\gamma}_{v_n}$ is usually assumed to be negligible. This assumption is valid, since intraband transitions have a much greater effect on the momentum distribution. However, this is an assumption and it may not be appropriate in some situations where the carrier concentration is very low (such that velocity fluctuations do not dominate this term). For the second-order moment, this term is characterized as follows.

$$\frac{1}{\Omega}\sum_{p} \frac{|\vec{p}|^2}{2m_n^*}s(\vec{r},\vec{p},t) = [\mathrm{G}_{W_n} - \mathrm{R}_{W_n}] + \frac{1}{\Omega}\sum_{p}\frac{|\vec{p}|^2}{2m_n^*}\gamma_f = \mathrm{G}_{W_n} - \mathrm{R}_{W_n} + \gamma_{w_n} \tag{2–106}$$

For the case of transitions that can be considered to only involve carriers with low kinetic energy (i.e. tunneling or band-trap transitions) this term can be assumed to be zero. However, for the case of impact ionization or Auger recombination this term should be considered, and can only be ignored if the effects of this term are studied and shown to be negligible. For the third-order moment, the Langevin term $\vec{\gamma}_{s_n}$ is related to $\vec{\gamma}_{v_n}$ (Equation 2–60) and is therefore assumed to be zero.

Therefore, the number fluctuation Langevin sources γ_n, γ_p, γ_{n_T} (trapped carriers, if necessary), γ_{w_n}, and γ_{w_p} enter the complete system of equations derived from the first four moments of the BTE as follows. As previously, the asterisks to denote effective masses and

mobilities are omitted for clarity.

$$\nabla^2\psi = -\frac{q}{\epsilon}(p - n + N_D^+ - N_A^-) - \frac{\rho_t}{\epsilon}$$

$$\frac{dn}{dt} = -\nabla\cdot(n\vec{V}_n) + \mathrm{G}_n - \mathrm{R}_n + \gamma_n \tag{2–107}$$

$$\frac{dp}{dt} = -\nabla\cdot(p\vec{V}_p) + \mathrm{G}_p - \mathrm{R}_p + \gamma_p \tag{2–108}$$

$$\frac{dn_T}{dt} = \mathrm{G}_p + \mathrm{R}_n - \mathrm{G}_n - \mathrm{R}_p + \gamma_{n_T} \tag{2–109}$$

$$m_n\frac{d(n\vec{V}_n)}{dt} = -\nabla(nkT_n) - qn\vec{E} - n\left(\frac{q\vec{V}_n}{\mu_n} - \lambda_{P_n}\nabla(kT_n)\right)$$

$$m_p\frac{d(p\vec{V}_p)}{dt} = -\nabla(pkT_p) + qp\vec{E} - p\left(\frac{q\vec{V}_p}{\mu_p} - \lambda_{P_p}\nabla(kT_p)\right)$$

$$\frac{3}{2}k\frac{d(nT_n)}{dt} = -\nabla\cdot(n\vec{S}_n) - q\vec{E}\cdot(n\vec{V}_n) + \mathrm{G}_{W_n} - \mathrm{R}_{W_n} - \frac{3}{2}nk\frac{T_n - T_L}{\langle\tau_{W_n}\rangle} + \gamma_{w_n} \tag{2–110}$$

$$\frac{3}{2}k\frac{d(pT_p)}{dt} = -\nabla\cdot(p\vec{S}_p) + q\vec{E}\cdot(p\vec{V}_p) + \mathrm{G}_{W_p} - \mathrm{R}_{W_p} - \frac{3}{2}pk\frac{T_p - T_L}{\langle\tau_{W_p}\rangle} + \gamma_{w_p} \tag{2–111}$$

$$m_n\frac{d(n\vec{S}_n)}{dt} = -\nabla\left(\frac{5}{2}nk^2T_n^2\right) - q\vec{E}\left(\frac{5}{2}nkT_n\right) - n\left(\frac{q\vec{S}_n}{\mu_{S_n}} - \lambda_{Q_n}\nabla\left(\frac{5}{2}k^2T_n^2\right)\right)$$

$$m_p\frac{d(p\vec{S}_p)}{dt} = -\nabla\left(\frac{5}{2}pk^2T_p^2\right) + q\vec{E}\left(\frac{5}{2}pkT_p\right) - p\left(\frac{q\vec{S}_p}{\mu_{S_p}} - \lambda_{Q_p}\nabla\left(\frac{5}{2}k^2T_p^2\right)\right)$$

The fluctuation of voltage $\tilde{V}_c$ at the considered external contact is then given as follows.

$$\tilde{V}_c = \iiint_r \left(G_n\gamma_n + G_p\gamma_p + G_{n_T}\gamma_{n_T} + G_{E_n}\gamma_{w_n} + G_{E_p}\gamma_{w_p}\right) d^3r \tag{2–112}$$

where G_n, G_p, G_{n_T}, G_{E_n}, and G_{E_p} are the Green's functions associated with the scalar-valued electron, hole, and trapped electron carrier continuity equations and electron and hole energy balance equations, respectively. The power spectral density $S_V = 2T\overline{\tilde{V}_c^*\tilde{V}_c}$ is computed as follows.

$$S_V = 2T\overline{\iiint_{r_i}\begin{pmatrix} G_n^*\gamma_n^* + G_p^*\gamma_p^* + G_{n_T}^*\gamma_{n_T}^* + \\ G_{E_n}^*\gamma_{w_n}^* + G_{E_p}^*\gamma_{w_p}^* \end{pmatrix} d^3r_i \iiint_{r_j}\begin{pmatrix} G_n\gamma_n + G_p\gamma_p + G_{n_T}\gamma_{n_T} + \\ G_{E_n}\gamma_{w_n} + G_{E_p}\gamma_{w_p} \end{pmatrix} d^3r_j} \tag{2–113}$$

As in the section on velocity fluctuations, there are, depending on the number fluctuation mechanism considered, approximations that the noise sources are statistically independent in position, as follows.

$$\overline{\gamma_\alpha^*(\vec{r}_i)\gamma_\alpha(\vec{r}_j)} = K_{\alpha\alpha}\frac{\delta(\vec{r}_i - \vec{r}_j)}{2T} \tag{2–114}$$

This is valid since random fluctuations in generation rates are not expected to be strongly correlated through position, except for the case of carrier tunneling. The noise strengths can be evaluated using Monte Carlo computations, but this is not feasible for low frequency computations. The alternative is to evaluate the local noise strengths using the closed form expressions such as those derived by van Vliet [47]. Terms involving γ_{w_n} must be evaluated differently for each type of mechanism.

None of the number fluctuation terms are involved in back-substituted expressions for heat flow or particle current, as in the case of velocity fluctuations, so extending this to the hydrodynamic, energy balance, and drift-diffusion cases is trivial. The effects of independent mechanisms are added using the superposition principal, as follows.

$$S_V|_{total} = S_V|_{trapping} + S_V|_{tunneling} + S_V|_{impact} \tag{2–115}$$

2.6.1.1 Bulk or surface trap capture and emission

For the case of a trap species located at a particular energy level E_T relative to the intrinsic energy level E_I, the statistical mean capture and emission rates of electrons and holes are governed by Shockley-Read-Hall recombination and generation rates R_{nT}, R_{pT}, G_{nT}, and G_{pT}, as follows.

$$\mathrm{R}_{nT} = c_n n(N_T - n_T) \tag{2–116}$$

$$\mathrm{G}_{nT} = e_n n_T = c_n n_1 n_T \tag{2–117}$$

$$\mathrm{R}_{pT} = c_p p n_T \tag{2–118}$$

$$\mathrm{G}_{pT} = e_p(N_T - n_T) = c_p p_1(N_T - n_T) \tag{2–119}$$

where c_n, e_n, c_p, and e_p are the electron and hole capture and emission coefficients, and n_1 and p_1 are the equivalence carrier concentrations, i.e. the electron and hole concentrations for the case when the Fermi level is the same as the trap level. They are computed using the Maxwell-Boltzmann approximation as follows.

$$n_1 = n_i exp\left(\frac{E_T - E_I}{kT_L}\right) \tag{2–120}$$

$$p_1 = n_i exp\left(\frac{E_I - E_T}{kT_L}\right) \tag{2–121}$$

where E_T is the trap energy level, E_I is the intrinsic energy level, and n_i is the intrinsic electron concentration. The corresponding local noise strengths are computed as follows [29, 47].

$$\overline{\gamma_n^*(\vec{r}_i)\gamma_n(\vec{r}_j)} = -\overline{\gamma_n^*(\vec{r}_i)\gamma_t(\vec{r}_j)} = 2(\mathrm{G}_{nT} + \mathrm{R}_{nT})\frac{\delta(\vec{r}_i - \vec{r}_j))}{2T} = K_{nn}\frac{\delta(\vec{r}_i - \vec{r}_j))}{2T} \tag{2–122}$$

$$\overline{\gamma_p^*(\vec{r}_i)\gamma_p(\vec{r}_j)} = -\overline{\gamma_p^*(\vec{r}_i)\gamma_t(\vec{r}_j)} = 2(\mathrm{G}_{pT} + \mathrm{R}_{pT})\frac{\delta(\vec{r}_i - \vec{r}_j))}{2T} = K_{pp}\frac{\delta(\vec{r}_i - \vec{r}_j))}{2T} \tag{2–123}$$

$$\overline{\gamma_t^*(\vec{r}_i)\gamma_t(\vec{r}_j)} = 2(\mathrm{G}_{nT} + \mathrm{R}_{nT} + \mathrm{G}_{pT} + \mathrm{R}_{pT})\frac{\delta(\vec{r}_i - \vec{r}_j))}{2T} = K_{tt}\frac{\delta(\vec{r}_i - \vec{r}_j))}{2T} \tag{2–124}$$

Note that the generation and recombination rates used in these expressions are only the components due to this trap species and its associated interactions. The terms involving γ_{w_n} and γ_{w_p} are assumed to be zero since the probability of capture or emission is highest from low kinetic energy states. The simplified power spectral density is then given as follows.

$$S_V = \iiint_r \begin{pmatrix} G_n^* K_{nn} G_n - G_n^* K_{nn} G_{n_T} + \\ G_p^* K_{pp} G_p - G_p^* K_{pp} G_{n_T} + \\ G_{n_T}^* K_{tt} G_{n_T} - G_{n_T}^* K_{nn} G_n - G_{n_T}^* K_{pp} G_p \end{pmatrix} d^3 r \tag{2–125}$$

2.6.1.2 Direct Carrier tunneling

Previously [29], noise due to carrier tunneling implemented in FLOODS was modelled as capture at fast surface states coupled with trap-to-trap tunneling from interface traps to the oxide traps. This was appropriate for the device and bias conditions in

previous works, since the Fermi level at the surface was in the energy gap. However, DC simulations of the devices measured for this work, and for any such highly scaled MOSFETs, show that the electron distribution is degenerate at the surface. Therefore, direct tunneling between the states in the conduction band at the silicon/oxide surface and traps in the oxide has been implemented in FLOODS as a part of this work.

Direct band-to-trap carrier tunneling is unique among the mechanisms considered in this work, in that it is a nonlocal mechanism involving fluctuations in two locations. The case of interest for the devices involved in this work is that of tunneling from the conduction band at the silicon surface and a trap in the oxide. As in the work of Hou [29], trapped carriers tunnel primarily to the nearest silicon node, and transitions between the gate and oxide traps are neglected. While the latter assumption is difficult to justify, it greatly simplifies the implementation and is therefore used. The interactions are between the trapped carrier continuity equation $\frac{dn_T^i}{dt} = \mathrm{R}_{nt}^{ij} - \mathrm{G}_{nt}^{ij} + \gamma_{n_T}^i = \gamma_{n_T}^i$ at some oxide node at position r_i and the electron continuity equation at some interface silicon node at position r_j. The tunneling capture and emission rates R_{nt}^{ij} and G_{nt}^{ij} are given as follows.

$$\mathrm{R}_{nt}^{ij} = c_{nt}^{ij} n^j (N_T^i - n_T^i) \tag{2–126}$$

$$\mathrm{G}_{nt}^{ij} = e_{nt}^{ij} n_T^i \tag{2–127}$$

where c_{nt}^{ij} and e_{nt}^{ij} are the capture and emission coefficients. Since there is no steady-state change in the concentration of trapped carriers, if there is no tunneling to the gate then these rates are equal. The capture and emission coefficients are given as follows.

$$e_{nt}^{ij} = c_{nt}^{ij} \frac{n^j (N_T^i - n_T^i)}{n_T^i} \tag{2–128}$$

$$c_{nt}^{ij} = T_0 exp(-\alpha d) \tag{2–129}$$

where T_0 is the tunneling coefficient, α is the attenuation constant of the electron wave functions, and d is the distance between node i and node j. The attenuation constant, for

a triangular barrier, is given as follows [29].

$$\alpha = -\frac{4}{3}\frac{\sqrt{2m_{ox}}}{\hbar}\frac{\phi_{itf}^{1.5} - \phi_{ox}^{1.5}}{\phi_{itf} - \phi_{ox}} \tag{2–130}$$

where m_{ox} is the effective mass of the tunneling electrons in the oxide, and ϕ_{itf} is the barrier height at the interface, equal to the difference in the electron affinities of the bulk silicon and the gate oxide, $4.05eV$. The barrier height at the trap is $\phi_{ox} = 4.05eV + q(\psi^j - \psi^i)$. In the limit that the field in the oxide is zero, α is $1.3 \cdot 10^8 cm^-1$. The tunneling coefficient for such band-to-trap transitions T_0 is not known. This value is arbitrary however, as the simulations have shown that the oxide noise is not sensitive to this parameter (there is effectively a functional dependence in $G_{nt}^* G_{nt}$ of $1/T_0$, such that the total noise power spectral density is insensitive to T_0).

The contribution to fluctuation in a contact voltage due to such transitions is given as follows.

$$\tilde{V}_c^{ij} = G_{n_T}(\vec{r}_i)\gamma_{n_T}(\vec{r}_i)V_i + G_n(\vec{r}_j)\gamma_n(\vec{r}_j)V_j \tag{2–131}$$

where V_i and V_j are the nodal volumes at the oxide and interface nodes, respectively. The power spectral density is then computed as follows.

$$S_V^{ij} = 2T\left(\begin{array}{c} G_{n_T}^*(\vec{r}_i)\overline{\gamma_{n_T}^*(\vec{r}_i)\gamma_{n_T}(\vec{r}_i)}G_{n_T}(\vec{r}_i)V_i^2 + G_{n_T}^*(\vec{r}_i)\overline{\gamma_{n_T}^*(\vec{r}_i)\gamma_n(\vec{r}_j)}G_n(\vec{r}_j)V_iV_j + \\ G_n^*(\vec{r}_j)\overline{\gamma_n^*(\vec{r}_j)\gamma_{n_T}(\vec{r}_i)}G_{n_T}(\vec{r}_i)V_jV_i + G_n^*(\vec{r}_j)\overline{\gamma_n^*(\vec{r}_j)\gamma_n(\vec{r}_j)}G_n(\vec{r}_j)V_j^2 \end{array}\right) \tag{2–132}$$

The fluctuations at the interface and at the trap are also related, as dictated by conservation of particles.

$$\gamma_n V_j = -\gamma_{n_T} V_i \tag{2–133}$$

This results in the following relations.

$$\overline{\gamma_n^*(\vec{r}_j)\gamma_n(\vec{r}_j)} = 2(\mathrm{G}_{nt} + \mathrm{R}_{nt})\frac{1}{2TV_j} = K_{tt}\frac{1}{2TV_j} \tag{2–134}$$

$$\overline{\gamma_{n_T}^*(\vec{r}_i)\gamma_{n_T}(\vec{r}_i)} = \frac{V_j^2}{V_i^2}\overline{\gamma_n^*(\vec{r}_j)\gamma_n(\vec{r}_j)} = K_{tt}\frac{V_j}{2TV_i^2} \tag{2–135}$$

$$\overline{\gamma_n^*(\vec{r}_j)\gamma_{n_T}(\vec{r}_i)} = -\frac{V_j}{V_i}\overline{\gamma_n^*(\vec{r}_j)\gamma_n(\vec{r}_j)} = -K_{tt}\frac{1}{2TV_i} \tag{2–136}$$

where γ_n represents fluctuations in electron concentration at the surface, and γ_{n_T} represents fluctuations in the concentration of trapped carriers at a location in the oxide. The terms involving γ_{w_n} are assumed to be zero since the carrier distribution is close to the conduction band edge unless the surface is strongly degenerate, in which case a carrier involved in the transition is one of many. Thus, the average kinetic energy of a degenerate carrier distribution does not fluctuate much due to this mechanism.

Finally, the simplified power spectral density then reduces to the following.

$$S_V^{ij} = V_j \begin{pmatrix} G_{n_T}^*(\vec{r}_i)K_{tt}G_{n_T}(\vec{r}_i) - G_{n_T}^*(\vec{r}_i)K_{tt}G_n(\vec{r}_j) - \\ G_n^*(\vec{r}_j)K_{tt}G_{n_T}(\vec{r}_i) + G_n^*(\vec{r}_j)K_{tt}G_n(\vec{r}_j) \end{pmatrix} \tag{2–137}$$

2.6.1.3 Impact Ionization

An impact ionization event results in the generation of an electron and a hole, accompanied by a loss in kinetic energy of a single carrier that is sufficient to cause the interband transition. The carrier density and kinetic energy rate fluctuations associated with electron ionization events are then related, as follows.

$$\gamma_p = \gamma_n \tag{2–138}$$

$$\gamma_{w_n} = -E_\delta \gamma_n \tag{2–139}$$

where E_δ represents the average energy lost by electrons in impact ionization events. This is expected to be nearly equal to the minimum kinetic energy required to excite an electron from the valence band to the conduction band while conserving energy and

momentum, which for the minimum Umklapp process is slightly higher than E_G. The approximation $E_\delta = E_G$ is assumed. The local noise strengths are then computed as follows.

$$\overline{\gamma_n^*(\vec{r}_i)\gamma_n(\vec{r}_j)} = \overline{\gamma_p^*(\vec{r}_i)\gamma_p(\vec{r}_j)} = -\overline{\gamma_n^*(\vec{r}_i)\gamma_p(\vec{r}_j)} = 2\mathrm{G}_{ii}\frac{\delta(\vec{r}_i - \vec{r}_j)}{2T} = K_{nn}\frac{\delta(\vec{r}_i - \vec{r}_j)}{2T} \tag{2–140}$$

$$\overline{\gamma_{w_n}^*(\vec{r}_i)\gamma_{w_n}(\vec{r}_j)} = 2\mathrm{G}_{ii}E_\delta^2\frac{\delta(\vec{r}_i - \vec{r}_j)}{2T} = E_\delta^2 K_{nn}\frac{\delta(\vec{r}_i - \vec{r}_j)}{2T} \tag{2–141}$$

$$\overline{\gamma_{w_n}^*(\vec{r}_i)\gamma_n(\vec{r}_j)} = \overline{\gamma_{w_n}^*(\vec{r}_i)\gamma_p(\vec{r}_j)} = -2\mathrm{G}_{ii}E_\delta\frac{\delta(\vec{r}_i - \vec{r}_j)}{2T} = -E_\delta K_{nn}\frac{\delta(\vec{r}_i - \vec{r}_j)}{2T} \tag{2–142}$$

where G_{ii} is the impact ionization rate, computed as in Section 2.4.

The power spectral density is then given as follows.

$$S_V = \iiint_r \begin{pmatrix} G_n^* K_{nn} G_n - G_n^* K_{nn} G_p - E_\delta G_n^* K_{nn} G_{E_n} \\ G_p^* K_{nn} G_p - G_p^* K_{nn} G_n - E_\delta G_p^* K_{nn} G_{E_n} \\ E_\delta^2 G_{E_n}^* K_{nn} G_{E_n} - E_\delta G_{E_n}^* K_{nn} G_n - E_\delta G_{E_n}^* K_{nn} G_p \end{pmatrix} d^3r \tag{2–143}$$

2.6.2 Comparison of Number Fluctuation Noise Simulation with Energy Balance and Drift-Diffusion Models in $n^+/n/n^+$ Resistors

Number fluctuation noise simulations were performed on the same resistor structures that were previously used in section 2.5.2.1, with the same choices for transport parameters. An electron trap ($c_n = 10^{-9} cm^3 s^{-1} > c_p = 10^{-11} cm^3 s^{-1}$) was used to simulate bulk generation-recombination noise with a constant trap density of $10^{15} cm^{-3}$ and a trap energy level near to the equilibrium Fermi level in the lowly doped region. Figure 2-9 shows the contributions to number fluctuation noise (the quantity inside the integral of Eq. (2–113). Clearly, the effect of the hydrodynamic model on number fluctuation noise is not as strong as that in the case of velocity fluctuations. Figure 2-10 shows the total noise integrated across the length of the devices. For long resistors, the bias dependence of the Noise is I^2, consistent with that of trapping in quasineutral regions. Figure 2-11 shows the ratio of the noise predicted by the Energy Balance model to that predicted by the Drift-Diffusion model.

2.7 Quantization Effects and Noise

The Schrödinger wave equation allows the evaluation of allowed states for electrons, given the potential energy that confines the electrons in a structure (for example, in the attractive electric field that surrounds positively charged atomic nucleii). The SWE is given as follows.

$$\left(\frac{\hbar^2}{2m}\nabla^2 + V(\vec{r},t)\right)\psi(\vec{r},t) = E\psi(\vec{r},t) \tag{2–144}$$

$V(\vec{r},t)$ is the potential energy seen by an electron, as a function of position and time. $\psi(\vec{r},t)$ and E are the wavefunction and associated energy of any allowed electron state that is a solution of this Eigenproblem. The solution of the SWE in an infinite well is well known, as illustrated in Figure 2-12. Note that the plotted functions are the waveforms times their complex conjugate, giving the shape of the probability functions for electrons in these odd and even states. The odd solutions have an odd number of nodes, and the even solutions have an even number.

In semiconductors such as Silicon, the periodicity of the positions of atomic nucleii gives rise to a periodic potential energy, yielding many allowed states that are clustered in energy within bands. The core electrons (in atoms that have them) are tightly bound in energy bands that have electrons in each and every allowed state. The valence electrons are less tightly bound in the valence band, with a few energetic electrons that are excited from the valence band or from bound states such as donor impurities or electron trap defects to the conduction band or to bound states at acceptor impurities and hole trap defects. As long as the crystal is periodic for long distances, and the electric fields associated with applied bias or nonhomogeneity are significantly lower than the binding forces in the periodic structure of the crystal lattice, the SWE solution can be assumed to give states consistent with the nearly free electron and hole models previously described.

However, in highly scaled and strongly inverted MOSFETs such as the devices considered in this study, the electric field under the gate oxide confines carriers tightly to the Silicon/Oxide surface. This confinement is in only one dimension (incident to the

surface), so the allowed states in the Silicon near the surface form quantized subbands for which carriers conduct current in the unconfined directions (along the surface).

This quantization effect gives rise to displacement of the inversion carriers from the surface as well as a local increase in the effective energy gap of the semiconductor. These effects are manifested in the MOSFET as an increase in the effective threshold voltage and a decrease in the number of carriers in the channel compared to what are predicted by classical models.

Several methods have been employed to approximate the effects of quantization in simulation frameworks originally developed for semi-classical transport. Some involve the computational of a deformation potential to reduce and displace inversion layers [48] . This requires adjustment of the mobility model [49]. However, the goal of this study is to accurately simulate the noise in these MOSFETs. The velocity fluctuation noise for current flow toward the drain is not expected to depend greatly on the shape of the distribution of conductive carriers in directions perpindicular to this current flow, and is not observed within the measurement time window. The only velocity fluctuation noise observed within the measurement time window in this work is in the SOI devices, where it is caused by majority carriers in the floating body. The number fluctuation noise, in the measurement time window, is primarily manifested by tunneling of inversion layer carriers into and out of traps in the oxide. This number fluctuation noise is primarily affected by the number of carriers in the inversion layer, and the tunneling capture and emission rates of trapped carriers, and is again not greatly affected by the shape of the inversion layer carrier distribution. It is important to note that the tunneling probabilites of carriers in the interacting traps and inversion layer are a function of the tunneling distance. They are not as strongly dependent on position as an exponential function of the tunneling distance (such as those computed for models where the carriers are assumed to tunnel from the oxide edge and for which the barrier height is integrated throughout the tunneling distance), because the error displacement in tunneling position is in the region

where the electron energy is greater than the potential energy. Later analysis shows this effect in detail, but for now the quantization effects are lumped into the effective tunneling distance and barrier height, similar to the way that quantization-affected scattering is lumped into the mobility models. Therefore, quantization effects in highly scaled MOSFETs whose bias is limited to strong inversion can be approximated, for the purpose of noise simulation, by a large fixed surface charge. This raises the threshold voltage in strong inversion and reduce the mobile inversion charge, without adversely affecting the simulation of noise in the device. This point is illustrated for the simulated devices and is presented in Chapter 4.

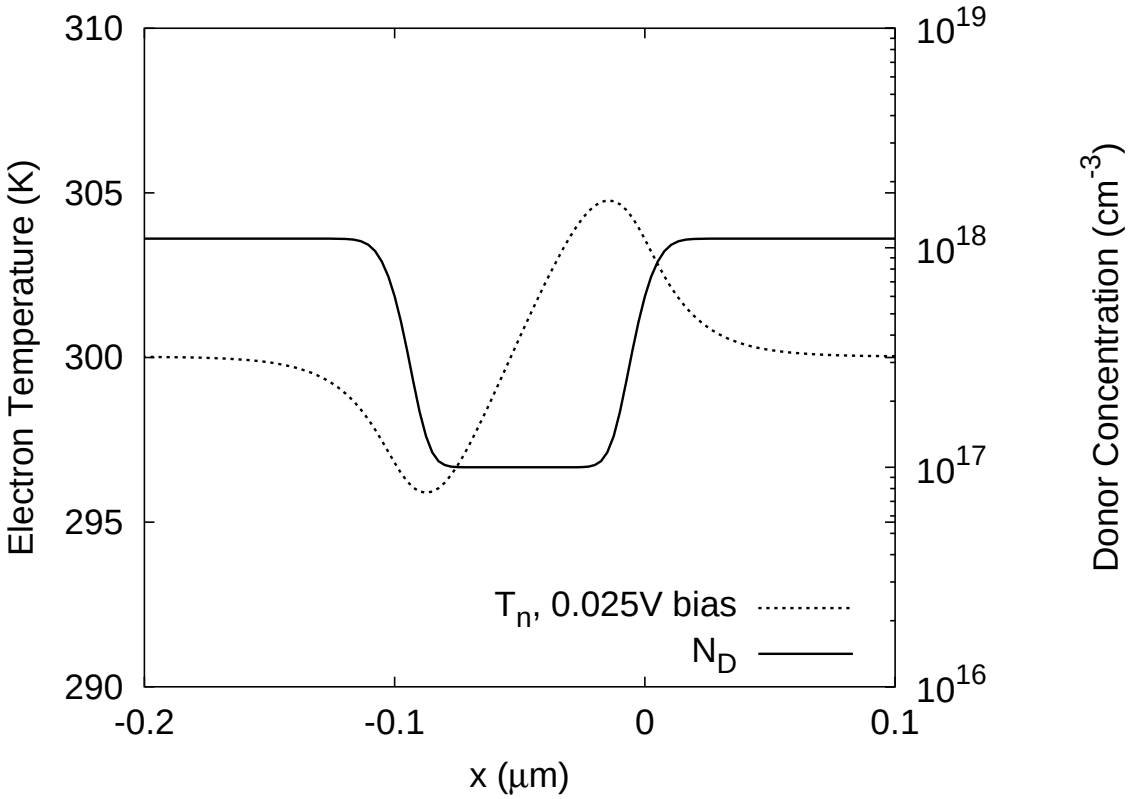

Figure 2-1. Electron temperature as a function of position for the energy balance model in a $0.1\,\mu$m $n^+/n/n^+$ resistor with a bias of $25mV$.

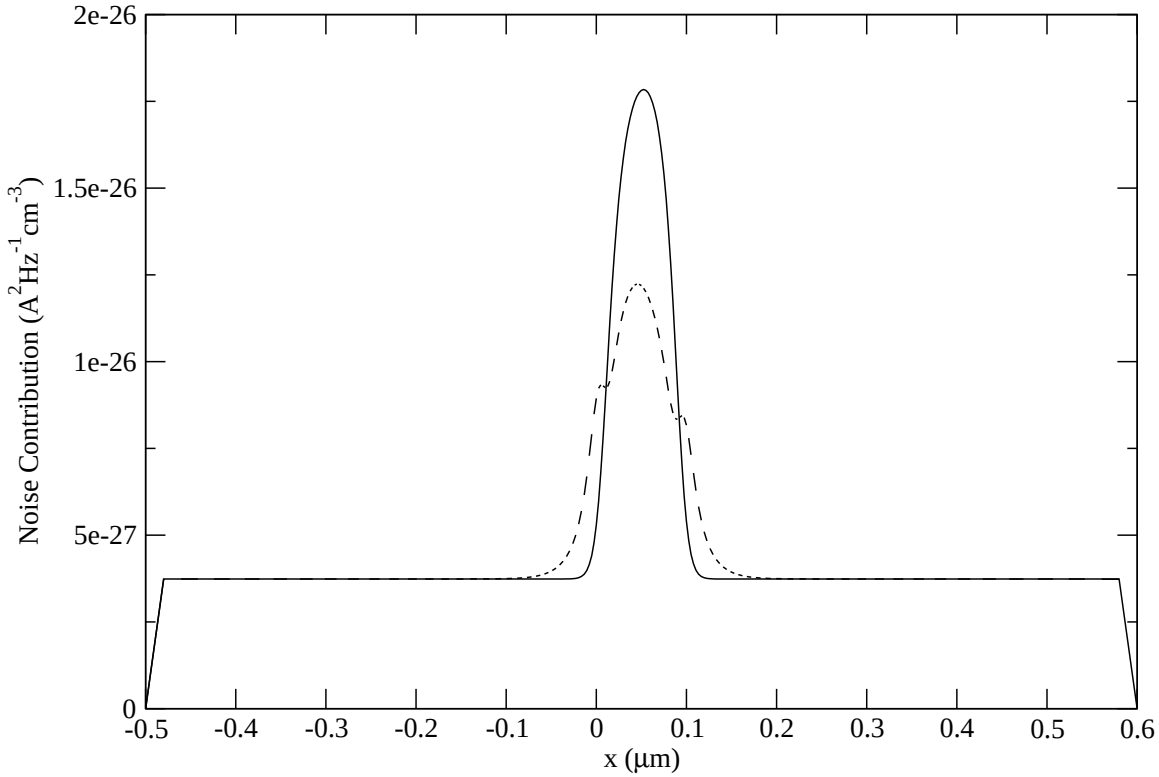

Figure 2-2. Velocity fluctuation noise contribution as a function of position in a $0.1\,\mu$m $n^+/n/n^+$ resistor for a bias of $25mV$.

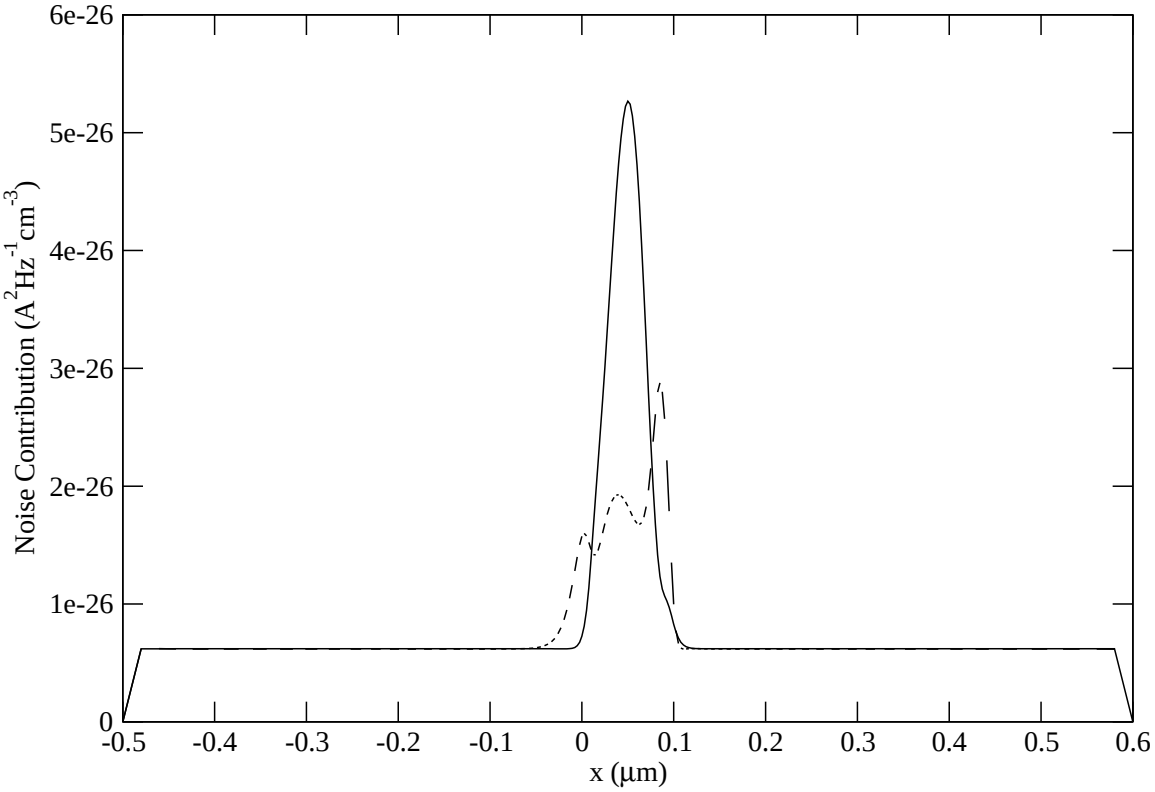

Figure 2-3. Velocity fluctuation noise contribution as a function of position in a $0.1\,\mu$m $n^+/n/n^+$ resistor for a bias of $0.5V$.

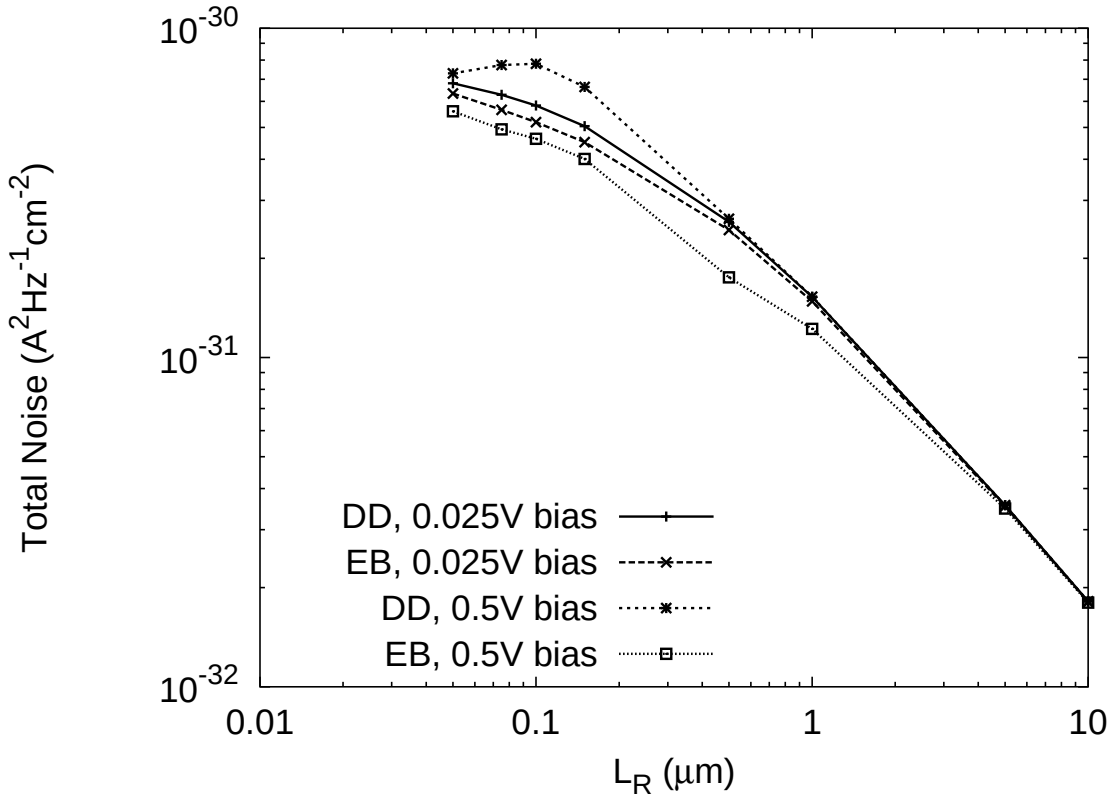

Figure 2-4. Velocity fluctuation noise for $n^+/n/n^+$ resistors of varying lengths.

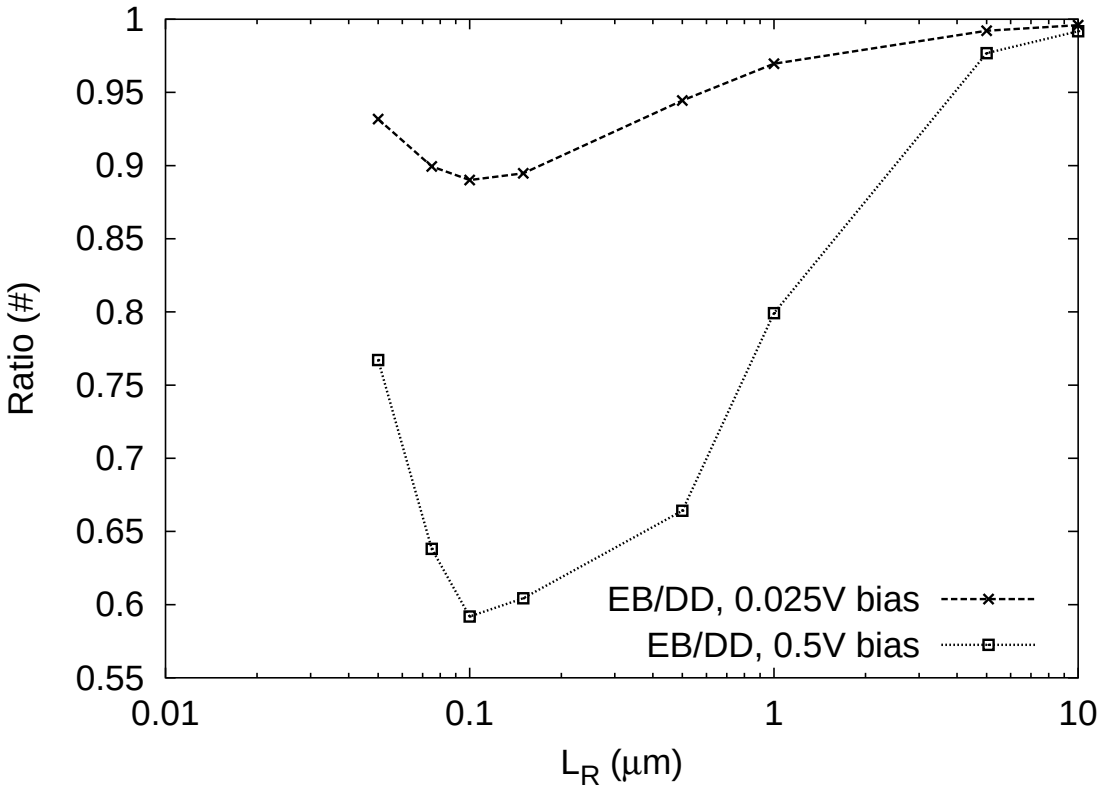

Figure 2-5. Ratio of velocity fluctuation noise predicted by Energy Balance model to that predicted by Drift-Diffusion for $n^+/n/n^+$ resistors of varying lengths.

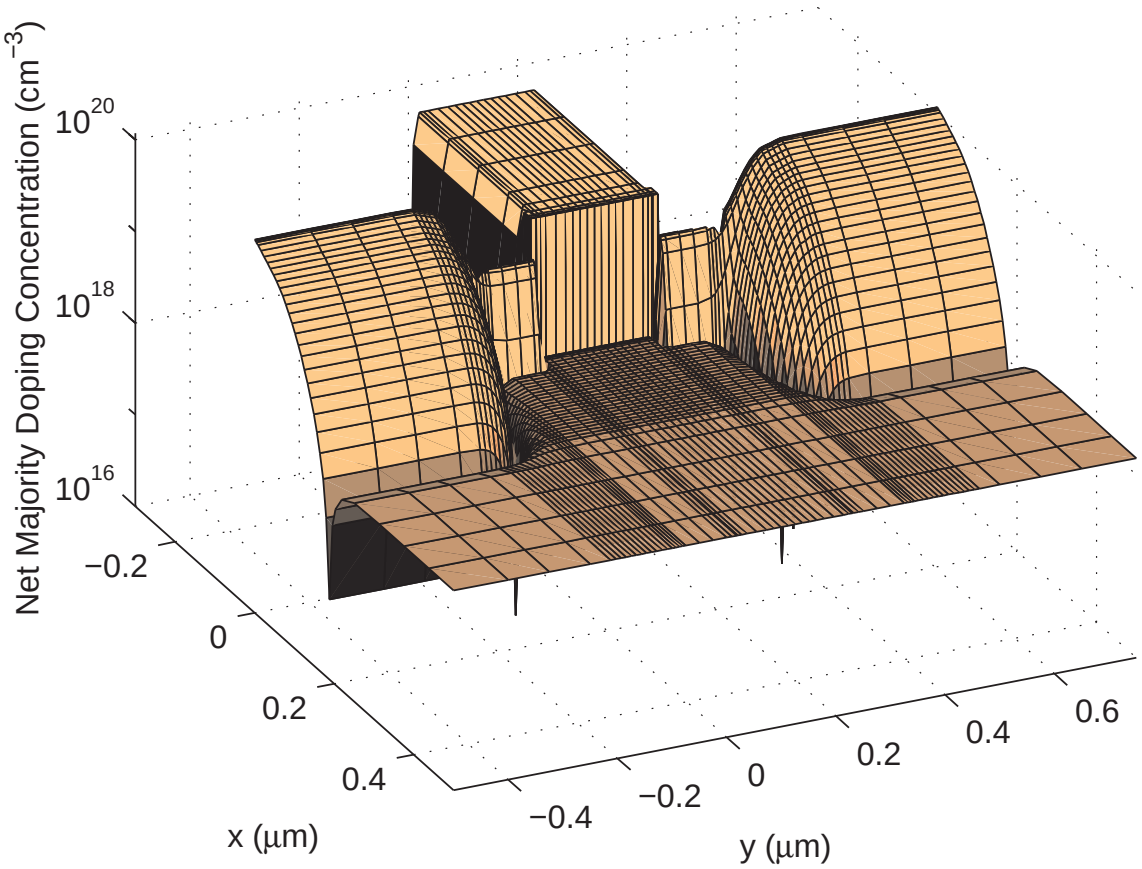

Figure 2-6. The net majority-type doping concentration plotted for a 0.25 μm nMOSFET. The gate is located to the rear, with the source on the left and the drain on the right.

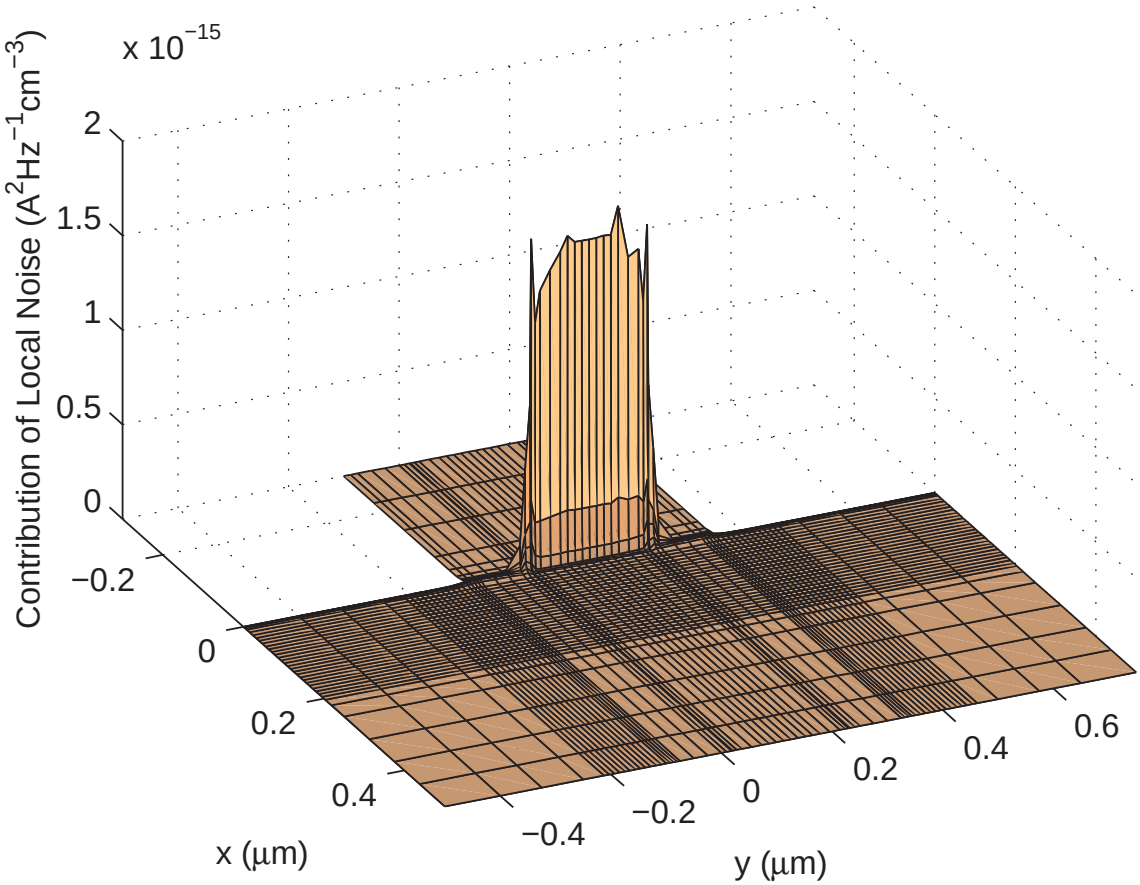

Figure 2-7. Contribution of local velocity fluctuation drain current noise as a function of position in the 0.25 μm nMOSFET as simulated using the drift-diffusion model, with $V_{GS} = 1.5$V and $V_{DS} = 10$mV. The total simulated noise was $1.89109 \cdot 10^{-23}\mathrm{A}^2\mathrm{Hz}^{-1}\mathrm{cm}^{-1}$, compared to the theoretical value $4kTg_{d0} = 1.7675 \cdot 10^{-23}\mathrm{A}^2\mathrm{Hz}^{-1}\mathrm{cm}^{-1}$.

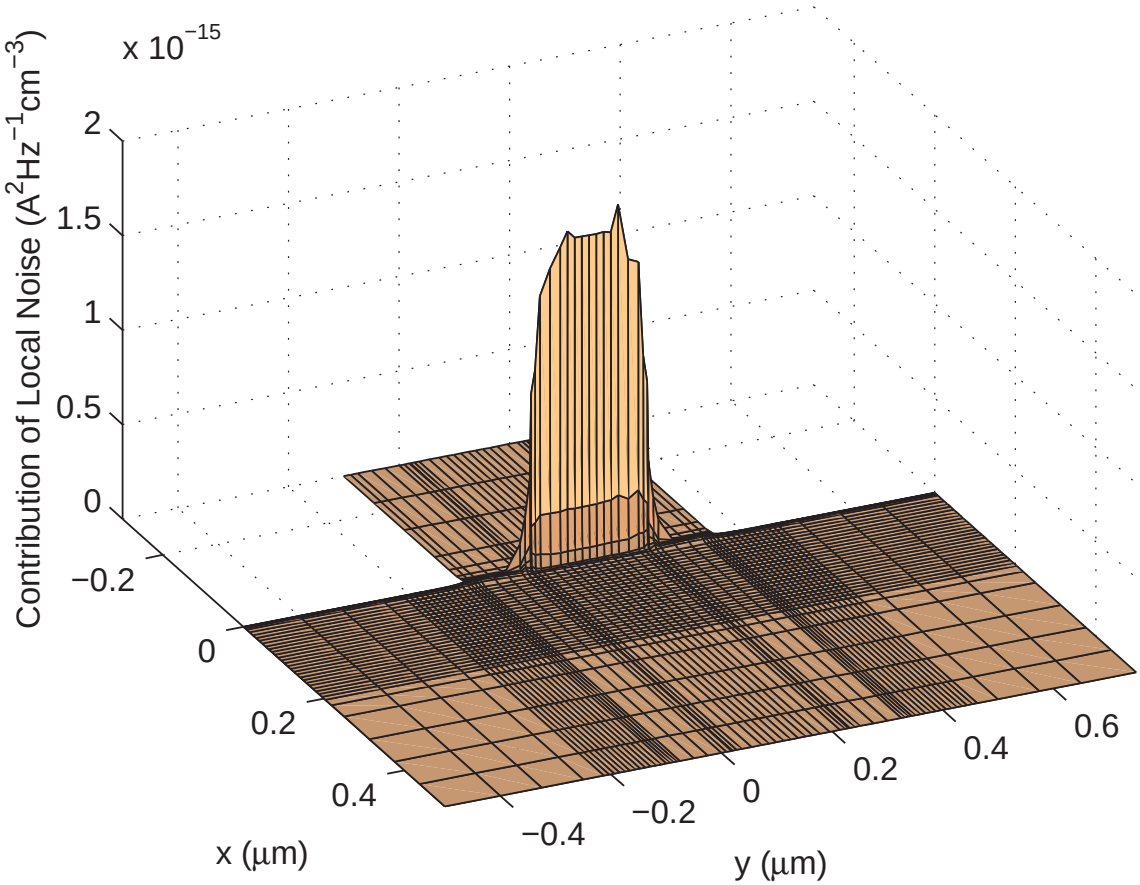

Figure 2-8. Contribution of local velocity fluctuation drain current noise as a function of position in the $0.25\,\mu$m nMOSFET as simulated using the energy balance model, with $V_{GS} = 1.5$V and $V_{DS} = 10$mV. The total simulated noise was $1.75531 \cdot 10^{-23}\mathrm{A}^2\mathrm{Hz}^{-1}\mathrm{cm}^{-1}$, compared to the theoretical value $4kTg_{d0} = 1.7805 \cdot 10^{-23}\mathrm{A}^2\mathrm{Hz}^{-1}\mathrm{cm}^{-1}$.

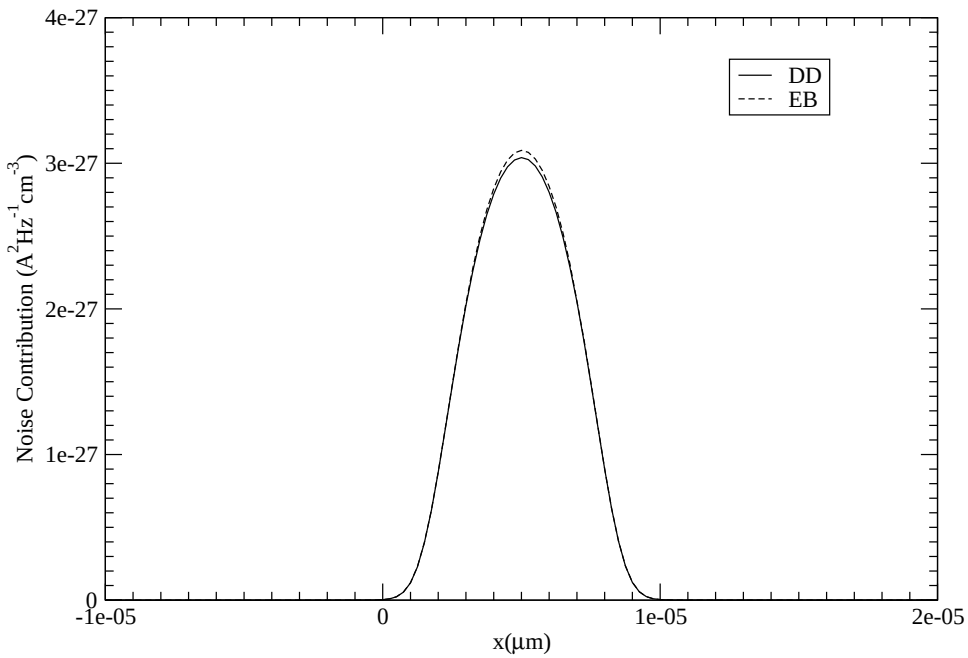

Figure 2-9. Number fluctuation noise contribution as a function of position in a $0.1\mu m$ $n^+/n/n^+$ resistor with a bias of $25mV$.

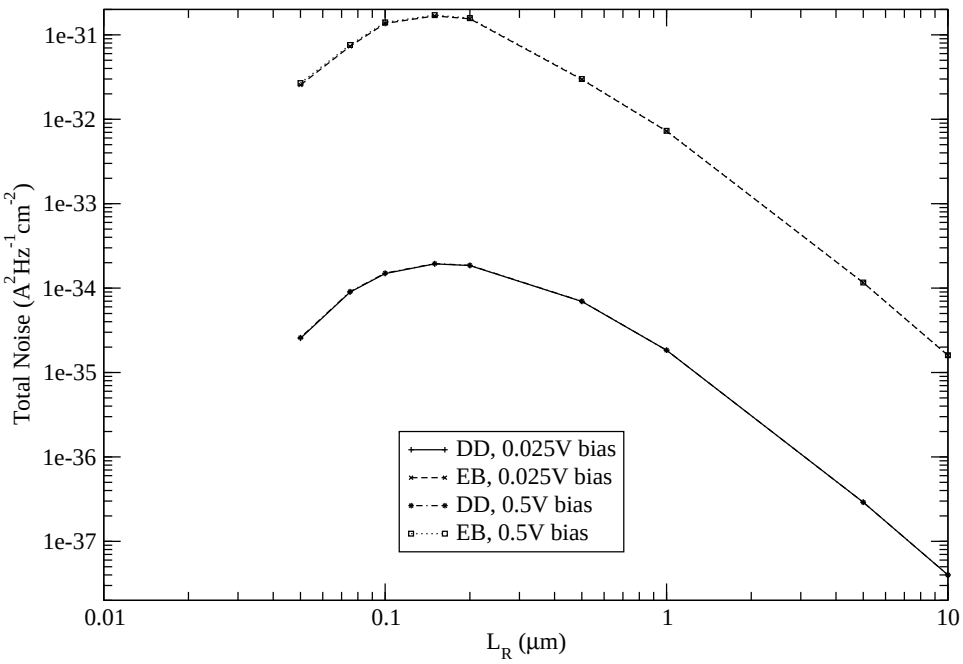

Figure 2-10. Number fluctuation noise for $n^+/n/n^+$ resistors of varying lengths.

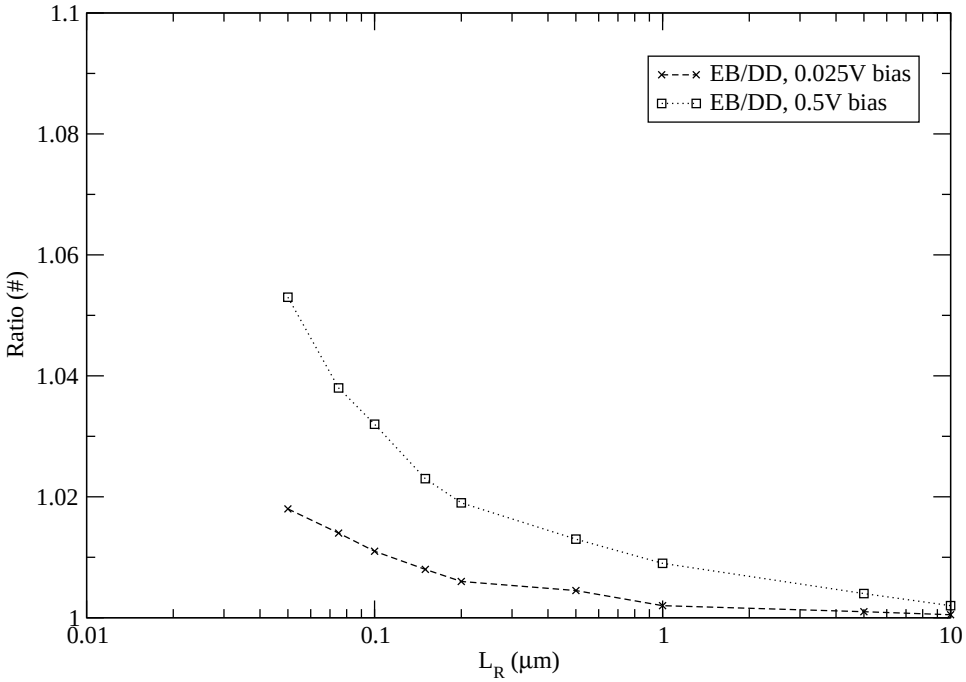

Figure 2-11. Ratio of number fluctuation noise predicted by the Energy Balance model to that predicted by Drift-Diffusion for $n^+/n/n^+$ resistors of varying lengths.

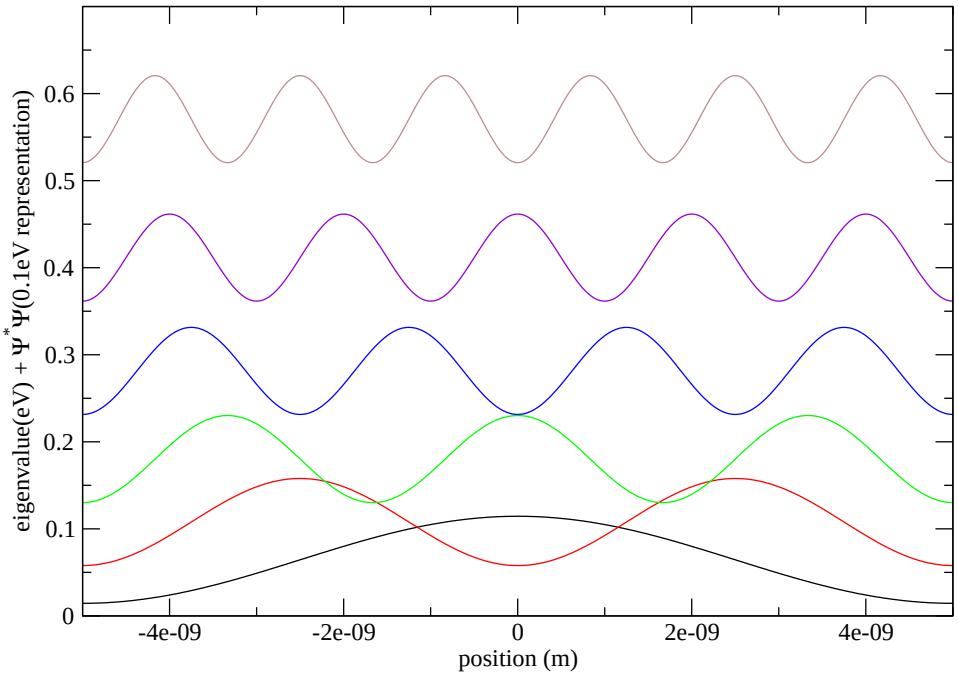

Figure 2-12. Solution of Schrödinger's Equation (probability distributions and associated energies) for allowed states in an infinite potential well.

CHAPTER 3
NOISE MEASUREMENTS

The measurement of noise in a semiconductor device must be conducted with care, because all devices in the measurement system generate noise which must be separated out from or made negligible compared to the noise generated within the device under test. As a result, noise measurement setups generally focus on low-noise components, clean DC power supplies, and quality electrical contacts. Traditionally used methods for protecting a device from high-voltage transients such as the use of reed relay switches and programmable voltage ramps from switching power supplies cannot be used due to the noisy signals the required components generate.

3.1 Measurement Setup

The noise measurements in this study were taken using the circuit depicted in Figure 3-1. The metal film resistors were soldered in place and BNC cables were used to connect the circuit to the amplifier and the power supply (which consists of two DC batteries, one 12.5V and one 2V). The amplifier used is the Brookdeal 5004, the spectrum analyzer is a Hewlett-Packard 3561A and two Agilent 34401A digital multimeters were used to measure gate and drain DC voltages.

3.1.1 Resistor Network Design

The gate bias is applied using a simple resistor divider circuit. The applied gate voltage is then given by the following equation.

$$V_G = \frac{R_1}{R_1 + R_2} V_{DD} \tag{3–1}$$

The resistor values (R_1 and R_2) should be chosen to be as small as possible to limit their contributions to the thermal noise at the drain, amplified from the gate, but taking into consideration their power dissipation limits and the current supplying ability of the batteries. The resistor values of $1.5k\Omega$ and $16k\Omega$ were chosen for R_1 and R_2, respectively.

The drain bias is applied using the three-resistor network consisting of resistors R_3, R_4, and R_5. The drain bias is determined by solving the following equation, using the

drain current of the device at the desired drain bias.

$$V_D = \frac{R_5}{R_3 + R_5} V_{DD} - I_D \frac{R_3 R_4 + R_4 R_5 + R_5 R_3}{R_3 + R_5} \tag{3–2}$$

R_4's resistance is desired to be as large as possible to maximize the significance of the high frequency intrinsic device thermal noise compared to the resistor voltage noise (such that $4kT(r_d||R_L) \approx 4kTr_d$). However, except for very small drain biases or very quiet (noiseless) devices, the corner frequency where low frequency noise becomes insignificant next to high frequency thermal noise is higher than the maximum frequency of the spectrum analyzer ($100kHz$). In addition, it is desirable to only vary one of the three resistors (R_3 was chosen for this) to apply differing drain bias. The maximum voltage drop across R_4 is then limited and must be significantly less than $V_{DD} - V_D$ to guarantee that fluctuations will not be clipped due to supply circuit limitations. Since the maximum current observed in the measured devices was approximately $3.5mA$, R_4 was chosen to be $2k\Omega$, resulting in a maximum voltage drop of around one-half the supply voltage. It is desirable to choose a value of R_5 which is less than R_4 such that the effect of varying R_3 will set the voltage of the internal network node, independent of the IV characteristics of the device under test. A value of $1k\Omega$ was chosen. R_3 is chosen for each device and bias point to match the desired drain voltage and measured IV characteristics.

3.1.2 Practical Considerations

The physical location of each circuit component and the BNC cables is depicted in Figure 3-2. Since switching power supplies are not used, the problem is presented of applying the bias to the device under test without applying any high-voltage transients which cause highly scaled and electrically sensitive MOS devices to degrade or suffer gate dielectric breakdown.

It was found that the parasitic capacitance of the BNC cables was significant enough to present enough charge to break down the gate oxide of the transistors measured. Therefore, it was necessary to use a pull-down resistor to limit the charging of the

parasitic capacitances while the gate and drain bias were applied. The procedure is depicted in Figure 3-3. Initially locations A, B, C and D are all disconnected. The BNC capacitances are charged to V_{DD}, and the gate and drain voltages are resistively tied to ground. Location A is connected first, pulling the voltage on the gate-side BNC cable's parasitic capacitance down to $\frac{100\Omega}{R_2+100\Omega}V_{DD}$. Location B is then connected, pulling the voltage down a little further (at this point the gate voltage measured was about $84mV$). Location A is then disconnected, and the gate voltage increases to the applied bias ($\approx 1.25V$). The same procedure is then repeated on the drain side, connecting first D, then C, and then disconnecting D. The gate and drain voltages were monitered at all times during the connecting procedure. Breakdown of the gate oxide can be detected by any significant drop in the measured gate voltage. After noise measurements, the order of the procedure is reversed to disconnect the device from bias.

It was also observed that disconnection of the bias resistor network on the drain side can create a high voltage transient on the gate side which is significant enough to break down the oxide. Therefore, between noise measurements at different drain bias it is necessary to remove the bias network connections to both the drain and gate before replacing R_3.

3.2 Measured Devices

Four devices were characterized in this work. Measured were long ($2.33\mu\mathrm{mL_G}$) and short ($0.09\mu\mathrm{mL_G}$) transistors, processed the same way in the same fab, with both SOI starting substrate material and bulk substrate material.

Figures 3-4 and 3-5 show the gate controlled I-V characteristics of the short n-channel bulk device, as measured using an HP4145 semiconductor parameter analyzer. Figure 3-6 shows the drain controlled I-V characteristics. Figure 3-7 shows the drain current noise measured at several drain bias points with the gate strongly inverted.

Figures 3-8 through 3-11, Figures 3-12 through 3-15, and Figures 3-16 through 3-19 show the similar measurements for the short channel SOI MOSFET, and long channel bulk and SOI MOSFETs, respectively.

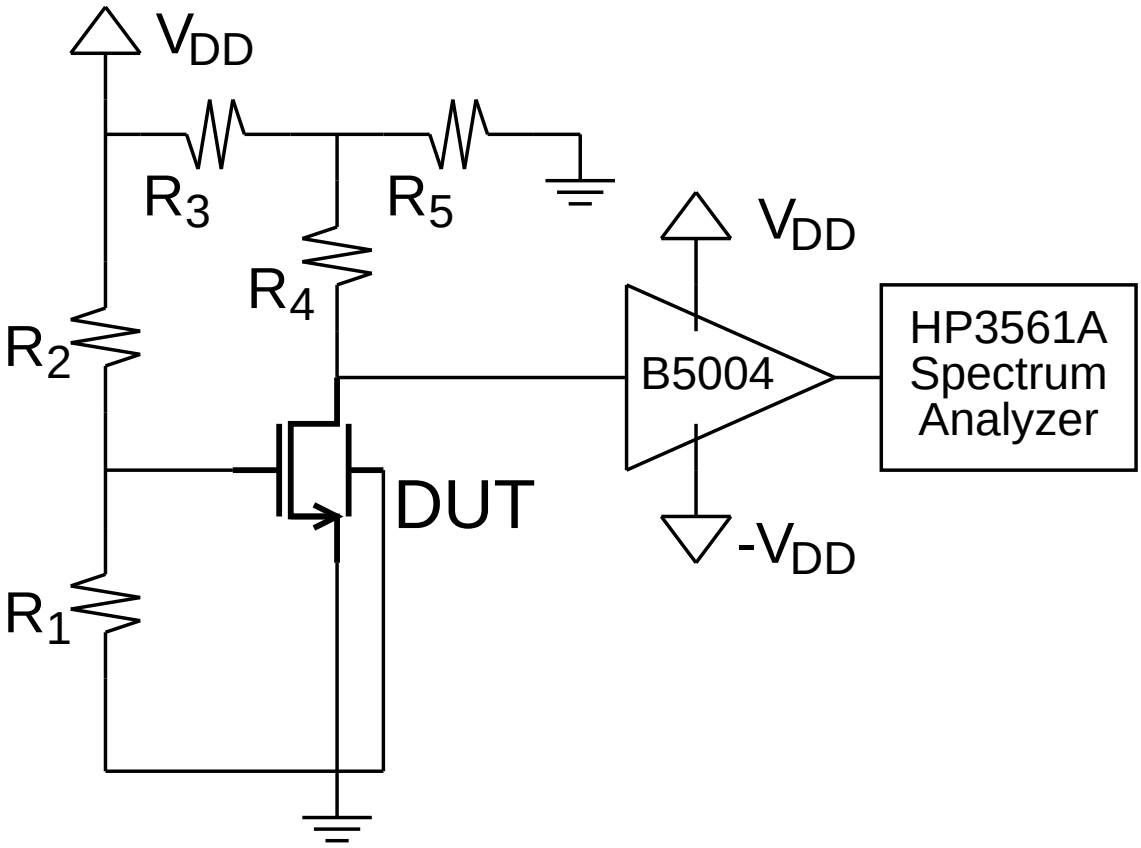

Figure 3-1. Circuit used for bulk and SOI device noise measurements.

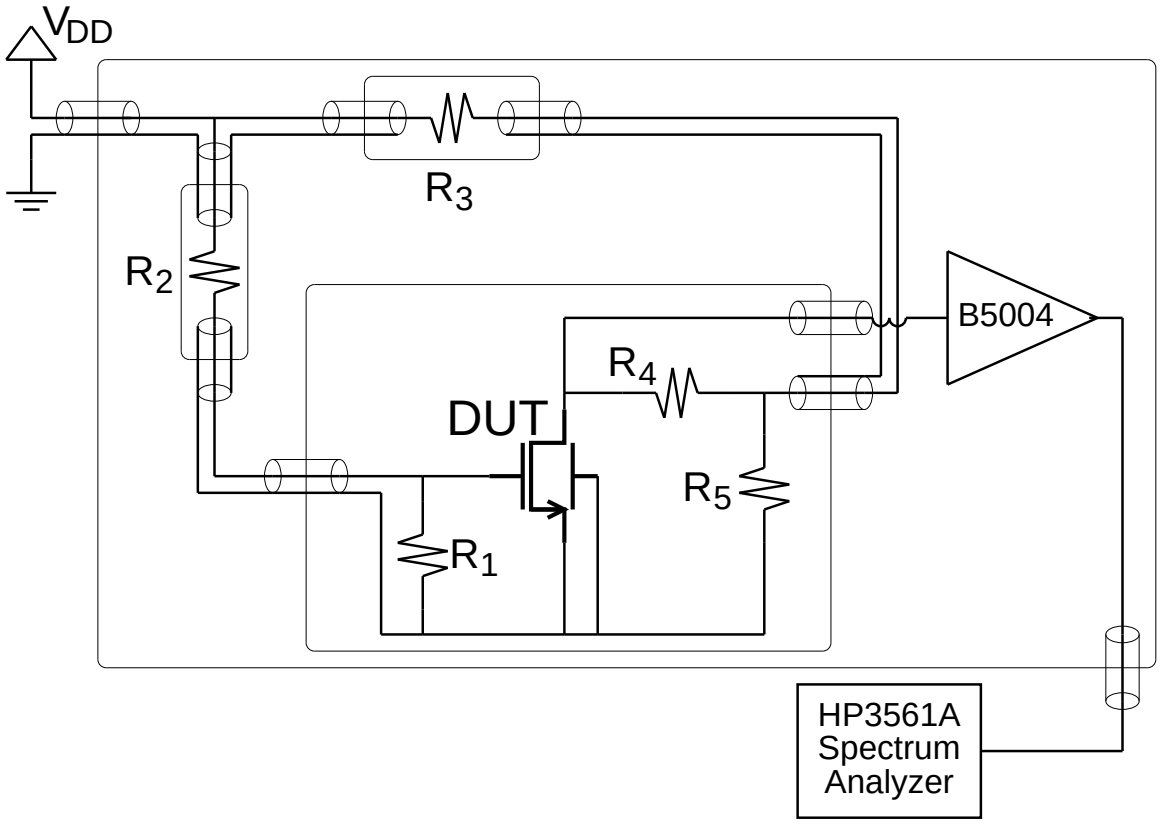

Figure 3-2. Physical layout of circuit showing the critical path of electrical connections.

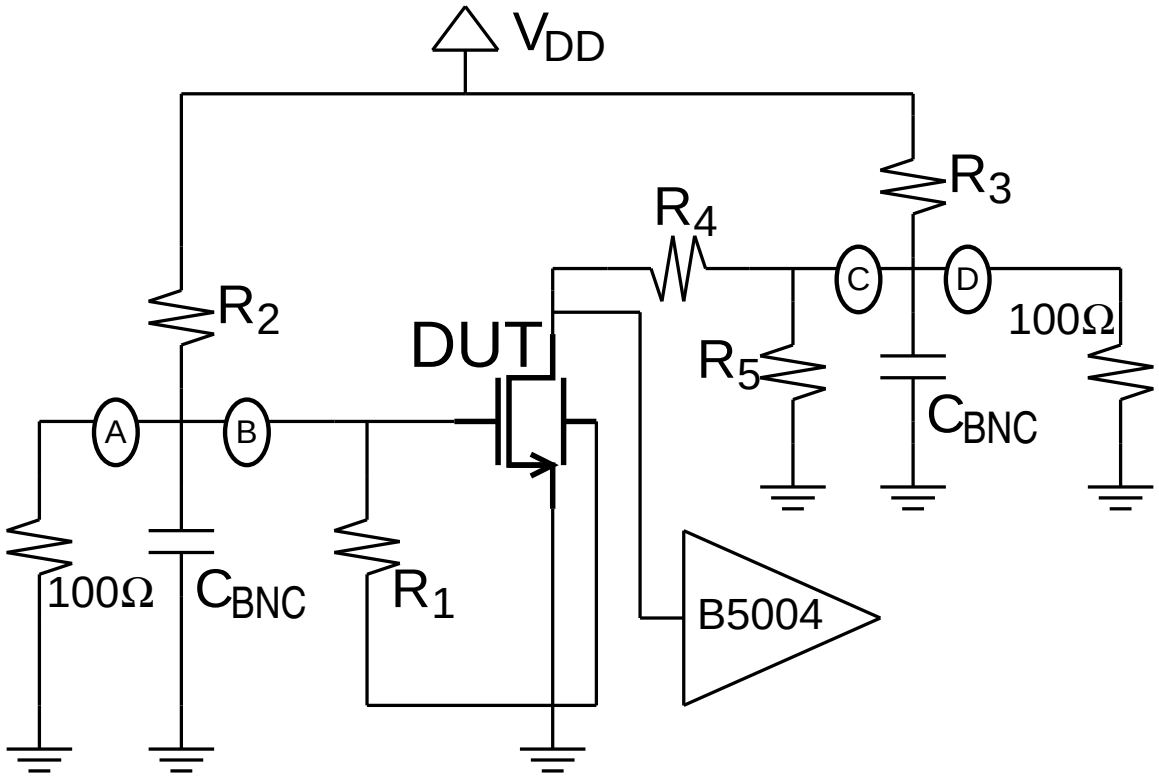

Figure 3-3. Connection scheme to ensure the avoidance of dielectric breakdown.

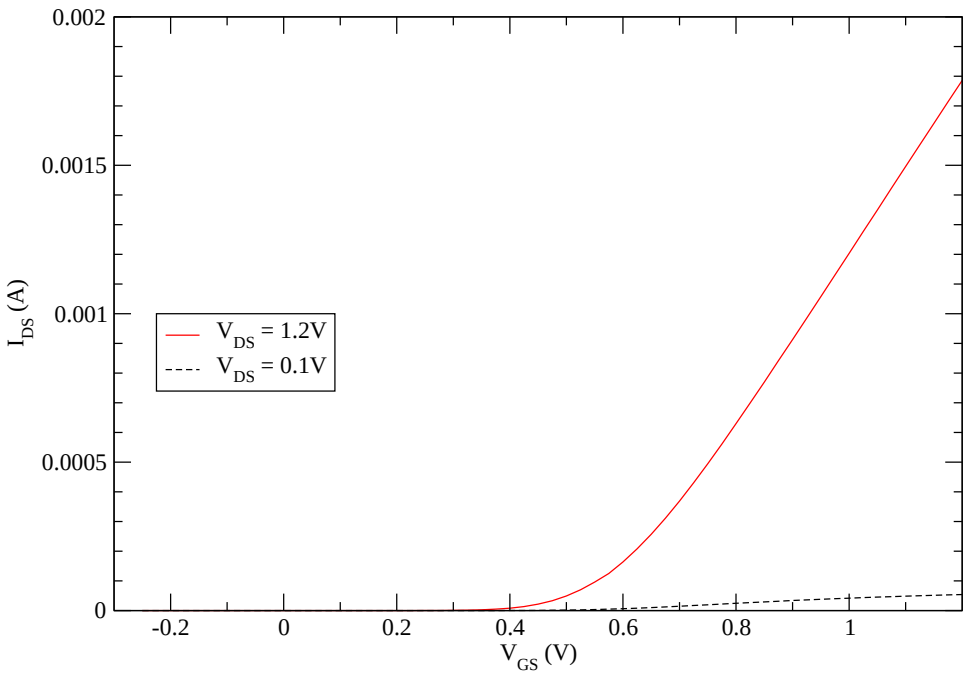

Figure 3-4. Gate controlled I-V characteristics of the $3.2\mu m$ x $90nm$ n-channel bulk MOSFET, in the linear and saturation conditions.

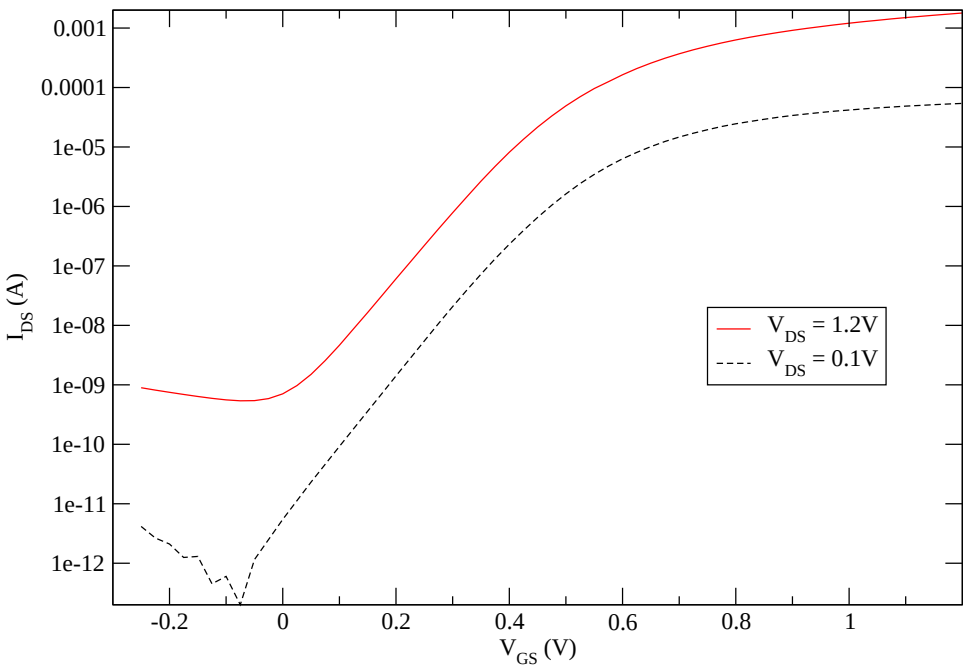

Figure 3-5. Gate controlled I-V characteristics of the $3.2\mu m$ x $90nm$ n-channel bulk MOSFET, in the linear and saturation conditions, on a logarithmic scale.

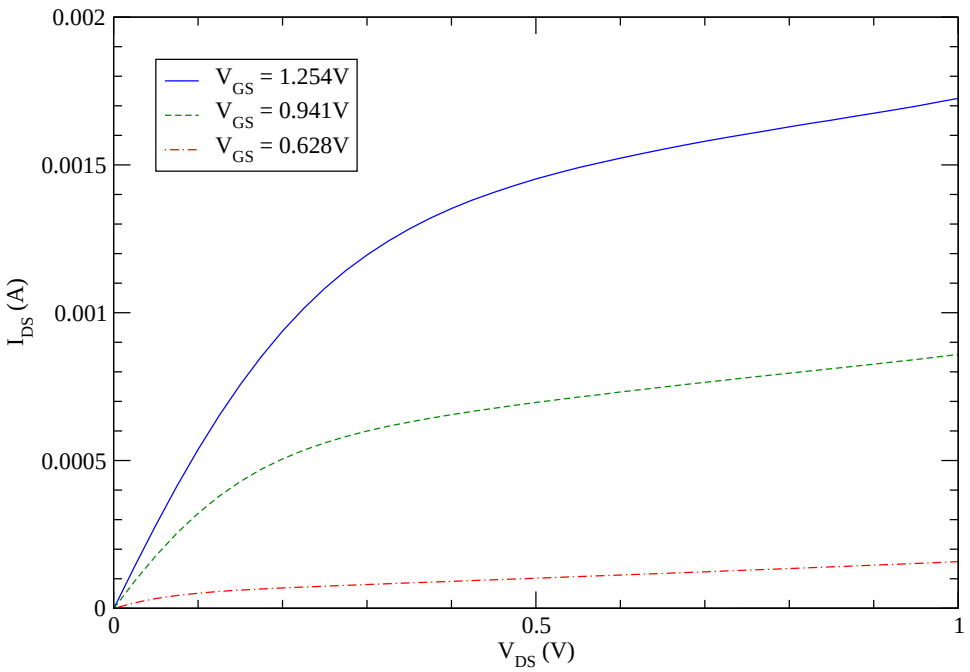

Figure 3-6. Drain controlled I-V characteristics of the $3.2\mu m$ x $90nm$ n-channel bulk MOSFET, in the linear and saturation conditions.

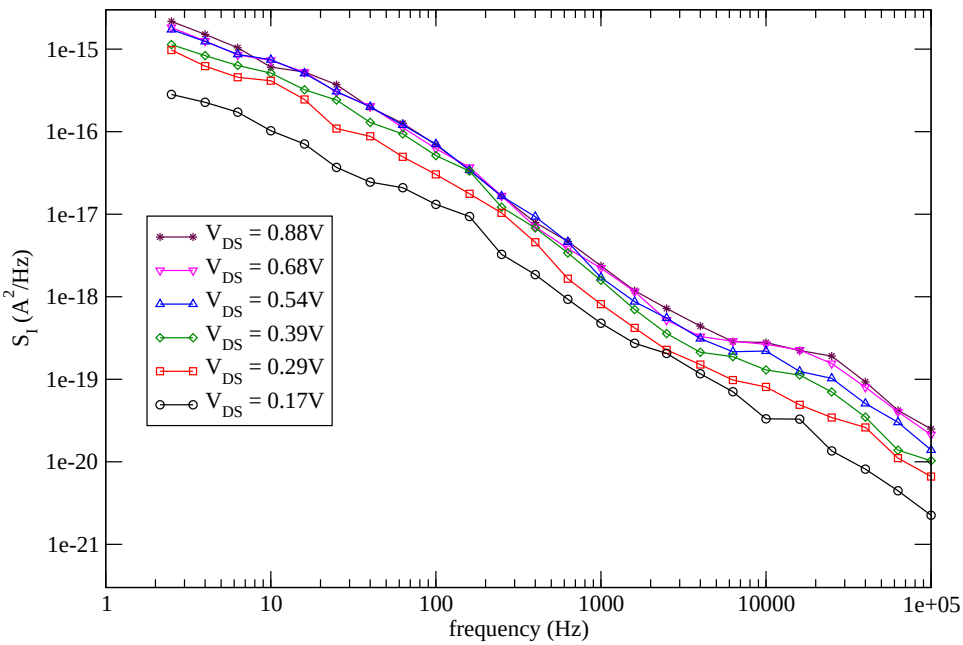

Figure 3-7. Drain current noise of the $3.2\mu m$ x $90nm$ n-channel bulk MOSFET, with $V_{GS} \approx 1.25$V.

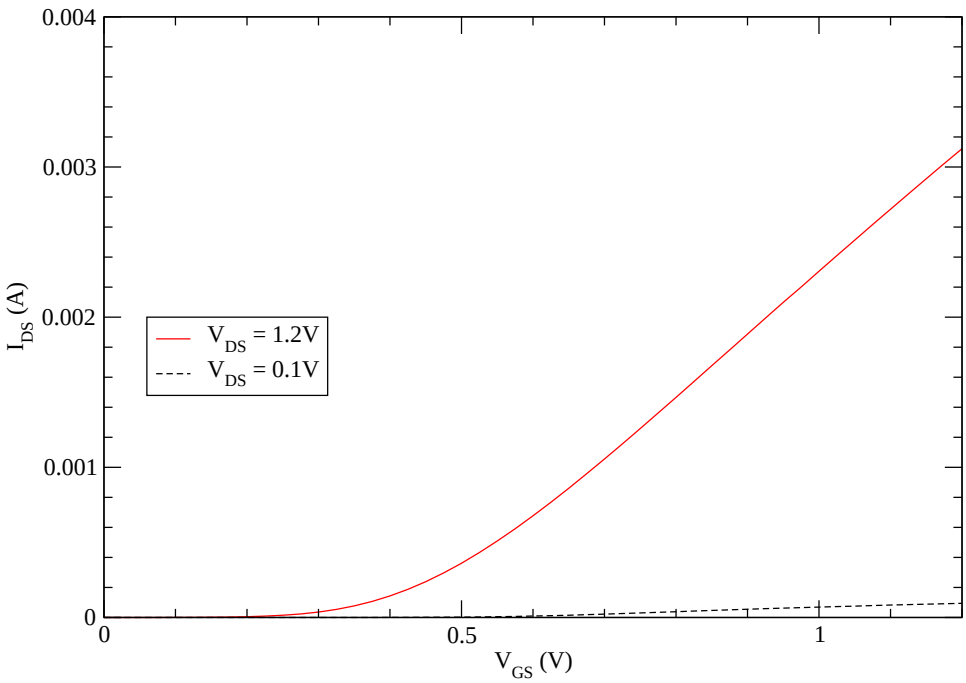

Figure 3-8. Gate controlled I-V characteristics of the 4.8μm x 90nm n-channel SOI MOSFET, in the linear and saturation conditions.

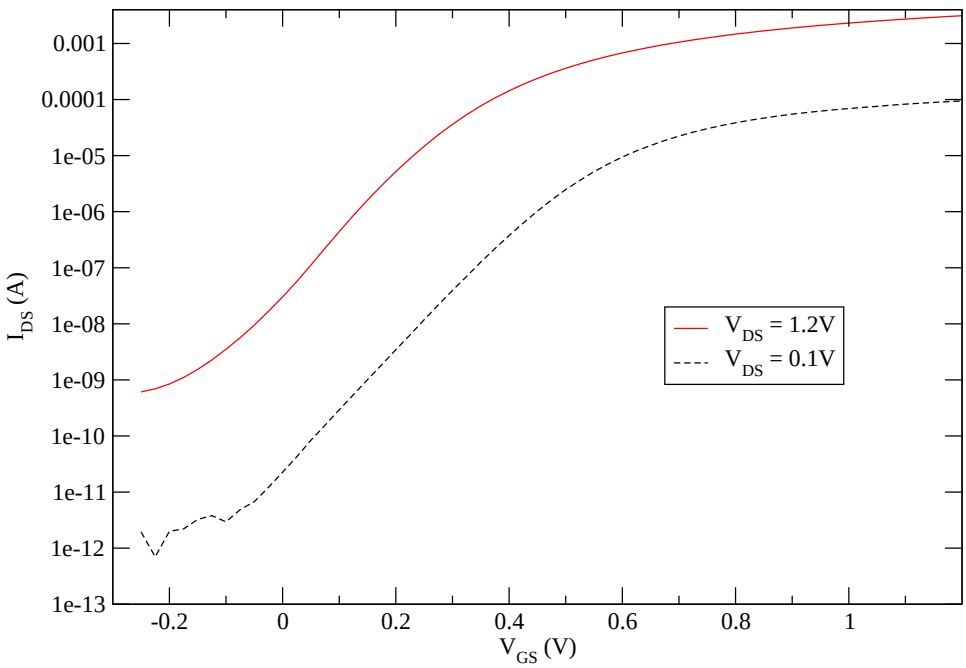

Figure 3-9. Gate controlled I-V characteristics of the $4.8\mu m$ x $90nm$ n-channel SOI MOSFET, in the linear and saturation conditions, on a logarithmic scale.

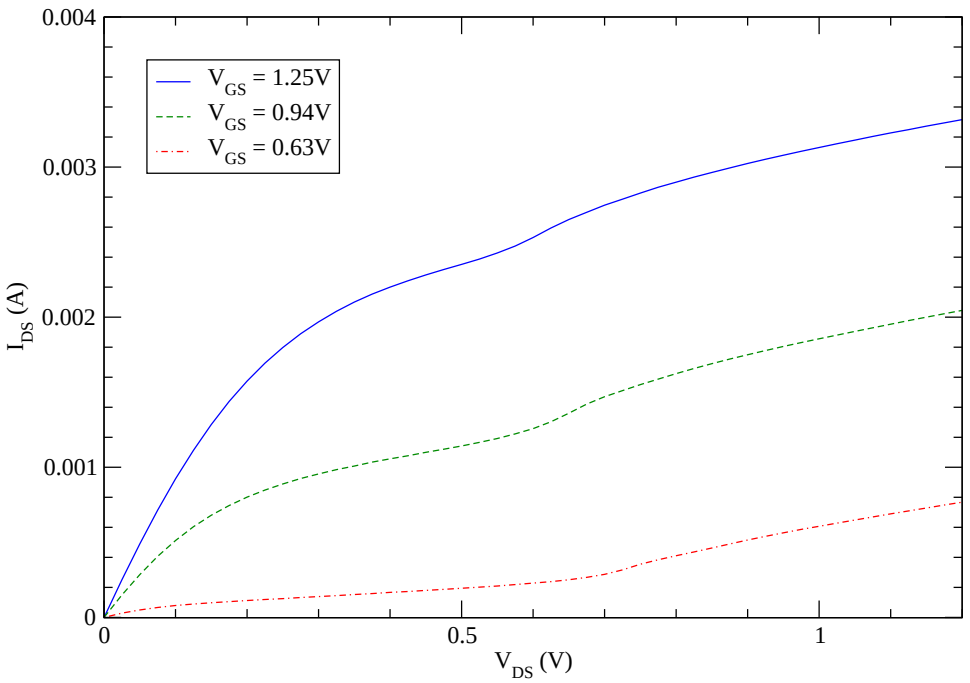

Figure 3-10. Drain controlled I-V characteristics of the 4.8μm x 90nm n-channel SOI MOSFET, in the linear and saturation conditions.

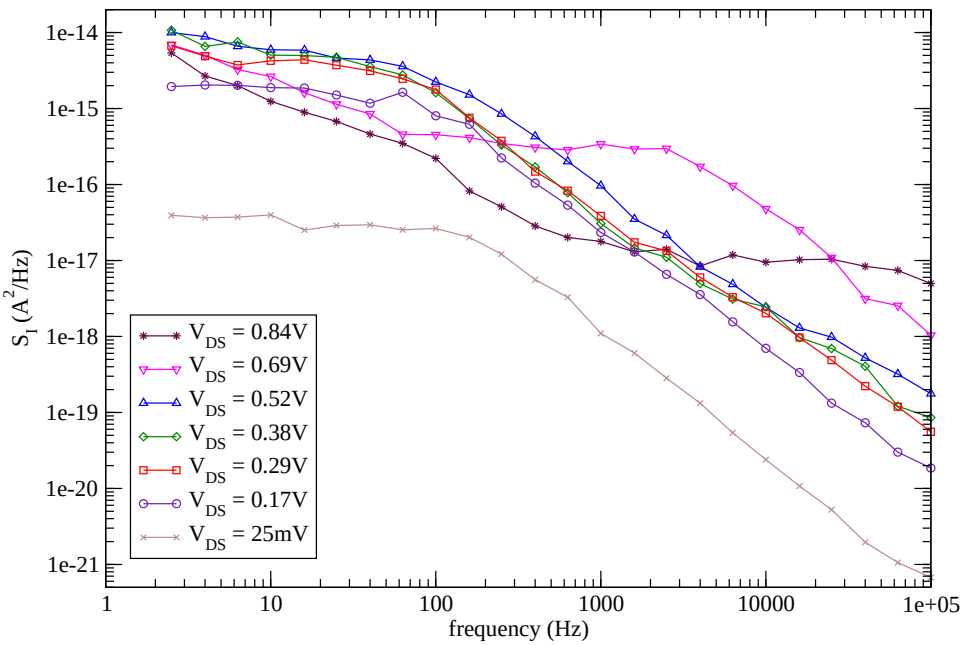

Figure 3-11. Drain current noise of the $4.8\mu m$ x $90nm$ n-channel SOI MOSFET, with $V_{GS} \approx 1.25$V.

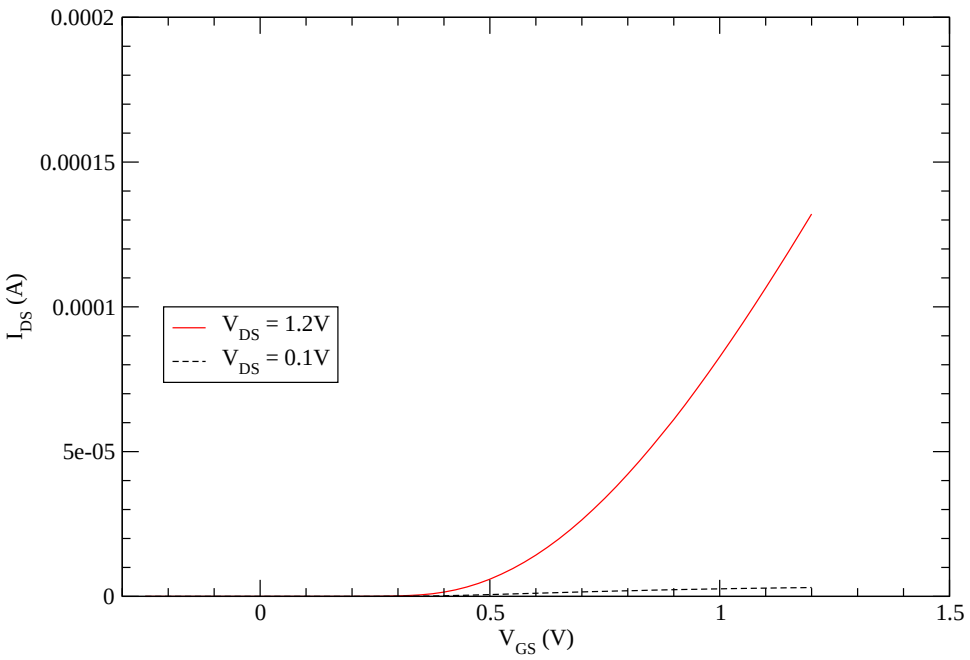

Figure 3-12. Gate controlled I-V characteristics of the $3.2\mu m$ x $2.33\mu m$ n-channel bulk MOSFET, in the linear and saturation conditions.

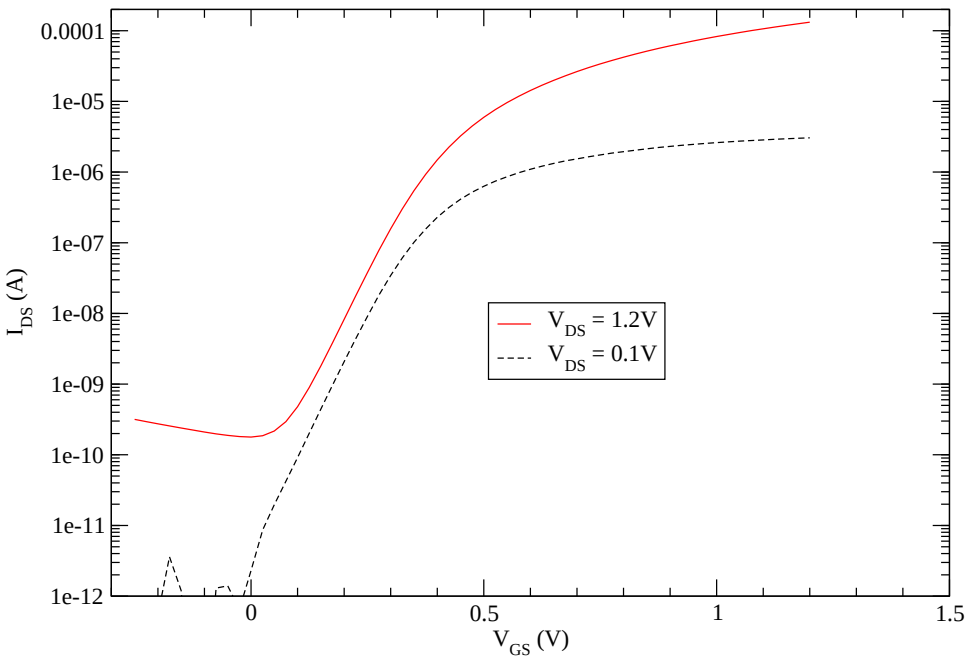

Figure 3-13. Gate controlled I-V characteristics of the $3.2\mu m$ x $2.33\mu m$ n-channel bulk MOSFET, in the linear and saturation conditions, on a logarithmic scale.

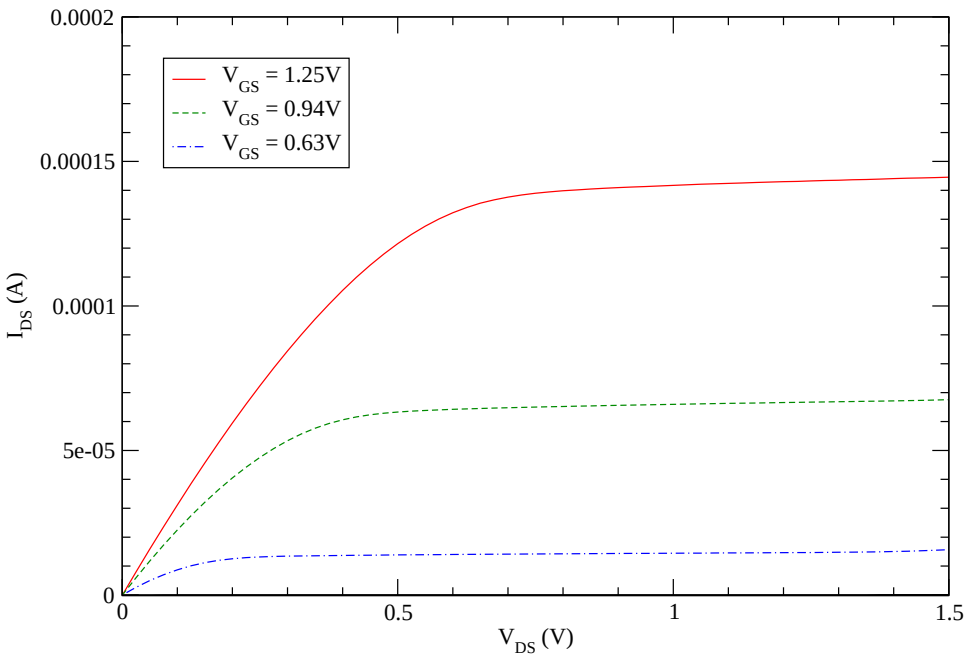

Figure 3-14. Drain controlled I-V characteristics of the 3.2μm x 2.33μm n-channel bulk MOSFET, in the linear and saturation conditions.

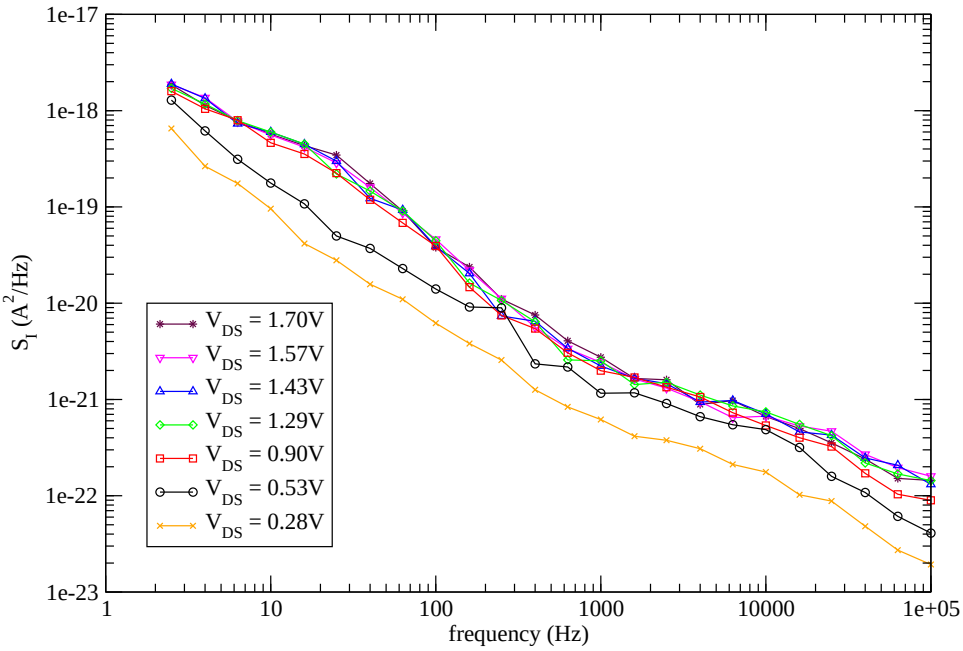

Figure 3-15. Drain current noise of the 3.2μm x 2.33μm n-channel bulk MOSFET, with $V_{GS} \approx 1.25$V.

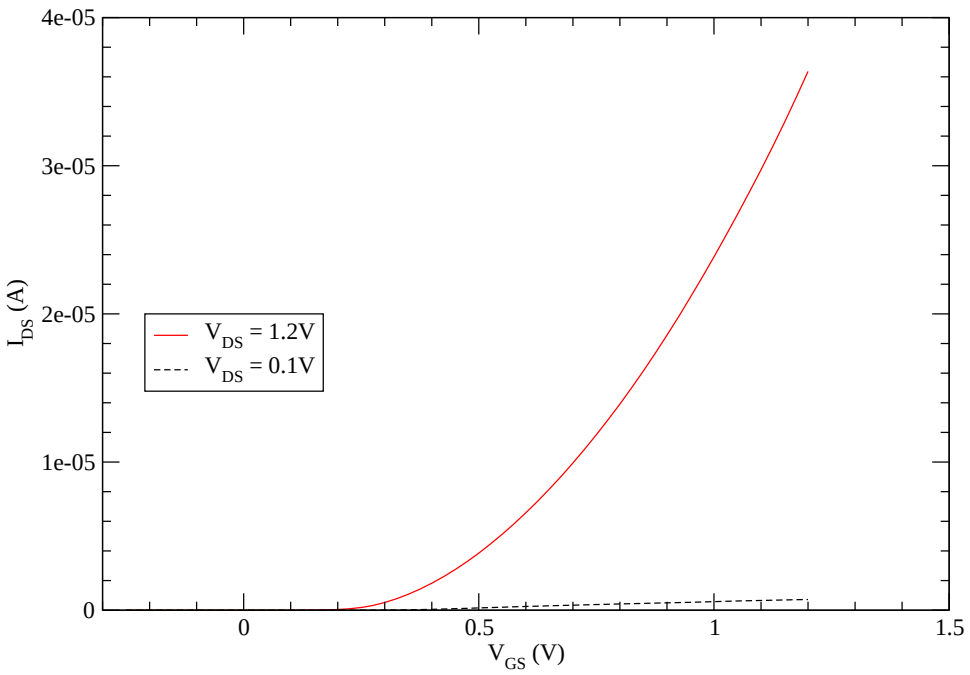

Figure 3-16. Gate controlled I-V characteristics of the $0.6\mu m$ x $2.33\mu m$ n-channel SOI MOSFET, in the linear and saturation conditions.

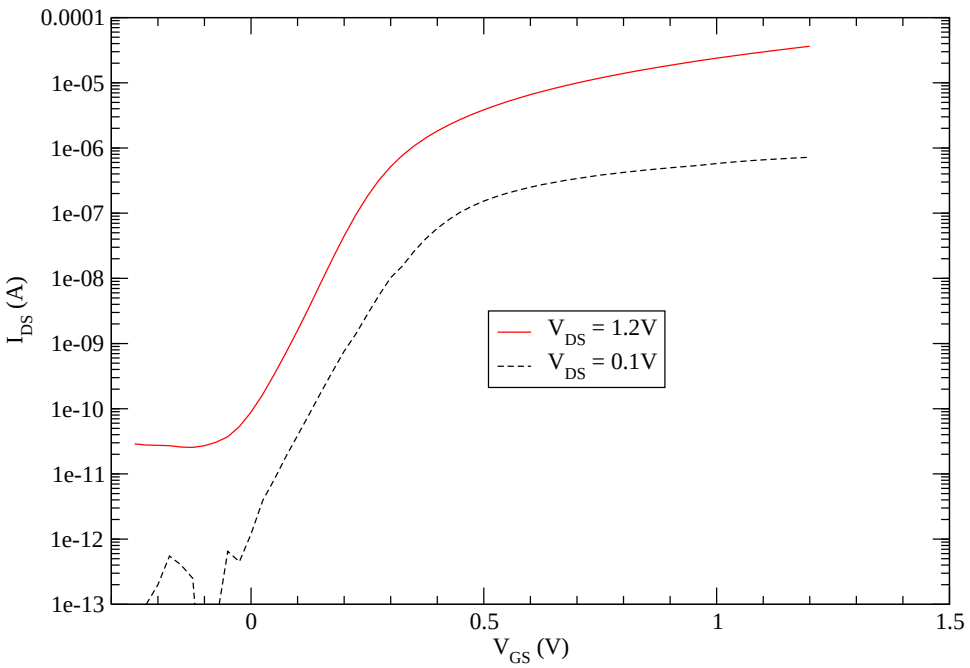

Figure 3-17. Gate controlled I-V characteristics of the $0.6\mu m$ x $2.33\mu m$ n-channel SOI MOSFET, in the linear and saturation conditions, on a logarithmic scale.

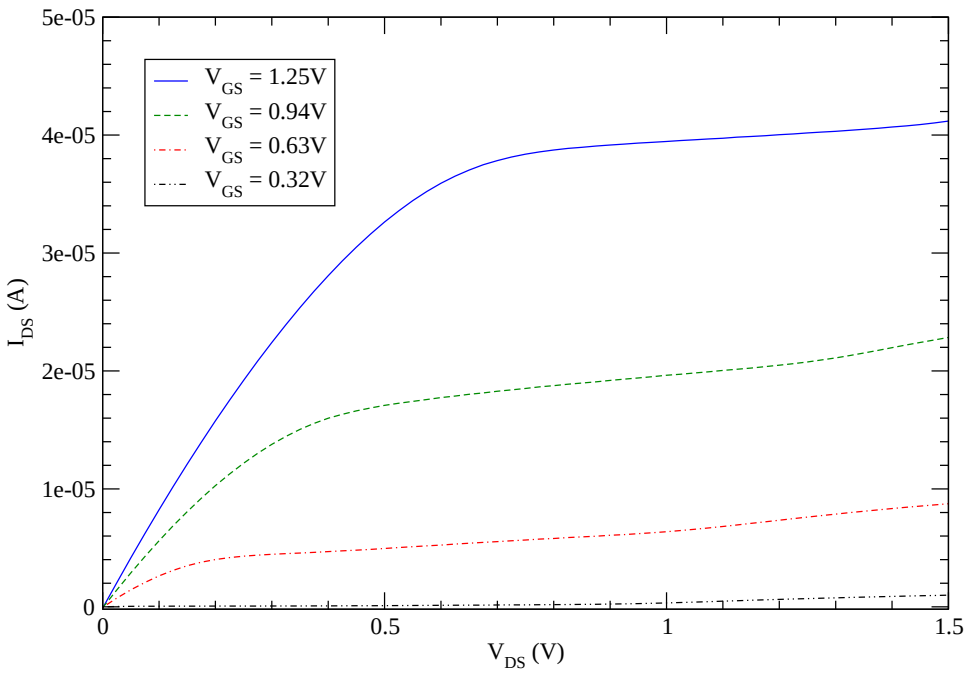

Figure 3-18. Drain controlled I-V characteristics of the $0.6\mu m$ x $2.33\mu m$ n-channel SOI MOSFET, in the linear and saturation conditions.

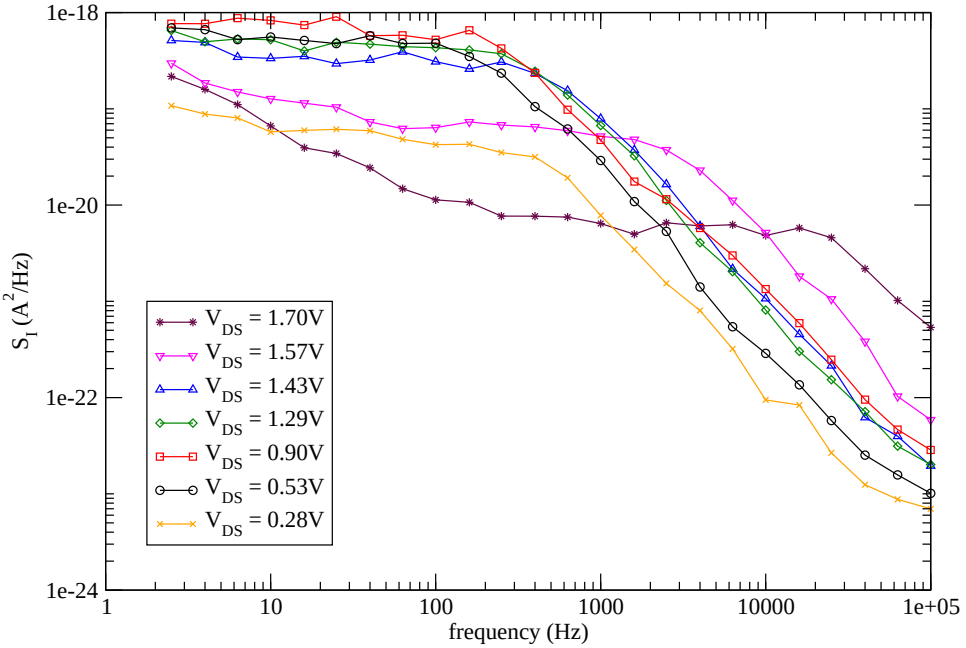

Figure 3-19. Drain current noise of the $0.6\mu m$ x $2.33\mu m$ n-channel SOI MOSFET, with $V_{GS} \approx 1.25$V.

CHAPTER 4
SIMULATIONS OF MEASURED DEVICES

It is a primary goal of this work to gain insight into the physics of the noise of the measured devices by simulating the noise using FLOODS and to compare to the measured results. In order to do this, however, the structure of the device must be brought in to the simulation framework in some manner.

The devices used for these measurements were provided by a Semiconductor Research Corporation member company, and an example TSUPREM simulation deck that is meant to create the doping profiles and oxide contours in the process structure was given along with the devices. This information was used with the commercial DIOS simulator (FLOOPS was not used due to Indium implants in the recipe, and DIOS is capable of generating meshes that can be simulated both with the commercial simulator DESSIS and with FLOODS) to generate a device mesh that is assumed to be an accurate representation of the doping profiles and geometric features of the devices measured.

The unknown simulation parameters of the devices were tuned to achieve agreement between simulated I-V characteristics and measured results (subject to the limitations of the physics simulated), and to give assurance that the process-simulated device mesh matches the real devices. Noise simulations were then performed using the assumptions of constant trap density in the oxide. The trap profile is then adjusted by looking at the measured noise data and attempting to ascertain the trap profile, then resimulating to achieve matching results. For the SOI transistors the velocity fluctuation noise dominates over the oxide trapping noise over much of the measurement time window, and therefore the match in oxide traps is made over a narrower range of frequencies and for fewer bias points.

Energy balance simulations could not be made to match the IV characteristics of the SOI devices, due to the extreme negative drain resistance of the resulting simulations, as discussed in the Chapter 1. As there is no hope of getting noise simulations to come

close to matching the measurements if DC simulations cannot match the DC current, drift-diffusion simulations are used here exclusively.

4.1 The 90nm Bulk MOSFET

The net doping density of the device resulting from the process simulations is plotted in Figure 4-1. The drift-diffusion simulations of the device are plotted in Figures 4-2, 4-3, and 4-4.

The device structure was reverse engineered and the simulations were tuned as follows, starting with the process recipe supplied by the providers of the devices.

First, the gate oxide thickness was modified such that the subthreshold slope of the $I_D V_G$ characteristics matches that of the measurement. The justification for variation from the provided recipe for this is that the precise oxide thickness cannot be not known, and the Philips unified mobility model which is used for low (acceleration) field mobility is used in these simulations andassumed to be accurate, especially in weak inversion (where unknown factors like surface roughness scattering don't matter) . Next the poly gate length is adjusted until the simulated $I_D V_G$ characteristics in linear and saturation regions exhibit drain-induced barrier lowering (V_{GS} offset between subthreshold linear and saturation curves) which matches that in the measured results. It is appropriate to modify the physical gate length, since the provided description of the devices was that the drawn gate length was $0.13\mu m$, and while the expected gate length after a gate trim etch was $70nm$ to $90nm$. As quantization effects are not included in these numerical simulations, it was necessary to find a way to simulate the current with the correct amount of minority carriers in the inversion layer. This was done using a fixed charge at the interface, which is adjusted to give good agreement between simulation and measurement at strong inversion and low drain bias, where the quantization effect is raising the effective threshold voltage and reducing the inversion charge, but the lateral field is not saturating carrier velocity. The coefficient of the surface roughness scattering term in the Darwish mobility model, which is process-dependent and an unknown parameter, was then modified until the I-V

characteristics match between simulation and measurement (best observed on a linear scale), from the onset of strong inversion onward. At this point, the physical structure of the device and its doping, electric field and overall inversion charge, as well as the understood mobility model, match the reality of the structure and the physics involved with the notable exception of the shape of the inversion layer, due to the incomplete modeling of the quantizaiton effects.

After the device simulations (process and device) were modified to match the I-V characteristics, noise simulations were performed for comparison to the measured results. A comparison of the noise in this device versus that simulated for uniform oxide trap density is given in Figure 4-5. For this simulation, it is also clear from the plots of noise contribution due to traps along the oxide in Figure 4-6 that with increasing drain bias, the traps near the source end of the channel increase in their effect on the noise, where as the traps toward the drain end decrease in their effects. To match the results of the noise measurements, the slope of the overall $1/f$-like noise was matched by adjusting the parameter η of the following oxide trap equation [29].

$$N_{tox} = N_{tox0} * exp(\eta * \delta x) + N_{disc} \tag{4–1}$$

where N_{tox0} is the peak volumetric density of traps at the surface, η is the constant of logarithmic proportionality, δx is the distance to the interface, and N_{disc} represents the effective density of discrete traps that were added to match the bumps in the measured characteristics, with their distance from the interface set to bring about a match of the cutoff frequency of the resulting Lorentzian, and the lateral position set to match the drain bias dependence of the Lorentzian. The local effective trap density is set to match the low frequency magnitude of the Lorentzian. There appear to be traps at three grid locations near the source end of the channel. Finally, by observing the drain dependence of the parts of the noise measurements not dominated by any obvious Lorentzian, the N_{tox0} parameter was adjusted to give a Gaussian distribution in the lateral direction, centered

toward the drain end where the drain bias dependence is depressed. The peak value of N_{tox0} used is $10^{14} cm^{-3}$. This background component is interpreted as a few traps in the drain region for which there is not sufficient information in the measured characteristics to discern a finer trap placement (the magnitude of the noise in these traps is lower thanthat of the traps near the source, and the cutoff frequency of their associated Lorentzia is not discernable in the measured data). The "spread out" Gaussian distribution in y direction and exponential increase in x direction toward the gate approximates the effect of discrete traps near the drain. The trap distribution used to fit the measured results is depicted in Figure 4-7. Trap 1 has a density of $5 \cdot 10^{18} cm^{-3}$, corresponding to a total number of 4 traps in the $3.2 \mu m$ wide device. Traps 2 and 3 are in neighboring nodes and have a density of $2 \cdot 10^{17} cm^{-3}$, corresponding to a total number of 0.5 traps each. This is interpreted as being one single trap, though the spread of the bump in the measured noise data is too wide to be a single Lorentzian. The spread is due either to the carriers not always tunneling directly perpendicular to the interface, or to carriers tunneling from some position in the inversion layer other than right at the surface. This trap distribution is unique, as the lateral position of these traps determines the drain bias dependence of the bump, and the position from the channel determines the cutoff frequency. The position of these traps therefore is as determinate as the modeling of Drift-Diffusion and process simulation allows. Consideration of quantization effects results in trap locations which are a little closer to the physical interface, as is shown later in this section. The distributed trap distribution is a gaussian distribution in the y direction, with a peak and standard deviation. In the x direction it is exponential, as in Equation 4–1. It has a peak density near the surface of $10^{14} cm^{-3}$ and a lateral spatial standard deviation of $10 nm$, centered along the channel below the center of the oval depicted in the figure. The factor η needed to match the greater than $1/f$ dependence in frequency was $4.5 \cdot 10^{7} cm^{-1}$. If the average trap density throughout the contributing region of this oxide is assumed to be approximately $2 \cdot 10^{15} cm^{-3}$ throughout the thickness of the gate oxide over $2 * \sigma_y$ on each

side of the peak value, this gives an equivalent of approximately 15 additional, individually indistinguishable traps. They are described here as being individually indistinguishable because if they are distributed in any arrangement approximating this distribution, they will provide the background $1/f$-like noise necessary to fit the measurement, and the individual Lorentzia from each trap is not significant enough to be individually observed in the final total noise.

The final fit of the simulated measurements to the measured data is shown in Figure 4-8. Significant diffusion noise was not observed within the measurement time window.

It is of interest to consider what the error in the 3 trap positions and energies are due to neglecting the shape of the carrier distribution in the inversion layer associated with the quantization effect. A first-order 1-D vertical solution to the SWE was computed in the inversion layer under each of the simulated oxide traps. This solution was obtained by solving the 1-D SWE using the shooting method. In one dimension the SWE equation is given as follows.

$$\frac{\delta^2\psi}{\delta x^2} = \frac{2m}{\hbar^2}\left(E - V(\vec{r})\right)\psi \tag{4–2}$$

This is integrated to get $\delta\psi/\delta x$ and ψ as a function of position, assuming some value for E. The integration starts with a value of zero for ψ and a small finite, arbitrary value for $\delta\psi/\delta x$ at one end of the solution, where E_C is higher than E and ψ is expected to go to zero. If E is an allowed Eigenvalue, ψ will go to zero at the other end as well, and will diverge to a very large value (positive or negative) if E is too high or too low. E is varied and the solution is tested until a valid Eigenvalue and Eigenfunction are found. Unless E is very close to a valid Eigenvalue, divergence of the solution usually causes numerical overflow, so an arbitrary precision software package for the Perl programming language was used to compute the solution, until the solution was close enough to switch to faster floating point fixed precision computations. Ideally, the computed wavefunctions and energy values would be used to reshape the inversion layer, and the transport model would

be re-solved, iterating until the SWE solution for the inversion layer and the simulated potential well and inverstion carrier distribution are in complete agreement. However, as the fixed interface charge has adjusted the electric field in the inversion layer to give agreement for the IV curves and the overall number of inversion carriers is therefore already in agreement, the shape of the potential well should not change too dramatically with iteration, and this solution should be correct to first order, sufficient to compute an error correction for these three traps.

This solution is represented by the distribution shapes depicted in figures 4-9 and 4-10. The error in the trap energy is approximated by the increase in the minimum allowed electron energy since the carriers are tunneling from the first subband rather than from the classical conduction band edge. The error in the trap position can be approximated by assuming that carriers tunnel from the most likely inversion electron position, at the peak of the electron wavefunction, rather than tunneling from the surface. To get the same tunneling probabilities (and the same Lorentzian cutoff frequency) the trap must be closer to the surface to get the same overall decrease in wavefunction value, as follows.

$$\frac{\psi_{peak}}{\psi_{trap}} = \frac{\psi_{surf}^{classical}}{\psi_{trap}^{classical}} \tag{4–3}$$

The computed errors suggest the trap position and energy are $4.66\mathring{A}$ closer to the surface and $0.104eV$ higher in energy for trap 1, $4.26\mathring{A}$ closer and $0.159eV$ higher for trap 2 and $4.29\mathring{A}$ closer and $0.159eV$ higher for trap 3.

To summarize, a trap distribution has been found for which the drift-diffusion model, augmented with direct band-to-trap tunneling physics, results in noise simulation which matches the measured noise data with very good agreement. Shooting methods show the error due to the semi-classical inversion layer shape and classical energy distribution, and correction terms are computed and withing the range of expected values. From this comparison the conclusion can be drawn that the Lorentzia observed in the noise

measurements originate from trapping of carriers at a small number of traps in the gate oxide in the vicinity of the source/body metallurgical junction.

4.2 The 90nm SOI MOSFET

For the $90nm$ SOI device, the net doping density is plotted in Figure 4-11. The floating body effect makes the observation of short channel effects, and therefore the reverse engineering of such a device, more difficult. However, since the bulk and SOI devices were both processed in the same lot in the same fab process, and with only different starting material, it is assumed that the poly gate lengths and oxide thickness are identical between the bulk and SOI devices. Since the starting material was different, however, there may be slight differences in the quality of the oxide interface under the gate, and the resulting surface scattering mobility model, electric field and therefore fixed interface charge to approximate quantization effects. This appears to be the case, as it was necessary to modify the surface roughness scattering parameters in the Darwish model and the fixed interface charge to get the I_DV_G characteristics to match for the linear case as well as they did for the $90nm$ bulk transistor. The I_DV_G characteristics match the measured results well in strong inversion, as shown in Figure 4-12.

Since the SOI device is highly sensitive to the charging of the floating body by impact ionization and the standard drift-diffusion based Van Overstraeten impact ioinization model [42] is known to overestimate the ionization rate in scaled devices [16], it is necessary to modify the impact ionization rate coefficients, balanced with Shockley Reed Hall recombination, in order to get the right overall amount of floating body charging as a function of bias and to get the simulated I_DV_D characteristics to match the measured ones with good agreement. To obtain a decent match for these highly scaled devices using this model, the B parameter was increased from the classical $1.231 \cdot 10^6 V/cm$ to $3.8 \cdot 10^6 V/cm$, and the A parameter was reduced from $7.03 \cdot 10^5 cm^{-1}$ to $1.3 \cdot 10^3 cm^{-1}$. The sizable reduction of the A parameter is in part to the reduction of the overall impact ionization rate, but largely also due to the exponential nature of the dependence on the B parameter,

which was increased to raise the onset of impact ionization to a higher electric field (over short distances). The $I_D V_D$ characteristics simulated using drift-diffusion are shown in Figure 4-13. The modified impact ionization rates are also responsible for the saturation matching of Figure 4-12.

After a good match was obtained for the DC simulations, noise simulations were also performed. First considered is the oxide noise. The oxide noise in the measured data is mostly swamped out by the diffusion Lorentzia, but some oxide noise is apparent at high drain biasand low frequency ($0.69V$ and $0.84V$ V_{DS}, between $1Hz$ and $100-600Hz$), where the impact ionization shifts the excess diffusion Lorentzia to low enough zero-frequency magnitude that the oxide noise can exceed it. It is also apparent at high frequency, for moderate drain bias ($0.27V$, $0.38V$, and $0.52V$ V_{DS}, above $10kHz$), where the Lorentzia rolls off fast enough (approximately $1/f^2$) that at high frequencies it is exceeded by the oxide noise. These Lorentzia are at the same cutoff frequency as the Lorentzia caused by the traps in the bulk device, so the oxide noise is computed by using the trap positions used for the bulk devices (depicted in Figure 4-7), then tuning the trap densities and the parameter η to match the increased overall slope of the SOI device's oxide noise, as plotted in Figure 4-15. Trap 1 (as in Figure 4-7) has a density of $5 \cdot 10^{19} cm^{-3}$, corresponding to a total number of 4 traps in the $4.8\mu m$ wide SOI device. Traps 2 and 3 have a density of $1.2 \cdot 10^{19} cm^{-3}$, corresponding to a total of 1 trap. The peak value of N_{tox0} and η used to match the background noise as in the bulk device were $1.2 \cdot 10^{15} cm^{-3}$ and $2.6 \cdot 10^{7} cm^{-1}$, respectively. The similarities between the bulk and SOI device oxide noise are striking, and indicate that the traps near the source/body junction under the gate are most likely a function of the gate oxidation recipe, and/or subsequent processing steps. This does not say anything about the traps elsewhere in the oxide, however, as this is the region of oxide in which the measured oxide noise is highly sensitive to traps within the measurement time window ($1Hz$ to $100kHz$).

As in the case of the bulk device's simulations, the shooting method is used to quantify the error in this result due to the shape and energy level of the inversion layer confined in the z direction. Figures 4-16 and 4-17 depict the shape and energy level of the first subband in the inversion layer under the traps. The carriers tunnel from the first subband rather than from the conduction band edge, so these simulations suggest that trap 1 is $134meV$ higher in energy than the classical model suggests. By matching the ratios of the wavefunction value at the peak of the wavefunction and at the trap position to that of the classical model (as in Equation 4–3), these simulations also suggest that trap 1 is $4.59\AA$ closer to the surface than suggested by the classical model. The same error corrections are computed for the other traps and suggest that traps 2 and 3 are $196meV$ higher in energy (they are located at the same y position, so carriers tunnel from the same first subband) and $4.23\AA$ and $4.25\AA$ closer to the surface, respectively.

For the velocity fluctuation noise, the simulated Lorentzia are plotted in Figure 4-18. The source of this noise is the shot noise of the source/body junction, located primarily on the source side of the metallurgical junction, as depicted in Figure 4-19. Here it is useful to discuss the relationship between the bulk recombination lifetimes of electrons and holes and the impact ionization parameters, which together set the IV characteristics shown in Figure 4-13. If the recombination lifetimes of electrons and holes are halved, the parameter A of Equation 2–53 can be doubled, without affecting the floating body potential or the kink in the IV curves. The effect on the noise Lorentzia in strong saturation (dominated by the impact ionization effect) however, is to halve their zero-frequency value and double their cutoff frequency. This is in agreement with the closed-form equations derived by Workman [1] and cast here as drain current noise, as follow.

$$S_I^{Lor}(0) = \frac{4(mkTg_{db})^2}{q(I_{GRtD} + I_{Gi})} \tag{4–4}$$

$$f_C = \frac{q(I_{GRtD} + I_{Gi})}{2\pi mkTC_B} \tag{4–5}$$

The expression $S_I^{Lor}(0)$ is the zero-frequency value of the Lorentzian, and f_C is the cutoff frequency, set by the first pole in the impedance of the internal body node. The subthreshold slope factor is given by m, kT/q is the thermal voltage, and g_db is the drain to body conductance. The terms I_{GRtD} and I_{Gi} represent the drain/body junction thermal generation and impact ionization currents, respectively. C_B is the total effective capacitance of the internal body node, including stray capacitances to gate, source, drain, and substrate beneath the buried oxide. This effect (scaling the impact ionization rate inversely with the recombination lifetimes) is here taken advantage of to affect the noise without affecting the IV curves, resulting in the fit of the Lorentzias' zero-frequency values at low drain bias. However, the simulated values at higher drain bias do not fit well. Therefore, the impact ionization rate parameter B in Equation 2–53 is increased slightly to $3.9 \cdot 10^6 V/cm$ to push this curve out to the right by increasing the electric field required to cause a given amount of impact ionization. While this skews the IV characteristics somewhat as plotted in Figure 4-20, its effect on these curves is significantly outweighed by the effect on the noise. An increase of 40% is sufficient to greatly increase the agreement of the noise at higher drain bias. This fit and that of the initial case are plotted in Figure 4-21. The cutoff frequency is still extremely low, as plotted in Figure 4-22. Though the cutoff frequency qualitatively decreases and increases with bias roughly as the measured data does, the value is a logarithmic average of 240 too low. Here consideration of the simulated problem to date must be considered to effect an improved fit. The DESSIS commercial simulator used in this work was limited to consider a single value for the fixed interface charge used at all Silicon/Oxide interfaces, independent of position. The fixed interface charge used for this work is an artificially high value used to compensate for quantum confinement-related reduction in inversion charge, and this is only appropriate under the thin gate oxide, where the high binding electric field reduces the number of inversion carriers. At the back gate, this high fixed charge has the effect of accumulating the p-type surface, thinning the space charge regions near the source and

drain junctions, and increasing the drain/body and source/body capacitances artificially. While this back gate accumulation has little effect on the DC IV characteristics, it is detrimental to the fit of the noise Lorentzia, as predicted by Equation 4–5. After applying a spatial dependence to the fixed surface charge in FLOODS to drive the fixed charge to zero at the back gate, increasing the impact ionization rate by a constant factor to raise the impact ionization to maintain the fit of the IV characteristics, and after rebalancing the SRH recombination lifetimes and impact ionization rates as in Table 4-1 to obtain a good fit of the low-frequency Lorentzia's magnitudes, the low cutoff frequency has been improved to within an order of magnitude, as shown in Figure 4-23.

There are unfortunately no further parameters that have been considered arbitrary and which can be tuned to increase the cutoff frequencies without further altering the fit of the zero-frequency value. In order to make this parameter have better agreement, it is necessary to deviate from the doping profile generated from the provided process description, or from the phyics of the transport model previously presented. Either is in general undesirable as the result is that the entire device structure would then be considered arbitrary. However, a small deviation is acceptable by adding some compensating donor concentration to the region at the bottom of the active device film, between the metallurgical source and drain p/n junctions and the buried oxide. This is acceptable because it does not affect the DC IV characteristics of the device, which are the primary consideration of the providers of the device, who design for digital applications and were not overly concerned with the accurate modeling of the doping profiles for noise simulation purposes. Reduction in the doping at the back of the film could be caused by transient enhanced diffusion near the bonded wafer oxide, and the IV characteristics employed by employees of the company that donated these devices would be insensitive to such an effect. This reduction in doping has the effect of further lowering the bulk capacitance, the only term in the closed form equation for cutoff frequency not present in the equation for zero-frequency value. The resulting Lorentzia exhibit increased cutoff

frequencies without altered zero-frequency values and are plotted in Figure 4-24. The final fit is improved both in low-frequency Lorentzia magnitude, and in cutoff frequency.

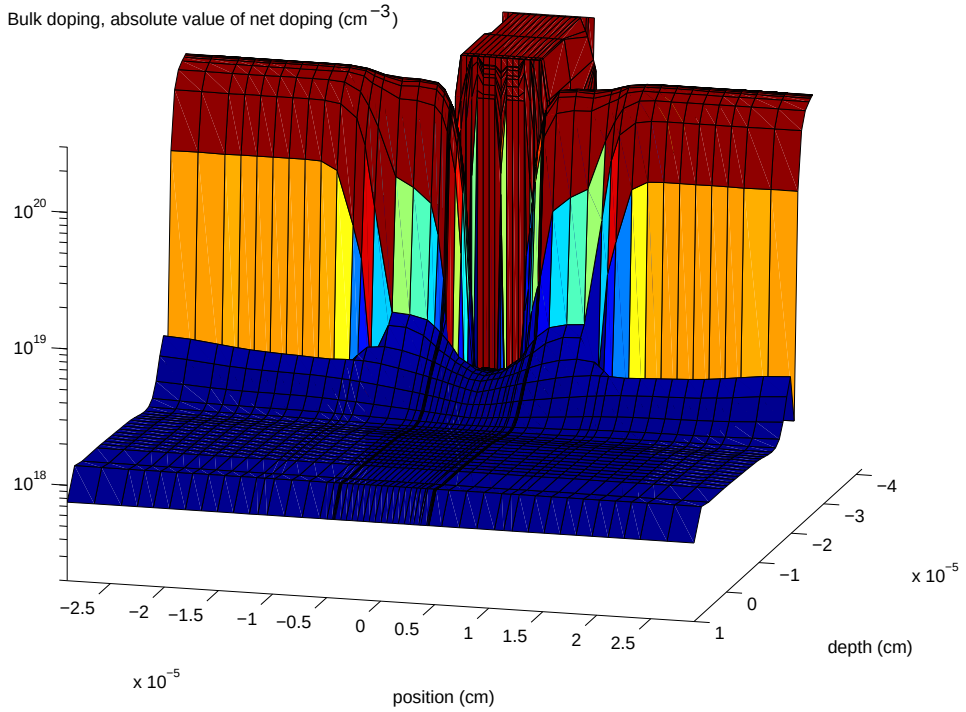

Figure 4-1. Absolute value of net doping density of the bulk MOSFET simulated in this work. The "spikish" shapes between the body doping and the steeply varying doping in the source/drain regions are due to the net doping zero crossing near the metallurgical junction, the sparseness of the grid, and the plotting on a log scale.

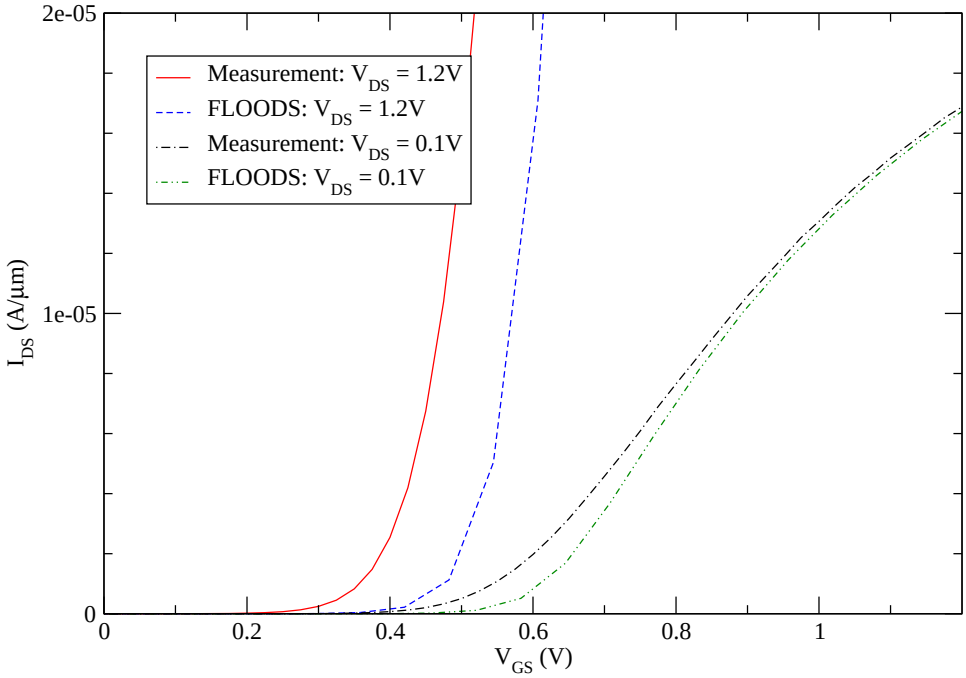

Figure 4-2. Match of simulated gate control IV characteristics for $3.2\mu m$ x $90nm$ bulk device, for $V_{DS} = 0.01V$ and $V_{DS} = 1.2V$.

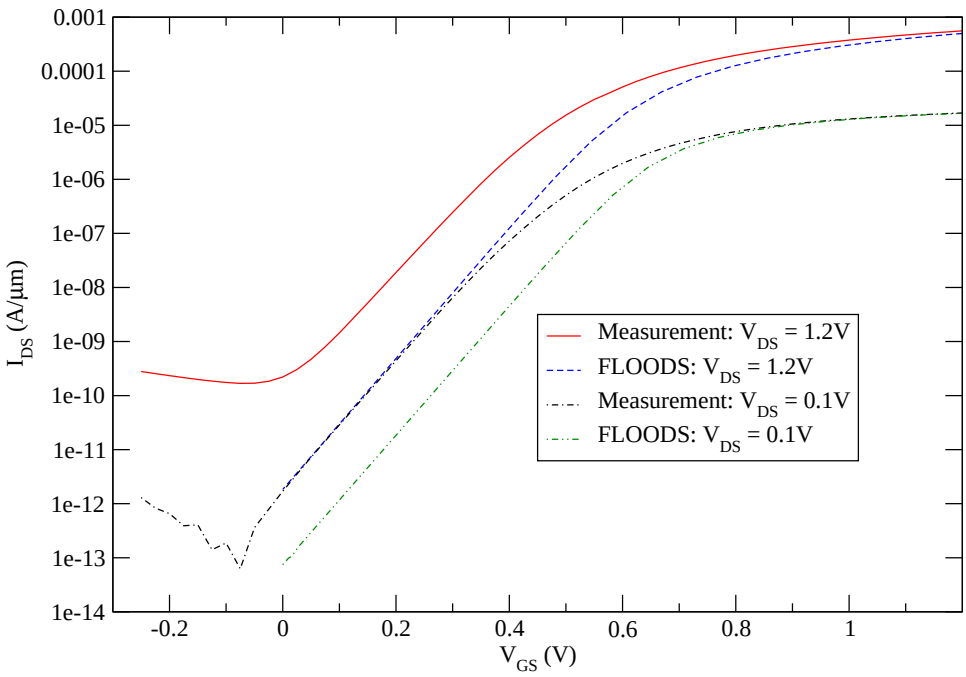

Figure 4-3. Match of simulated gate control IV characteristics for $3.2\mu m$ x $90nm$ bulk device, for $V_{DS} = 0.01V$ and $V_{DS} = 1.2V$, on a logarithmic scale.

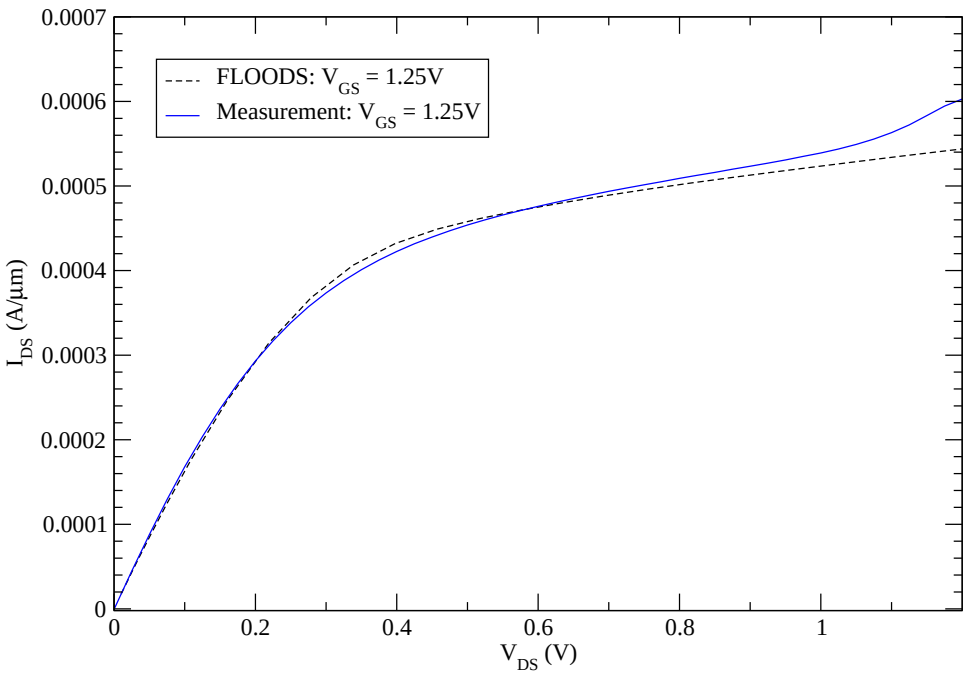

Figure 4-4.]
Match of simulated drain control IV characteristics for $3.2\mu m$ x $90nm$ bulk device, for $V_{GS} = 1.25V$.

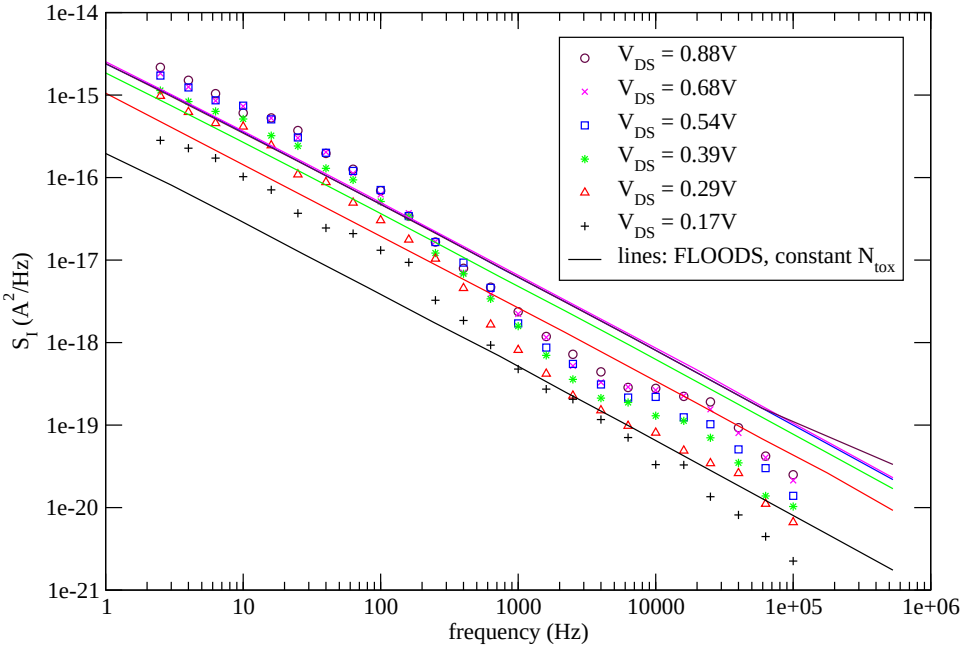

Figure 4-5. Match of simulated noise characteristics for $3.2\mu m$ x $90nm$ bulk device with assumed constant trap density.

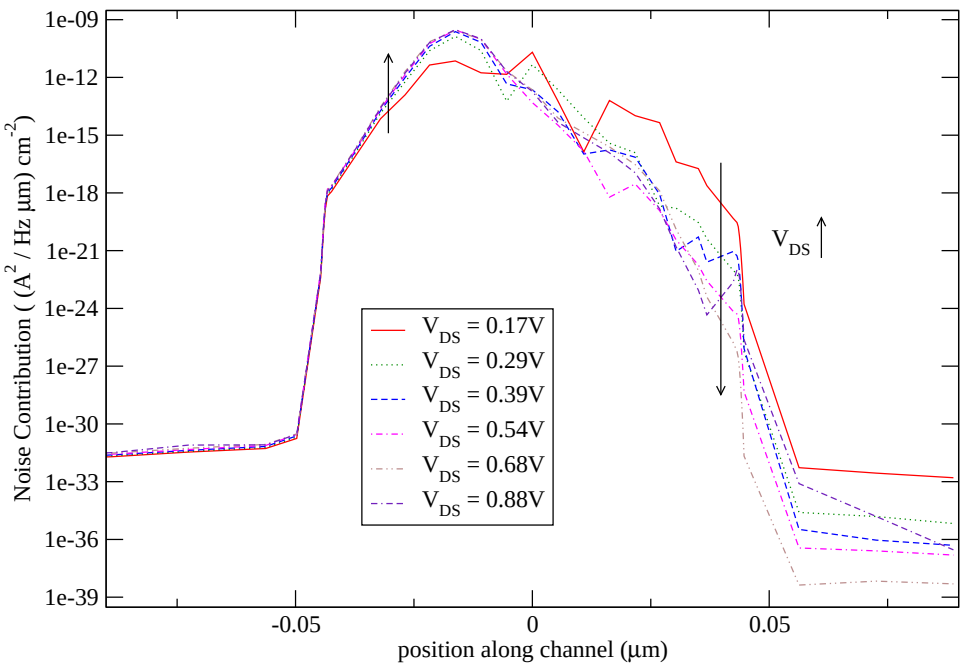

Figure 4-6. Contribution to drain current noise of oxide trapping along the channel in $3.2\mu m$ x $90nm$ bulk device (source on the left and drain on the right) at the depth of oxide contributing most at 1kHz.

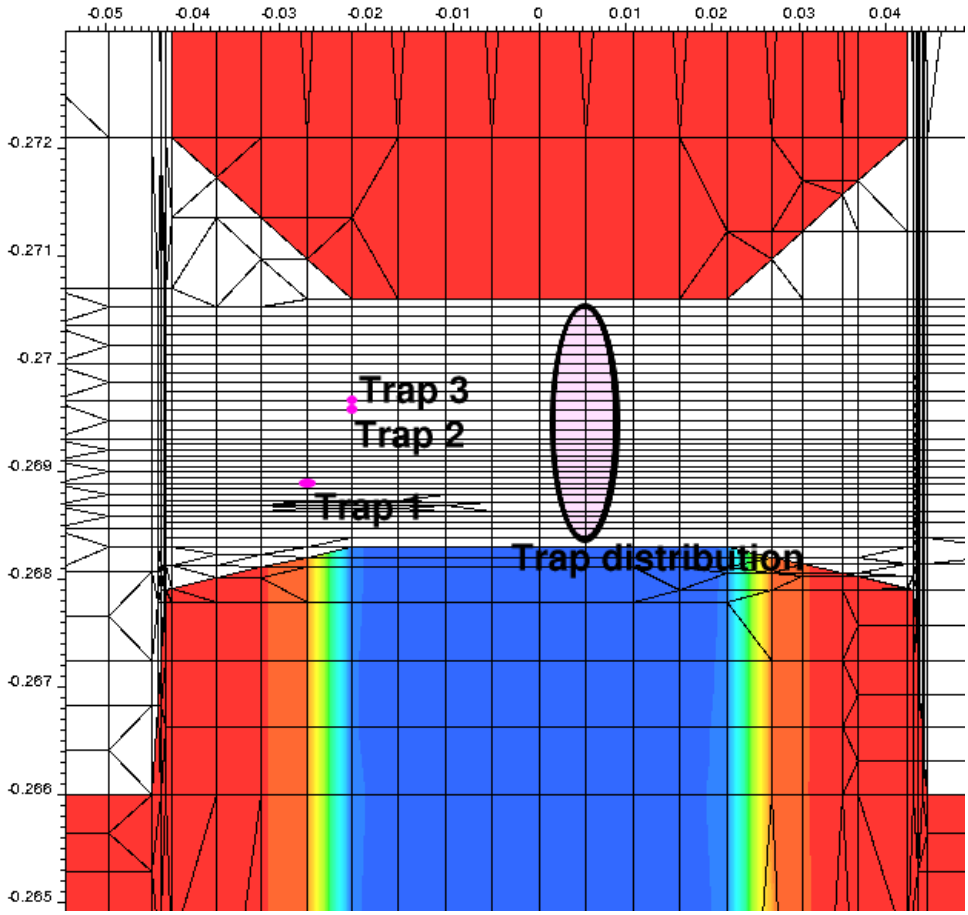

Figure 4-7. Graphical depiction of locations of traps on mesh for simulating the 90nm Bulk nMOSFET.

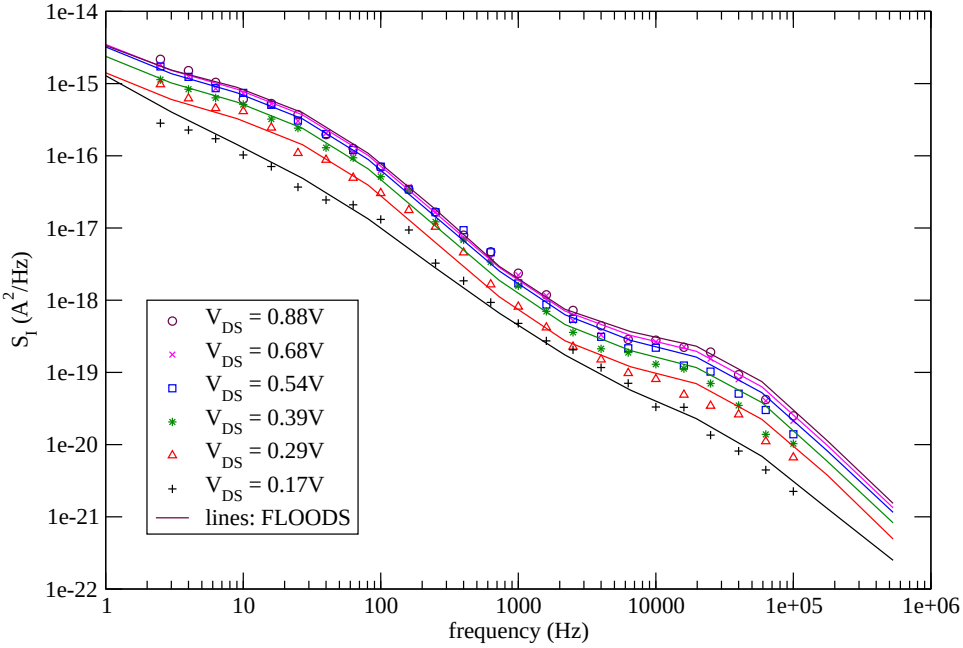

Figure 4-8. Final fit of measured and simulated noise for the 90nm Bulk nMOSFET.

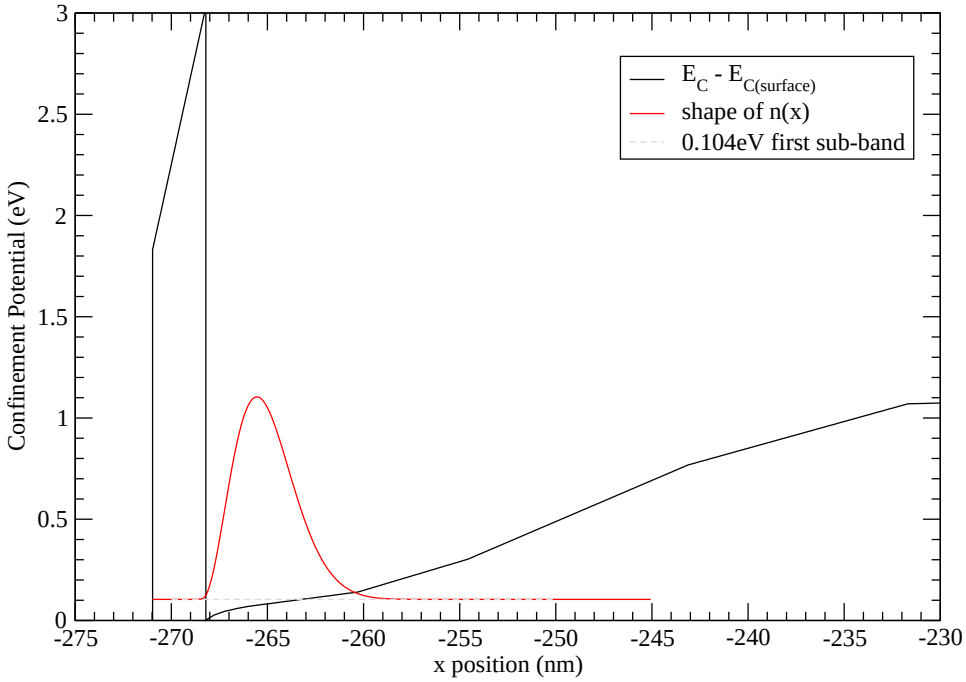

Figure 4-9. First order quantized n(x) under trap 1, assuming all carriers are in the first subband and using the potential well from the classical simulation.

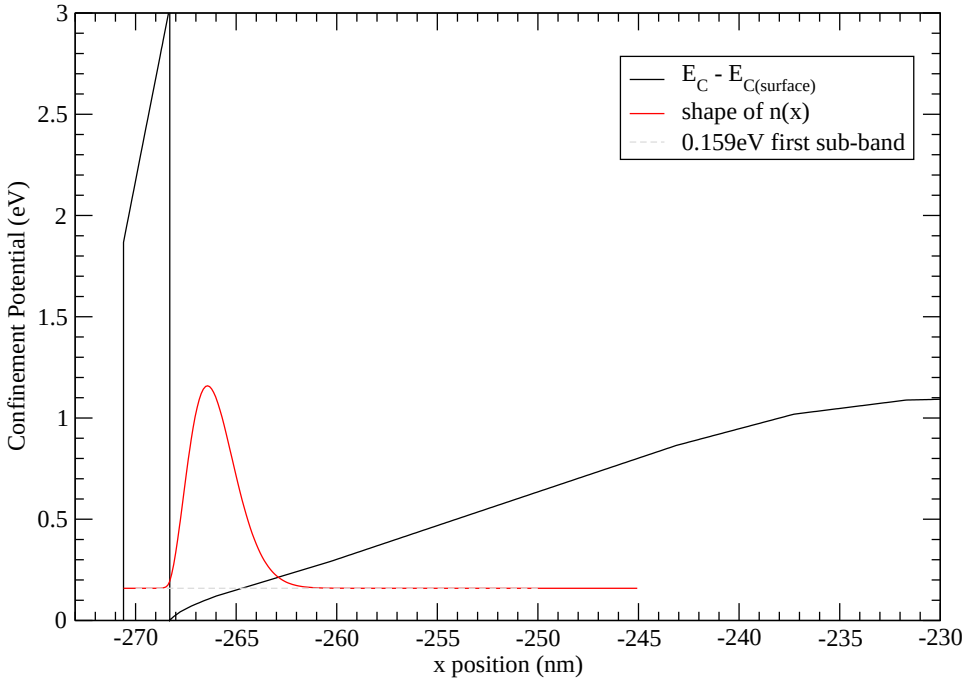

Figure 4-10. First order quantized n(x) under traps 2 and 3, assuming all carriers are in the first subband and using the potential well from the classical simulation.

Table 4-1. Final values of impact ionization rate coefficients and carrier recombination lifetimes

parameter	value
A	$1.3 \cdot 10^3 cm^{-1}$
B	$3.9 \cdot 10^6 V/cm$
τ_n	$11ns$
τ_p	$3.9ns$

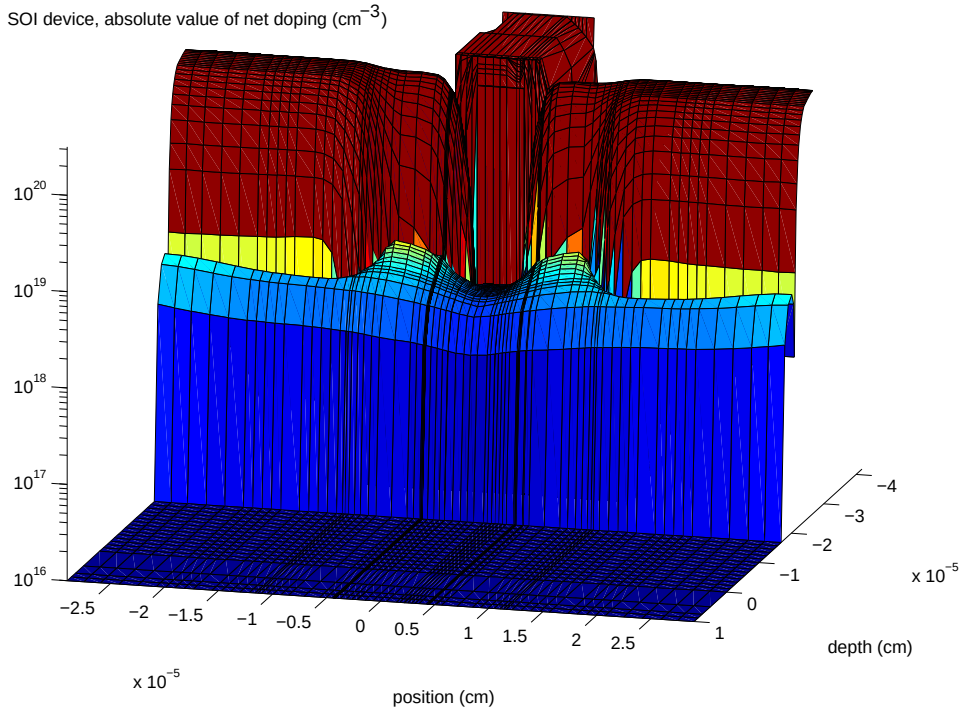

Figure 4-11. Net doping density of the SOI MOSFET simulated in this work. The relative smoothness of this figure near the metallurgical junction compared to that in Figure 4-1 is due to the finer mesh in this region, which was necessary to obtain convergence in the SOI device over V_{DS}.

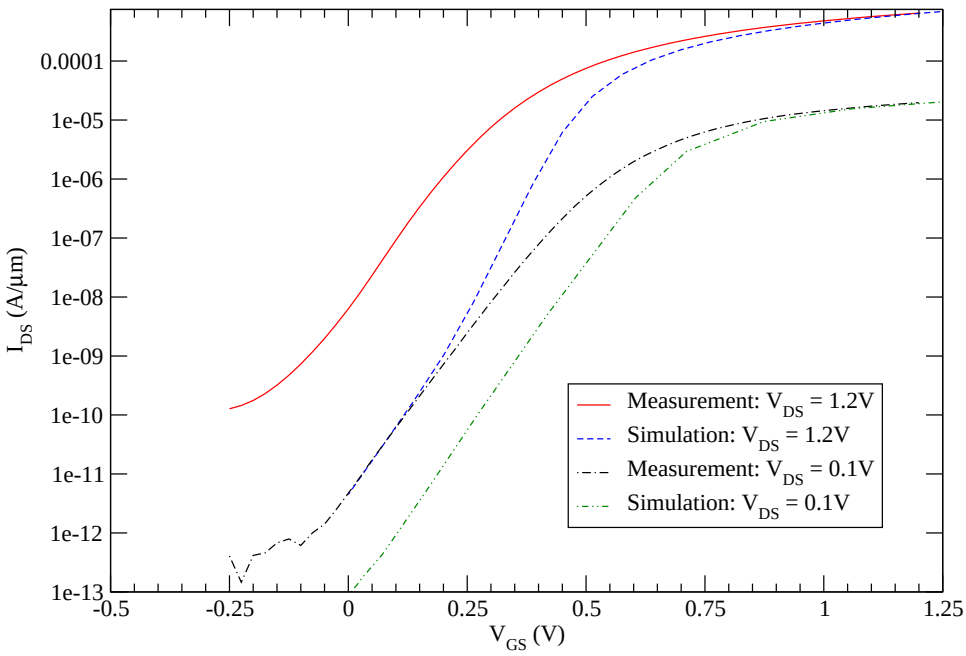

Figure 4-12. Match of simulated gate control IV characteristics for $4.8\mu m x 90nm$ SOI device, for $V_{DS} = 0.01V$ and $V_{DS} = 1.2V$, on a logarithmic scale.

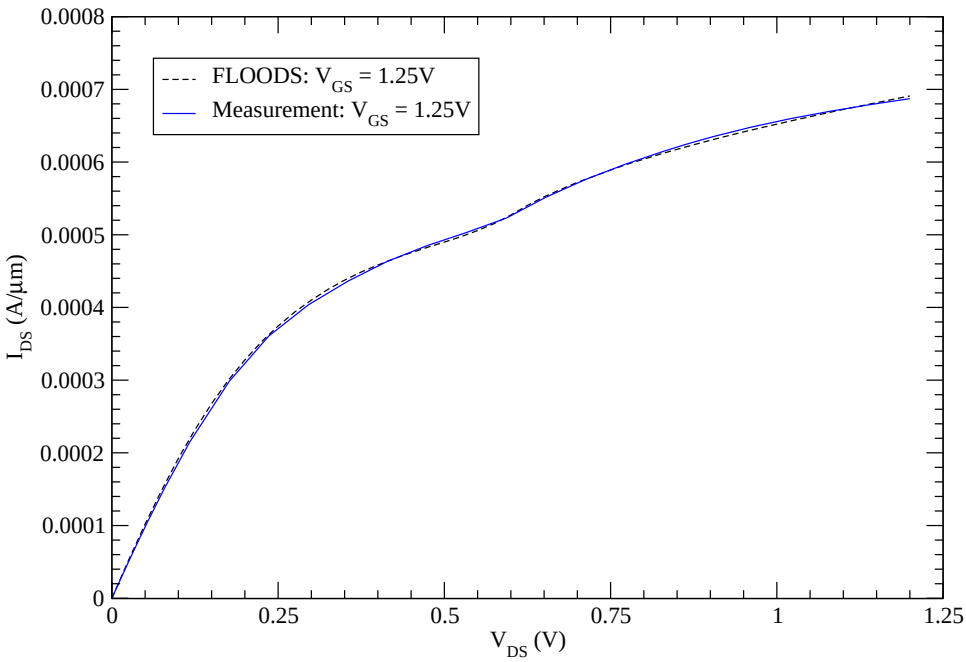

Figure 4-13. Match of simulated drain control IV characteristics for $4.8\mu m x 90nm$ SOI device, for $V_{GS} = 1.25V$.

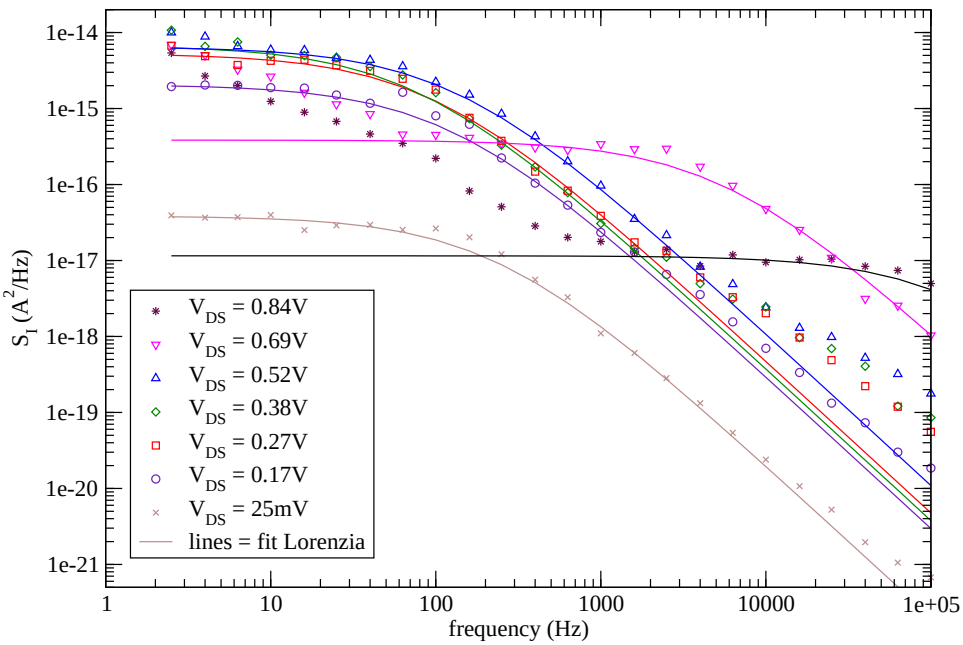

Figure 4-14. Lorentzia mathematically fit to the measured data in order to plot the oxide noise without the diffusion noise in the measurements.

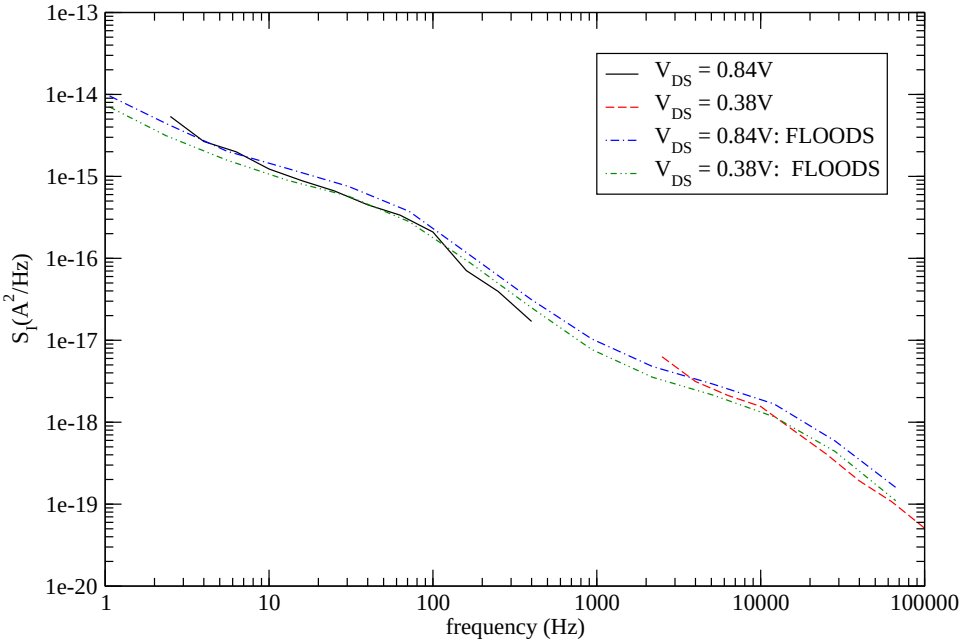

Figure 4-15. Fit of Oxide noise simulations to features in the 0.84V and 0.38V cases, with the excess noise removed.

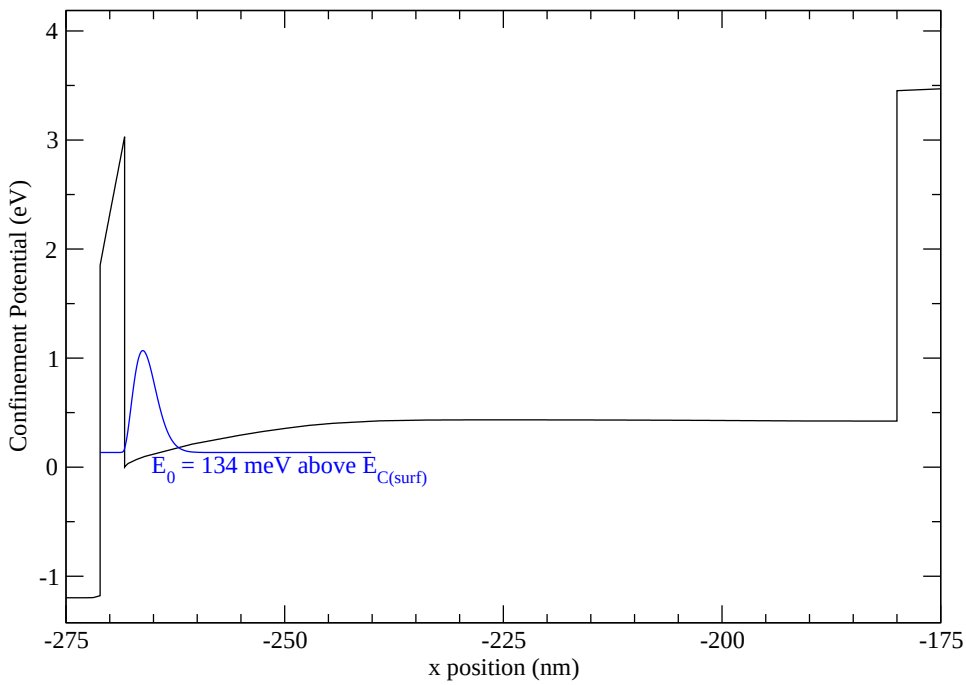

Figure 4-16. First order quantized n(x) under trap 1, assuming all carriers are in the first subband and using the potential well from the classical simulation.

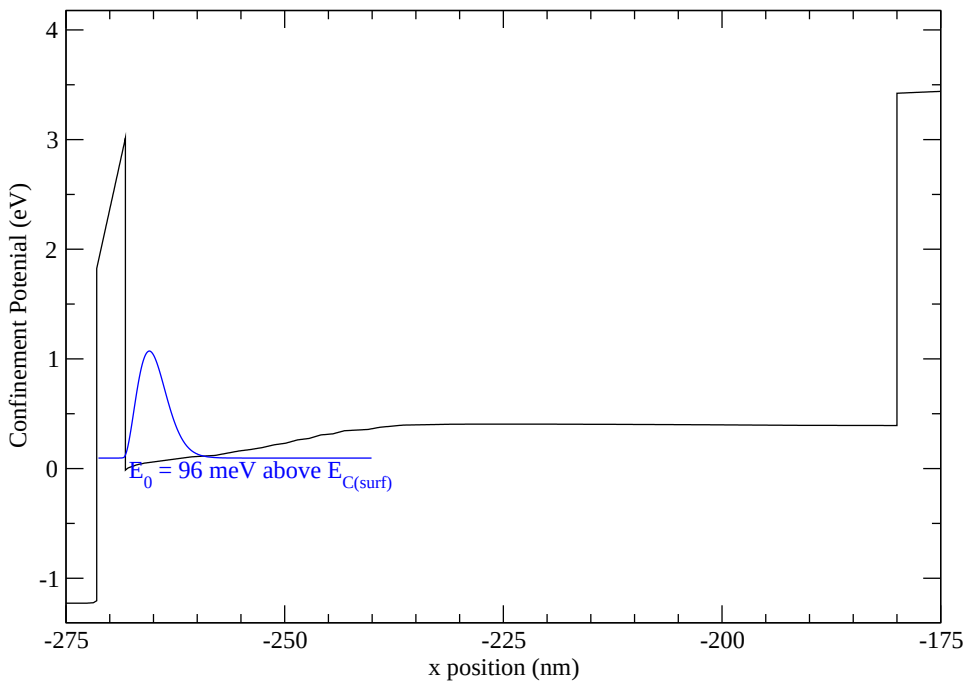

Figure 4-17. First order quantized n(x) under traps 2 and 3, assuming all carriers are in the first subband and using the potential well from the classical simulation.

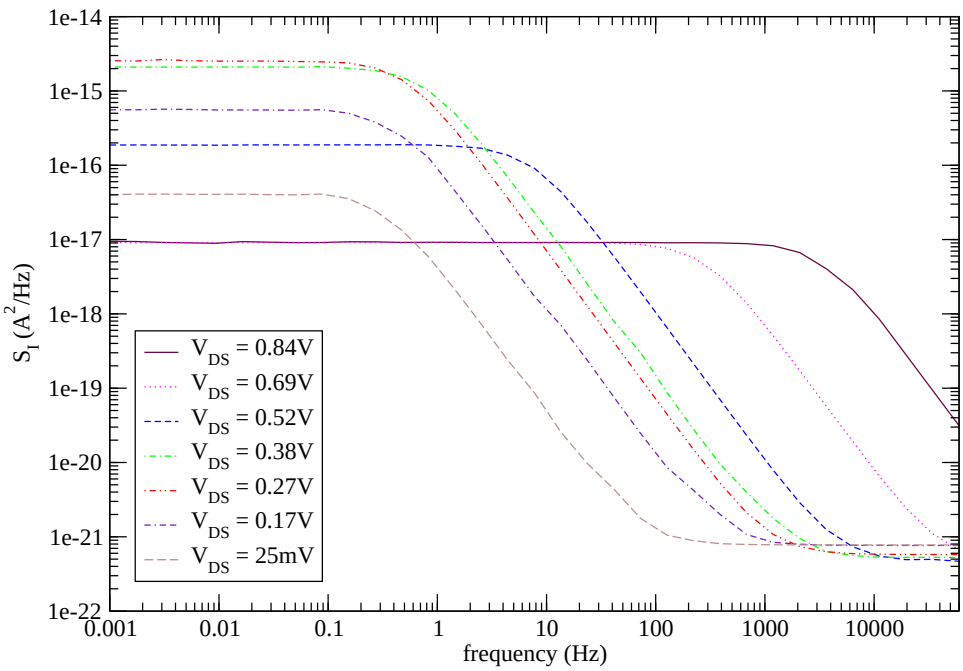

Figure 4-18. Velocity fluctuation noise simulations for $V_{GS} = 1.25V$.

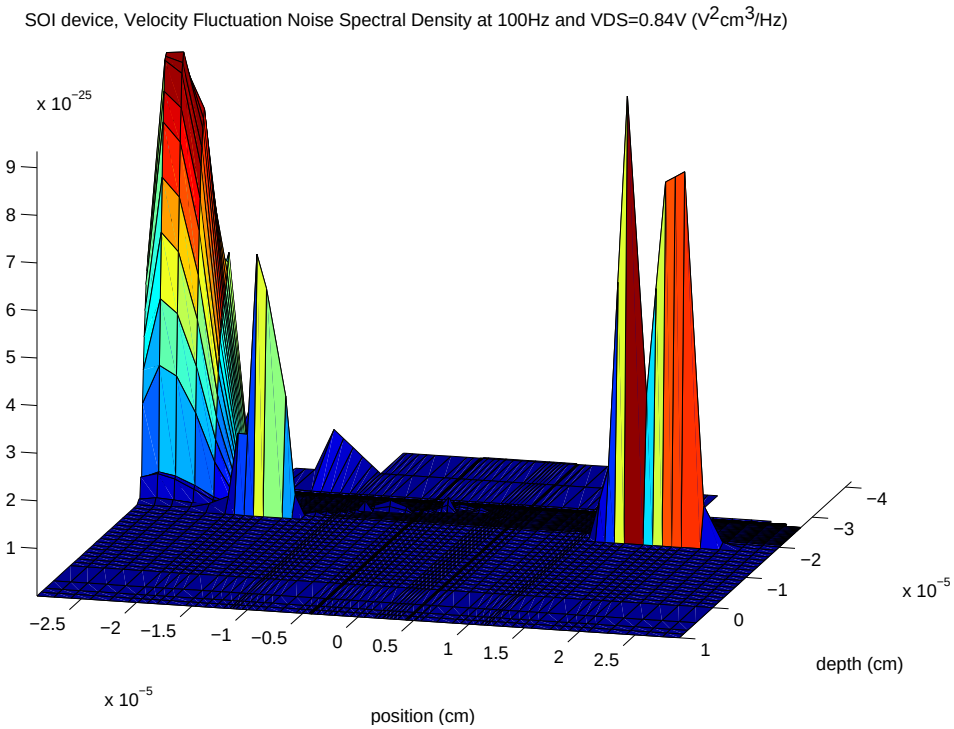

Figure 4-19. Spatial distribution of contributions to the power spectral density at $100Hz$ of the hole diffusion noise in the 90nm SOI device at $V_{DS} = 0.84V$ and $V_{GS} = 1.25V$.

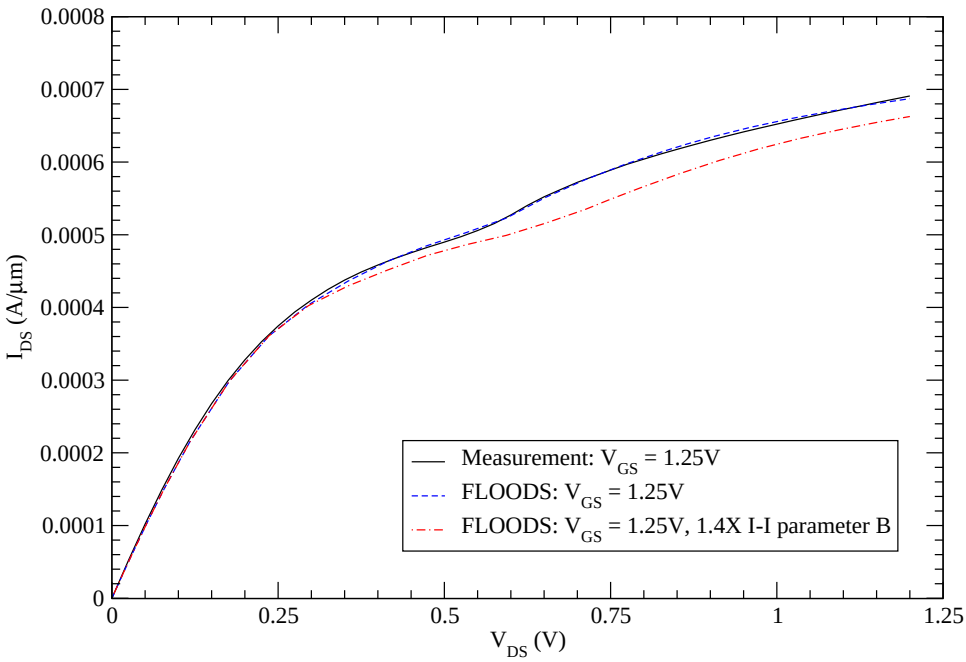

Figure 4-20. Match of simulated drain control IV characteristics, for $V_{GS} = 1.25V$, including case with impact ionization B parameter adjusted by +40%.

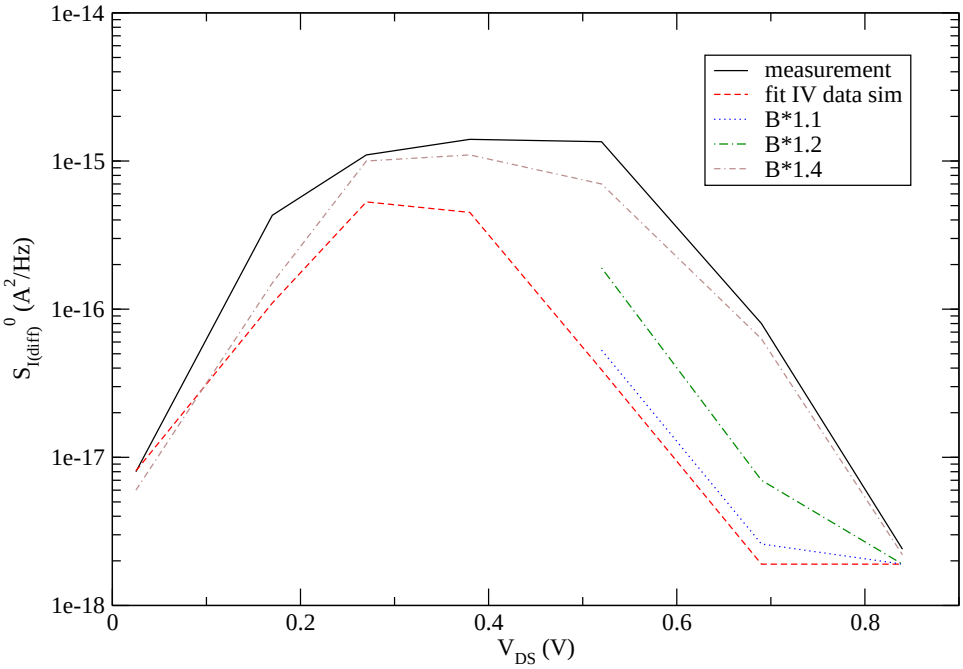

Figure 4-21. Zero-frequency value of Lorentzia in measurement and in simulations with $V_{GS} = 1.25V$. The two simulation cases are with the impact-ionization parameters that gave a good fit for the IV and those that gave a good fit to the noise magnitude.

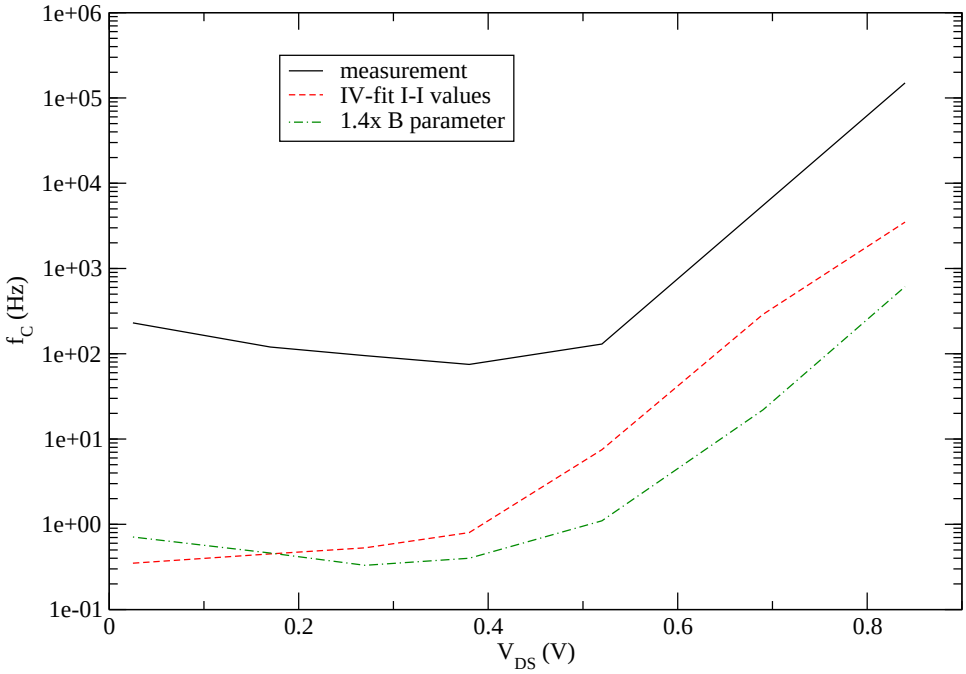

Figure 4-22. Cut-off frequency of Lorentzia in measurement and in simulations with $V_{GS} = 1.25V$. The two simulation cases are with the impact-ionization parameters that gave a good fit for the IV and those that gave a good fit to the noise magnitude.

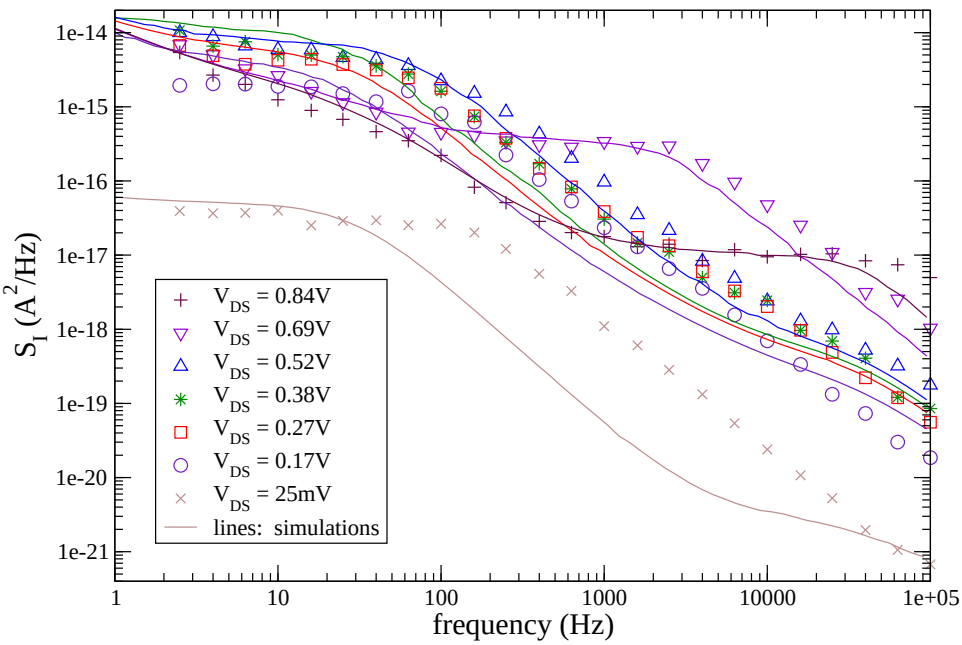

Figure 4-23. Fit of simulated oxide noise and simulated velocity fluctuation noise with corrected fixed interface charge, to the measured data.

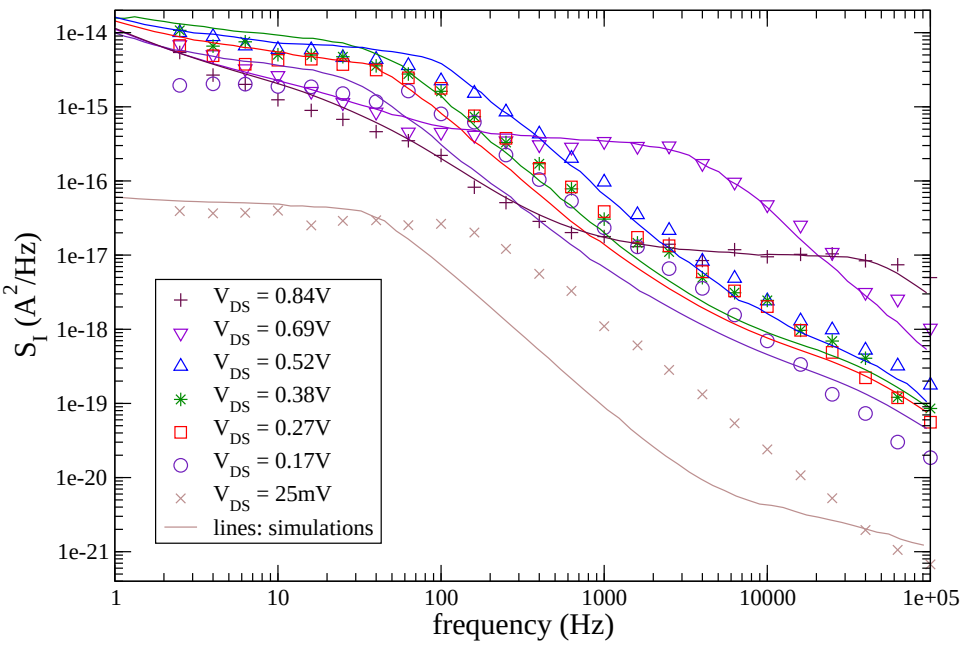

Figure 4-24. Final fit of simulated oxide noise and simulated velocity fluctuation noise, with modified backside film doping, to the measured data.

CHAPTER 5
CONCLUSION

5.1 Summary

The work submitted in this dissertation makes several important contributions to the field of simulations and noise in highly scaled silicon devices. The FLOODS numerical device simulator was enhanced with operators for the Alagator language, which allow the simulations of impact ionization, surface mobility models that depend on transverse electric field, and higher order moments for hydrodynamic models. Highly scaled bulk and partially depleted SOI transistors were measured and a method for reverse engineering them for use in numerical simulations was described. The previous oxide noise simulation work was extended for direct tunneling between interface carriers and oxide traps. The oxide traps in 90nm bulk and SOI transistors were profiled, and the results indicated that specific trap species and position were characteristic of the gate oxidation process. The excess low frequency noise due to impact ionization and subsequent source/body forward bias was simulated and compared with good agreement to the measured data. The shooting method was implemented to solve Schrödinger's Equation, giving a first order correction for the position and energy level of the traps simulated in the devices considered.

5.2 Recommendations for Future Work

For such highly scaled transistors as those used in this work, quantization of carriers in the channel should be included. Though current approaches such as the Van Dort model or the Density Gradient methods can be difficult to simulate and add complexity to an already difficult simulation problem, as numerical solvers and methods improve, these should become possible for the simulation of such devices. This will make it unnecessary to use the fixed charge to reduce the inversion charge in strong inversion, and extend the capability of this work to simulate noise in both subthreshold conditions and strong inversion in a single simulation. Care must be taken to ensure that the small-signal simulations are accurate, however, to make noise simulation possible within such a

framework. Device self-heating (lattice heat flow) is another important component that should be added, though it too adds complexity to the system of PDEs. This would extend this work for the application of modern SiGe BJTs, and improve accuracy for SOI transistors as well.

In addition, as gate oxide thicknesses continue to scale, and as high-dielectric constant insulators are adopted for gate oxides, the implementation of the physics of gate oxide trapping must be refined. Tunneling to the gate should be included, and recent work shows that inelastic tunneling mechanisms such as those explored in work by Lee [50] should be considered as well.

As the modeling of conduction and heat flow mobility models improve for higher-order moments than drift-diffusion, the simulation of partially depleted SOI devices using these transport models should become more accurate, reducing such effects as the negative drain conductance. At this point, impedance field simulations of scaled SOI devices using higher order transport models will be beneficial to give more accurate impact ionization rates, so that the simulation of highly scaled devices sensitive to impact ionization will be more predictive.

Finally, oxide trapping simulation should be applied to double-gate and gate-all-around devices, as the profiling of traps in these gate oxides should provide much insight into these devices' fabrication. Ways to do quantum simulations including noise should be investigated for use in devices such as carbon nanotubes and quantum dots. These devices are likely to require the use of 3D simulations to capture the physics associated with noise, which will require further refinement of the oxide trapping simulation assumptions.

APPENDIX A
APPENDIX: SIMULATION FILES

In this chapter, examples are given of scripts for controlling FLOODS that were used in the simulation of the noise in the devices in this dissertation. Much of the content of code here is leveraged from that of Juan Sanchez, Frank Hou, and Professor Mark Law. The characters "//" indicate that a line was broken here for formatting purposes.

noise7.dd

```
#Simulation of 90nm SOI Device with VDS=0.84V
source dd.phy
source soi.ckt
init silvaco=noise7.sil
source soi.cnt
# Use preconfigured scripts for printing circuit values
source pscripts
source dmswp.tcl
set Vd 0.84
set Vs 0.0
set Vg 1.25
set Vx 0.0
pdbSetDouble Math updateLimit 1.0
pdbSetDouble Math iterLimit 50
pdbSetDouble Math noimpLimit 10
pdbSetBoolean Math residCheck 0
sel name=IntCharge z=2.2e12
sel name=iifact z=1.0
device
device
device
device
device
source traps.ox
set f [open "noise7.dat" w]
for {set freq 1.0e-3} \\
    {$freq <= 1.0e5} \\
    {set freq [expr $freq * 1.75]} {
   puts $freq
   device noise=Cur_Vds freq=$freq oxide
   pac
   set N [expr {abs([circuit value Sdiff name=Cur_Vds])}]
   set N2 [expr {abs([circuit value Sox name=Cur_Vds])}]
   puts $f "$freq $N $N2"
   flush $f
```

```
}
```

dd.phy

```
# Drift-Diffusion

solution name=Potential nosolve
solution add name=DevPsi solve damp negative
solution add name=Elec solve !negative
solution add name=Hole solve !negative
solution add name=nti solve !negative

set Temp 300
source PhyParam
set ni "[ni_cal $Temp]"
set Vt [expr $k*$Temp/$q]
term name=T add eqn="$Temp"

source KlaassenNAs.tcl
source DarwishN.tcl
source KlaassenPB.tcl
set mun "($mun / \\
(sqrt(1.0 + ($mun*diff(DevPsi)/1.3e7)^2)))"
set mup "($mup / \\
(sqrt(1.0 + ($mup*diff(DevPsi)/8.37e6)^2)))"
set taun 1.11108333333333e-08
set taup 3.88891666666667e-09

set U "( $taup*(Elec+$n1) + $taun*(Hole+$p1) )"
set U "(Elec*Hole - $ni*$ni) / $U"
set GII "iifact*eImpact"
set esi [expr 11.7 * 8.85418e-14]
set eps [expr $esi / $q]
set eqnP "$eps * grad(DevPsi) + Doping - Elec + Hole"
set eqnE "ddt(Elec) - ($mun / $q) * \\
hdsgrad(Elec, $q*DevPsi, $k*T) + $U - $GII"
set eqnH "ddt(Hole) - ($mup / $q) * \\
hdsgrad(Hole, -$q*DevPsi, $k*T) + $U - $GII"

# Silicon/Poly
pdbSetDouble Silicon DevPsi DampValue 0.005
pdbSetDouble Silicon DevPsi Abs.Error 1.0e-9
pdbSetString Silicon DevPsi Equation $eqnP
pdbSetString Silicon Elec Equation $eqnE
pdbSetDouble Silicon Elec Abs.Error 1.0e-5
pdbSetString Silicon Hole Equation $eqnH
```

```
pdbSetDouble Silicon Hole Abs.Error 1.0e-5

pdbSetDouble PolySilicon DevPsi DampValue 0.005
pdbSetDouble PolySilicon DevPsi Abs.Error 1.0e-9
pdbSetString PolySilicon DevPsi Equation $eqnP
pdbSetString PolySilicon Elec Equation $eqnE
pdbSetDouble PolySilicon Elec Abs.Error 1.0e-5
pdbSetString PolySilicon Hole Equation $eqnH
pdbSetDouble PolySilicon Hole Abs.Error 1.0e-5

# Oxide
set eso [expr 3.9 * 8.85418e-14]
set epo [expr $eso / $q]
set eqnO "$epo * grad(DevPsi) - nti"
pdbSetDouble Oxide DevPsi DampValue 0.025
pdbSetDouble Oxide DevPsi Abs.Error 1.0e-9
pdbSetString Oxide DevPsi Equation $eqnO

set eqnsurf "DevPsi_Oxide - DevPsi_Silicon"
pdbSetBoolean Oxide_Silicon DevPsi FixedOxide 1
pdbSetBoolean Oxide_Silicon DevPsi FluxConstant 1
pdbSetString Oxide_Silicon DevPsi \\
Equation_Oxide $eqnsurf

set eqnsurf "DevPsi_Oxide - DevPsi_Polysilicon"
pdbSetBoolean Oxide_Polysilicon DevPsi FixedOxide 1
pdbSetBoolean Oxide_Polysilicon DevPsi FluxConstant 1
pdbSetString Oxide_Polysilicon DevPsi \\
Equation_Oxide $eqnsurf

# Nitride
set esn [expr 7.0 * 8.85418e-14]
set epn [expr $esn / $q]
set eqnN "$epn * grad(DevPsi)"
pdbSetDouble Nitride DevPsi DampValue 0.025
pdbSetDouble Nitride DevPsi Abs.Error 1.0e-9
pdbSetString Nitride DevPsi Equation $eqnN

set eqnsurf "DevPsi_Nitride - DevPsi_Oxide"
pdbSetBoolean Oxide_Nitride DevPsi FixedOxide 1
pdbSetBoolean Oxide_Nitride DevPsi FluxConstant 1
pdbSetString Oxide_Nitride DevPsi Equation_Oxide $eqnsurf

#Diffusion Noise
pdbSetString Silicon Elec \\
```

```
Noise.V_Elec "4.0 * $Vt * $mun * Elec"
pdbSetString Silicon Hole \\
Noise.V_Hole "4.0 * $Vt * $mup * Hole"

#Interface/oxide noise stuff
set z 3.1
set cni 1.0e-7
set cpi 1.0e-7
set n1i "cons(Elec_Silicon)"
set p1i "cons(Hole_Silicon)"
set zkt [expr {$z*$Vt}]
set fkt [expr {4.0*$Vt}]
set Nti0 1.0e11
set Nti "( $fkt * $Nti0 * \\
((cons(Elec_Silicon) / $ni)^$zkt) )"

set Rni "( $cni * Elec_Silicon * ($Nti - nti) )"
set Gni "( $cni * $n1i * nti )"
set Rpi "( $cpi * Hole_Silicon * nti )"
set Gpi "( $cpi * $p1i * ($Nti - nti) )"
set Uni "( $Rni - $Gni )"
set Upi "( $Rpi - $Gpi )"
pdbSetBoolean Oxide_Silicon Elec FixedOxide 0
pdbSetBoolean Oxide_Silicon Elec FluxConstant 0
pdbSetString Oxide_Silicon Elec Equation_Silicon "+ $Uni"
pdbSetBoolean Oxide_Silicon Hole FixedOxide 0
pdbSetBoolean Oxide_Silicon Hole FluxConstant 0
pdbSetString Oxide_Silicon Hole Equation_Silicon "+ $Upi"
pdbSetBoolean Oxide_Silicon nti FixedOxide 0
pdbSetBoolean Oxide_Silicon nti FluxConstant 0
pdbSetString Oxide_Silicon nti Equation \\
"ddt(nti) - $Uni + $Upi"
set intcharge "IntCharge"
pdbSetString Oxide_Silicon DevPsi \\
Equation_Silicon $intcharge
pdbSetString Oxide_PolySilicon DevPsi \\
Equation_PolySilicon $intcharge

pdbSetString Oxide_Silicon Elec Noise.N_Elec_SS \\
"2.0 * ($Gni+$Rni)"
pdbSetString Oxide_Silicon Hole Noise.N_Hole_SS \\
"2.0 * ($Gpi+$Rpi)"
pdbSetString Oxide_Silicon nti Noise.N_nti_II \\
"2.0 * ($Gni+$Rni + $Gpi+$Rpi)"
pdbSetString Oxide_Silicon Elec Noise.N_nti_SI \\
```

```
"- 2.0 * ($Gni + $Rni)"
pdbSetString Oxide_Silicon Hole Noise.N_nti_SI \\
"- 2.0 * ($Gpi + $Rpi)"
pdbSetString Oxide_Silicon nti Noise.N_Elec_IS \\
"- 2.0 * ($Gni + $Rni)"
pdbSetString Oxide_Silicon nti Noise.N_Hole_IS \\
"- 2.0 * ($Gpi + $Rpi)"

source dev.ox

# drain
pdbSetBoolean D Elec Fixed 1
pdbSetBoolean D Hole Fixed 1
pdbSetBoolean D DevPsi Fixed 1
pdbSetString D Elec Equation "Doping - Elec + Hole"
pdbSetString D Hole Equation "DevPsi + $Vt*log(Hole/$ni) - D"
pdbSetString D DevPsi Equation "DevPsi - $Vt*log(Elec/$ni) - D"
pdbSetString D Equation "$q * (Flux_Hole - Flux_Elec)"

# source
pdbSetBoolean S Elec Fixed 1
pdbSetBoolean S Hole Fixed 1
pdbSetBoolean S DevPsi Fixed 1
pdbSetString S Elec Equation "Doping - Elec + Hole"
pdbSetString S Hole Equation "DevPsi + $Vt*log(Hole/$ni) - S"
pdbSetString S DevPsi Equation "DevPsi - $Vt*log(Elec/$ni) - S"
pdbSetString S Equation "$q * (Flux_Hole - Flux_Elec)"

# gate
pdbSetBoolean G Elec Fixed 1
pdbSetBoolean G Hole Fixed 1
pdbSetBoolean G DevPsi Fixed 1
pdbSetString G Elec Equation "Doping - Elec + Hole"
pdbSetString G Hole Equation "DevPsi + $Vt*log(Hole/$ni) - G"
pdbSetString G DevPsi Equation "DevPsi - $Vt*log(Elec/$ni) - G"
pdbSetString G Equation "$q * (Flux_Hole - Flux_Elec)"

# body
pdbSetBoolean X Elec Fixed 1
pdbSetBoolean X Hole Fixed 1
pdbSetBoolean X DevPsi Fixed 1
pdbSetString X Hole Equation "Doping - Elec + Hole"
pdbSetString X Elec Equation "DevPsi - $Vt*log(Elec/$ni) - X"
pdbSetString X DevPsi Equation "DevPsi + $Vt*log(Hole/$ni) - X"
pdbSetString X Equation "$q * (Flux_Hole - Flux_Elec)"
```

hd.phy

```
math device dim=2 umf gmres row scale

solution name=Potential nosolve
solution add name=DevPsi solve damp negative
solution add name=Elec solve !negative
solution add name=Hole solve !negative
solution add name=Tn solve damp !negative

set Temp 300
source PhyParam
set ni "[ni_cal $Temp]"
set Vt [expr $k*$Temp/$q]

term name=T add eqn="$Temp"
source KlaassenNAs.tcl
source DarwishN.tcl
source KlaassenPB.tcl
set mup "($mup / (sqrt(1.0 + ($mup*diff(DevPsi)/8.37e7)^2)))"

#gr
set tn 2.0e-11
set tp 6.0e-12
set n1 $ni
set p1 $ni
set U "(Elec*Hole - $ni*$ni)/($tn*(Hole+$p1)+$tp*(Elec+$n1))"

set GI "eImpact"

#Closure Expressions
set Un "($k*Tn)"
set Up "($k*T)"
set Wn "(1.5*$k*Tn)"
set Wno "(1.5*$k*T)"
set taueE 0.4e-12
set dsquig [expr {4/3}]
set lsquig 0.0
set lamp 0.0
set lamep 0.0
set Dsquig [expr {4/3*(1-$lamp-$lamep)}]
set W_U 1.5

set Beta 2.0
set mun "($mun/((sqrt(1.0+0.25*(1.5*$mun*$k*(Tn-$Temp) \\
```

```
/$q/$taueE/1.0e14)^2.0)+0.5*(1.5*$mun*$k*(Tn-$Temp)/$q/ \\
$taueE/1.0e14))))"

set mun "((f)*(eMob)+(1-f)*($mup))"
set mup "((f)*(hMob)+(1-f)*($mup))"
#set mun "eMob"
#set mup "hMob"
set esi [expr 11.7 * 8.85418e-14]
set eps [expr $esi / $q]
set eqnP "$eps * grad(DevPsi) + Doping - Elec + Hole"
set eqnE "ddt(Elec) - ($mun / $q) * \\
hdsgrad(Elec, $q*DevPsi-(1-$lamp)*($Un), $Un) + $U - $GI"
set eqnH "ddt(Hole) - ($mup / $q) * \\
hdsgrad(Hole, -$q*DevPsi, $k*T) + $U - $GI"

set DnSn "(($W_U*$mun/$q) * \\
hdsgrad(Elec*($Un), $dsquig*$q*DevPsi- \\
($Dsquig-$dsquig*$lamp-$lsquig)*($Un), \\
($dsquig+$lsquig)*($Un)))"
set JHe "-(DevPsi*($mun)* \\
hdsgrad(Elec, $q*DevPsi-(1-$lamp)*($Un), $Un))- \\
DevPsi*(ddt(Elec)*$q)"
set nCen "((Elec+1.0e10)*($Wn-$Wno)/($taueE))"
set eqnTE "ddt(Elec*$Wn) + fact*($DnSn) + fact*($JHe) - $nCen"
#set eqnTE "ddt(Elec*$Wn) - $nCen"

# Silicon
pdbSetDouble Silicon DevPsi DampValue 0.005
pdbSetDouble Silicon DevPsi Abs.Error 1.0e-9
pdbSetString Silicon DevPsi Equation $eqnP
pdbSetString Silicon Elec Equation $eqnE
pdbSetDouble Silicon Elec Abs.Error 1.0e-5
pdbSetString Silicon Hole Equation $eqnH
pdbSetDouble Silicon Hole Abs.Error 1.0e-5
pdbSetDouble Silicon Tn DampValue 300.0
pdbSetString Silicon Tn Equation $eqnTE
pdbSetDouble Silicon Tn Abs.Error 1.0e-8

# PolySilicon
pdbSetDouble PolySilicon DevPsi DampValue 0.005
pdbSetDouble PolySilicon DevPsi Abs.Error 1.0e-9
pdbSetString PolySilicon DevPsi Equation $eqnP
pdbSetString PolySilicon Elec Equation $eqnE
pdbSetDouble PolySilicon Elec Abs.Error 1.0e-5
pdbSetString PolySilicon Hole Equation $eqnH
```

```
pdbSetDouble PolySilicon Hole Abs.Error 1.0e-5
pdbSetDouble PolySilicon Tn DampValue 300.0
pdbSetString PolySilicon Tn Equation $eqnTE
pdbSetDouble PolySilicon Tn Abs.Error 1.0e-8

# Oxide
set eso [expr 3.9 * 8.85418e-14]
set epo [expr $eso / $q]
set eqnO "$epo * grad(DevPsi)"
pdbSetDouble Oxide DevPsi DampValue 0.025
pdbSetDouble Oxide DevPsi Abs.Error 1.0e-9
pdbSetString Oxide DevPsi Equation $eqnO

set eqnsurf "DevPsi_Oxide - DevPsi_Silicon"
pdbSetBoolean Oxide_Silicon DevPsi FixedOxide 1
pdbSetBoolean Oxide_Silicon DevPsi FluxConstant 1
pdbSetString Oxide_Silicon DevPsi Equation_Oxide $eqnsurf
set intcharge "IntCharge"
pdbSetString Oxide_Silicon DevPsi Equation_Silicon $intcharge

set eqnsurf "DevPsi_Oxide - DevPsi_Polysilicon"
pdbSetBoolean Oxide_Polysilicon DevPsi FixedOxide 1
pdbSetBoolean Oxide_Polysilicon DevPsi FluxConstant 1
pdbSetString Oxide_Polysilicon DevPsi Equation_Oxide $eqnsurf

#Noise
pdbSetString Silicon Elec Noise.V_Elec "4.0*$k*Tn*$mun*Elec/$q"
pdbSetString Silicon Elec Noise.V_Tn \\
"-4.0*$k*Tn*$mun*Elec*(2.0*$k*Tn/$q-DevPsi)"
pdbSetString Silicon Tn   Noise.V_Tn \\
"4.0*$k*Tn*$mun*Elec*$q*((2.0*$k*Tn/$q-DevPsi)^2.0)"
pdbSetString Silicon Tn Noise.V_Elec \\
"-4.0*$k*Tn*$mun*Elec*(2.0*$k*Tn/$q-DevPsi)"
pdbSetString Silicon Hole Noise.V_Hole \\
"4.0 * $Vt * $mup * Hole"


# G
pdbSetBoolean G Elec Fixed 1
pdbSetBoolean G Hole Fixed 1
pdbSetBoolean G DevPsi Fixed 1
pdbSetBoolean G Tn Fixed 1
pdbSetString G Elec Equation "Doping - Elec + Hole"
pdbSetString G Hole Equation "DevPsi + $Vt*log(Hole/$ni) - G"
pdbSetString G DevPsi Equation "DevPsi - $Vt*log(Elec/$ni) - G"
```

```
pdbSetString G Tn Equation "Tn - T"
pdbSetString G Equation "$q * (Flux_Hole - Flux_Elec)"

# S
pdbSetBoolean S Elec Fixed 1
pdbSetBoolean S Hole Fixed 1
pdbSetBoolean S DevPsi Fixed 1
pdbSetBoolean S Tn Fixed 1
pdbSetString S Elec Equation "Doping - Elec + Hole"
pdbSetString S Hole Equation "DevPsi + $Vt*log(Hole/$ni) - S"
pdbSetString S DevPsi Equation "DevPsi - $Vt*log(Elec/$ni) - S"
pdbSetString S Tn Equation "Tn - T"
pdbSetString S Equation "$q * (Flux_Hole - Flux_Elec)"

# D
pdbSetBoolean D Elec Fixed 1
pdbSetBoolean D Hole Fixed 1
pdbSetBoolean D DevPsi Fixed 1
pdbSetBoolean D Tn Fixed 1
pdbSetString D Elec Equation "Doping - Elec + Hole"
pdbSetString D Hole Equation "DevPsi + $Vt*log(Hole/$ni) - D"
pdbSetString D DevPsi Equation "DevPsi - $Vt*log(Elec/$ni) - D"
pdbSetString D Tn Equation "Tn - T"
pdbSetString D Equation "$q * (Flux_Hole - Flux_Elec)"

# B
pdbSetBoolean B Elec Fixed 1
pdbSetBoolean B Hole Fixed 1
pdbSetBoolean B DevPsi Fixed 1
pdbSetBoolean B Tn Fixed 1
pdbSetString B Hole Equation "Doping - Elec + Hole"
pdbSetString B Elec Equation "DevPsi - $Vt*log(Elec/$ni) - B"
pdbSetString B DevPsi Equation "DevPsi + $Vt*log(Hole/$ni) - B"
pdbSetString B Tn Equation "Tn - T"
pdbSetString B Equation "$q * (Flux_Hole - Flux_Elec)"
```

dev.ox

```
# Oxide Noise Stuff.
set NT 1.2e15
set NC 2.98e19
set yc 0.01085
set yc 0.0
set sy 0.01
pdbSetBoolean Oxide_Silicon Elec degenerate 1
pdbSetString Oxide_Silicon Noise Eqn "Elec"
```

```
pdbSetString Oxide Noise Eqn "nti"
pdbSetString Oxide nti tau0 "2.4e-11"
pdbSetString Oxide nti alpha "-1.4e8"
pdbSetString Oxide_Silicon nti Ntitf "1.0"
pdbSetString Oxide nti Ntox0 \\
"$NT*(exp(-(y-$yc)*(y-$yc)/$sy/$sy))*xf"
pdbSetString Oxide nti eta "2.6e7"
pdbSetString Oxide nti lambda "1e-47"
pdbSetString Oxide nti Nt0 "ntrap"
pdbSetString Oxide_Silicon Elec Nc "$NC"
```

traps.ox

```
# Oxide trap stuff

set win 0.00002
set nt1 2e17
set x1 -0.269562
set y1 -0.0217
set x11 -0.26965
sel name=NT1 z=$nt1*(x>($x1+$win))*(x<($x1-$win))* \\
(y>($y1+$win))*(y<($y1-$win))
sel name=NT11 z=$nt1*(x>($x11+$win))*(x<($x11-$win))* \\
(y>($y1+$win))*(y<($y1-$win))
set nt2 5e18
set x2 -0.268991
set y2 -0.026875
sel name=NT2 z=$nt2*(x>($x2+$win))*(x<($x2-$win))* \\
(y>($y2+$win))*(y<($y2-$win))
sel name=ntrap z=NT1+NT11+NT2
```

soi.ckt

```
#SOI device circuit

circuit clear
circuit add name=Vgs from=G voltage eq = {G-$Vg}
circuit add name=Vds from=D voltage eq = {D-$Vd} \\
ac.r={1.0} ac.i={0.0}
circuit add name=Vss from=S voltage eq = {S-$Vs}
circuit add name=Vxs from=X voltage eq = {X-$Vx}
```

soi.cnt

```
#################################################################
#   Definition of contact regions for device                    #
#################################################################

#
#   Define geometrical locations for contact boxes
```

```
#
contact name=D silicon ylo=0.24 yhi=0.35 xlo=-0.268 xhi=-0.264
contact name=S silicon ylo=-0.35 yhi=-0.24 xlo=-0.268 xhi=-0.264
contact name=G polysilicon ylo=-0.4 yhi=0.4 xlo=-0.42 xhi=-0.417
contact name=X polysilicon xlo=0.099 xhi=0.101
```

KlaassenNAs.tcl

```
#Klaassen Mobility Parameter values for Arsenic

set KEmumax 1417.0
set KEmumin 52.2
set KENref1 9.68e16
set KEalph1 0.68
set KEcD 0.21
set KENrefD 4.0e20
set KEcA 0.50
set KENrefA 7.2e20
set KEtheta_e 2.285
set KEtheta_h 2.247

#Klaassen's fit parameters

set KEme 1.0
set KEmh 1.258
set KEfcw 2.459
set KEfbh 3.828

# Lattice scattering

set KEmuL "($KEmumax*(300.0/T)^$KEtheta_e)"

# Impurity and Hole Scattering.

set KEmuiN [expr "($KEmumax*$KEmumax/($KEmumax-$KEmumin))"]
set KEmuiN "($KEmuiN*(T/300.0)^(3.0*$KEalph1-1.5))"
set KEmuiC [expr "($KEmumax*$KEmumin/($KEmumax-$KEmumin))"]
set KEmuiC "($KEmuiC*(300.0/T)^0.5)"
set KENsc "(Donors+Acceptors+Hole)"
set KEPBH "(1.36e20/Elec*$KEme*(T/300.0)^2.0)"
set KEfoo "(1.0+1.0/($KEcA+($KENrefA/$KENsc)^2.0))"
term name=KEZ add eqn=$KEfoo
set KEPCW "(3.97e13*((1.0/((KEZ)^3.0*$KENsc))* \\
(T/300.0)^3.0)^(2.0/3.0))"
set KEfoo "(1.0/($KEfcw/($KEPCW)+$KEfbh/($KEPBH)))"
term name=KEP add eqn=$KEfoo
```

```
set KEs1 0.89233
set KEs2 0.41372
set KEs3 0.19778
set KEs4 0.28227
set KEs5 0.005978
set KEs6 1.80618
set KEs7 0.72169
set KEfoo \\
"(1.0-$KEs1/($KEs2+((T/300.0/$KEme)^$KEs4)*(KEP))^$KEs3+ \\
$KEs5/((($KEme*300.0/T)^$KEs7)*KEP)^$KEs6)"
term name=KE_G add eqn=$KEfoo

set KEr1 0.7643
set KEr2 2.2999
set KEr3 6.5502
set KEr4 2.3670
set KEr5 -0.01552
set KEr6 0.678
set KEfoo \\
"(($KEr1*KEP^$KEr6+$KEr2+$KEr3*$KEme/$KEmh)/ \\
(KEP^$KEr6+$KEr4+$KEr5*$KEme/$KEmh))"
term name=KE_F add eqn=$KEfoo

set KENsceff "(Donors+KE_G*Acceptors+Hole/KE_F)"

set KEfoo "($KEmuiN*$KENsc/$KENsceff* \\
($KENref1/$KENsc)^$KEalph1+$KEmuiC*(Elec+Hole)/$KENsceff)"
term name=KEmuDAh add eqn=$KEfoo

# Combine using Mathiesson's rule

set KEfoo "($KEmuL*KEmuDAh/($KEmuL+KEmuDAh))"
term name=KEmob add eqn=$KEfoo
set mun "KEmob"
```

DarwishN.tcl

```
#Darwish Electron Model.  Assumes a low field mobility has
#already been defined and $mun is the electron mobility.

#Model parameters

set DEB 3.61e7
set DEC 1.70e4
set DEtau 0.0233
```

```
set DEdelta 1.2e10
set DEA 1.08
set DEalpha 6.85e-21
set DEeta 0.0767
set DEkappa 1.7

#surface acoustic phonon scattering

set DETpri "((T/300.0)^$DEkappa)"
set DEfoo "(($DEB*$DETpri)/(trans(DevPsi)+1.0e-10))"
set DEfoo "($DEfoo+(($DEC*(Donors+Acceptors+Hole)^$DEtau)/ \\
((trans(DevPsi)+1.0e-10)^([expr 1.0/3.0]))))"
set DEmuac "($DEfoo*(1.0/$DETpri))"

#surface roughness scattering

set DEgamma "(($DEA+(($DEalpha*(Elec+Hole))/ \\
((Donors+Acceptors+Hole)^($DEeta)+1.0e-45))))"
set DEmusr "($DEdelta/(((trans(DevPsi))+1e-10)^($DEgamma)+ \\
1.0e-10))"

# Combine using Mathiesson's rule

set DEmob "(($mun)*($DEmuac)*($DEmusr)/(($mun)*($DEmuac)+ \\
($DEmuac)*($DEmusr)+($DEmusr)*($mun)))"
set mun "$DEmob"
```

PhyParam

```
#Physical Constants Used

proc bandgap { T } {
    set A1 1.17;    set B1 1.059e-5;   set C1 -6.05e-7;
    set A2 1.1785;  set B2 -9.025e-5;  set C2 -3.05e-7;
    set A3 1.206;   set B3 -2.73e-4;   set C3 0.0;

    if {$T < 168.0} {
        return [expr {$A1 + $B1*$T + $C1*$T*$T}]
    } elseif {$T < 300.0} {
        return [expr {$A2 + $B2*$T + $C2*$T*$T}]
    } else {
        return [expr {$A3 + $B3*$T + $C3*$T*$T}]
    }
}

set pi 3.14159265358979
```

```
set k 1.38066e-23
set q 1.60218e-19
set mo 0.91093837e-30
set h2 [expr pow(6.6260755e-34,2.0)]

proc mdc_cal { T } {
  set Eg0 "[bandgap 0.0]"
  set Eg "[bandgap $T]"
  set m_t [expr (0.1905*$Eg0/$Eg)]
  set m_l 0.9163
    set foo1 [expr (pow(6.0,(2.0/3.0)))]
    set foo2 [expr (pow($m_t,2.0)*$m_l)]
    set foo3 [expr (1.0/3.0)]
  return [expr ($foo1*pow($foo2,$foo3))]
}

proc mdv_cal { T } {
  set a 0.4435870;     set b 0.3609528e-2;  set c 0.1173515e-3;
  set d 0.1263218e-5;  set e 0.3025581e-8;  set f 0.4683382e-2;
  set g 0.2286895e-3;  set h 0.7469271e-6;  set i 0.1727481e-8;
    set num [expr ($a + $b*$T + $c*$T*$T + \\
    $d*$T*$T*$T + $e*$T*$T*$T*$T)]
    set den [expr (1.0 + $f*$T + $g*$T*$T + \\
    $h*$T*$T*$T + $i*$T*$T*$T*$T)]
    set foo [expr (2.0/3.0)]
  return [expr (pow(($num/$den),$foo))]
}

proc Nc_cal { T } {
  global pi k mo h2
  set m_dc "[mdc_cal $T]"
    set foo \\
    [expr 2.0*pow((2.0*$pi*$k*$mo*300.0/($h2*1.0e4)),1.5)]
  return [expr ($foo*pow(($m_dc*$T/300.0),1.5))]
}

proc Nv_cal { T } {
  global pi k mo h2
  set m_dv "[mdv_cal $T]"
    set foo \\
    [expr 2.0*pow((2.0*$pi*$k*$mo*300.0/($h2*1.0e4)),1.5)]
  return [expr ($foo*pow(($m_dv*$T/300.0),1.5))]
}

proc ni_cal { T } {
```

```
  global k q
  set Eg "[bandgap $T]"
  set Nc "[Nc_cal $T]"
  set Nv "[Nv_cal $T]"
    set foo [expr ($Nc*$Nv*exp(-$Eg*$q/($k*$T)))]
  return [expr sqrt($foo)]
}
```

dmswp.tcl

```
#tcl procedures for doing sweeps
# requires pscripts

proc Ramp1 { varname initv finalv maxstep body} {
    global Vg Vd Vb Vs Vx
    upvar $varname v
    set v $initv
    device
    uplevel $body
    while { [expr abs($initv) ] <  [expr abs($finalv) ] } {
     set initv [ expr $initv + $maxstep ]
if { [expr abs($initv)] > [expr abs($finalv)] } {
    set initv $finalv
    }
set v $initv
     device
uplevel $body
}
    }

proc linsweep { varname initv finalv initstep \\
minstep maxstep filename text1 text2 body } {
# Declare global variables here for contact variables
# (very important, and differs for each device type!)
    global Vg Vd Vx Vs
    upvar $varname v
# Write MCA file preamble
    puts "writing to $filename"
    set ofile [ open $filename w ]
    set ns  "            "
    set msg "%MC-ASCII text {$text1} {$text2} \n%\n%  \\
    record $ns Vd $ns Id $ns Vg $ns Ig $ns Vs $ns Is $ns \\
    Vb $ns Ib\n"
    set un  "%             V   \\8m\\5A/\\8m\\5m"
    append msg "%    None $un $un $un $un\n"
    set ns  "%          "
```

```
    append msg "%     1.0 $ns 1.0 $ns 1.0 $ns 1.0 $ns 1.0 \\
    $ns 1.0 $ns 1.0 $ns 1.0 $ns 1.0"
    puts $ofile $msg
    flush $ofile

    set rcd 100

set v [expr $initv]
set ret [ catch { device } ]
if { $ret } {
  puts "Initial convergence failure!!!"
  break;
}
set step $initstep
set intlv [expr {$initv + $step}]
set v [expr $intlv]
if {$finalv > $initv} {
  set sign 1
} else {
  set sign -1
   }
set ncvg 0
    while { [expr $sign*$intlv ] <  [expr $sign*$finalv ] } {
      set ret [ catch { device } ]
  if { $ret } {
    set intlv [expr {$intlv - $step} ]
set ncvg 0
set step [ expr $step / 1.8 ]
    if { $sign*$step < $minstep } {
      puts " Too small of a step!!!!!"
     break;
}
    puts [format "Non-Convergence!! \\
    Reducing Step to %1.7e" $step]
set intlv [expr {$intlv + $step} ]
set v [expr $intlv]
  } else {
    uplevel $body
    set msg "     $rcd"
    set foo [circuit name=D value]
    append msg [ format "   %1.7e" $foo ]
    set foo [expr [circuit name=Cur_Vds value] * 1e6 ]
    append msg [ format "   %1.7e" $foo ]
    set foo [circuit name=G value]
    append msg [ format "   %1.7e" $foo ]
```

```
    set foo [expr [circuit name=Cur_Vgs value] * 1e6 ]
    append msg [ format "   %1.7e" $foo ]
    set foo [circuit name=S value]
    append msg [ format "   %1.7e" $foo ]
    set foo [expr [circuit name=Cur_Vss value] * 1e6 ]
    append msg [ format "   %1.7e" $foo ]
    set foo [circuit name=X value]
    append msg [ format "   %1.7e" $foo ]
    set foo [expr [circuit name=Cur_Vxs value] * 1e6 ]
    append msg [ format "   %1.7e" $foo ]
    puts $ofile $msg
    flush $ofile
#See if we can increase the step size
        set ncvg [expr $ncvg + 1]
        if { $ncvg >= 3 } {
#3 convergences in a row.  Increase step size!
          set step [ expr $step * 1.9 ]
          if { $step > $maxstep } {
            set step [ expr $maxstep ]
          }
        }
set intlv [expr $intlv + $step]
set v [expr $intlv]
  }
  incr rcd
    }

# while is exited, and intlv is just beyond $finalv.
# revert intlv to last value, and then do whatever it
# takes to drive it to $finalv before exiting.
    set intlv [expr $intlv - $step]
set step [expr $finalv - $intlv]
    while { [expr $sign*$intlv ] <  [expr $sign*$finalv ] } {
  set intlv [expr $finalv]
  set v [expr $intlv]
      set ret [ catch { device } ]
  if {$ret} {
    set intlv [expr $intlv - $step]
set step [ expr $step / 1.7 ]
    if { $step < $minstep } {
      puts " Too small of a step!!!!!"
     break;
}
    puts [format "Non-Convergence!! \\
    Reducing Step to %1.7e" $step]
```

```
set intlv [expr $intlv + $step]
set step [ expr $finalv - $intlv ]
set v [ expr $intlv ]
  }
}

    uplevel $body
    set msg "     $rcd"
    set foo [circuit name=D value]
    append msg [ format "   %1.7e" $foo ]
    set foo [expr [circuit name=Cur_Vds value] * 1e6 ]
    append msg [ format "   %1.7e" $foo ]
    set foo [circuit name=G value]
    append msg [ format "   %1.7e" $foo ]
    set foo [expr [circuit name=Cur_Vgs value] * 1e6 ]
    append msg [ format "   %1.7e" $foo ]
    set foo [circuit name=S value]
    append msg [ format "   %1.7e" $foo ]
    set foo [expr [circuit name=Cur_Vss value] * 1e6 ]
    append msg [ format "   %1.7e" $foo ]
    set foo [circuit name=X value]
    append msg [ format "   %1.7e" $foo ]
    set foo [expr [circuit name=Cur_Vxs value] * 1e6 ]
    append msg [ format "   %1.7e" $foo ]
    puts $ofile $msg
    flush $ofile
puts "Finished with sweep.  Closing $filename."
close $ofile
}

proc diffnoisesweep { varname initv finalv initstep \\
minstep maxstep filehandle text1 text2 body } {
    global Vg Vd Vb Vs Vx
    upvar $varname v
    puts "writing to output"

    set v $initv
    while { [expr abs($initv) ] < \\
    [expr abs($finalv) + 1.0e-4 ] } {
     set ret [ catch { device } ]
if { $ret } {
    set initv [ expr $initv - $initstep ]
    set v $initv
    set initstep [ expr $initstep * 3.0 / 4.0 ]
    if { $maxstep < $minstep } {
```

```
     puts " Too small of a step!!!!!"
     break; }
puts [format "Non-Convergence!! \\
Reducing Step to %1.7e" $initstep]
} else {
uplevel $body
    device
set foo [circuit name=D value]
set msg [format "%1.7e" $foo]
    device noise=Cur_Vds freq=100.0
    set foo [expr \\
    {abs(1.0e4*[circuit value Sdiff name=Cur_Vds])}]
    append msg [ format "   %1.7e" $foo ]
    puts $filehandle $msg
    flush $filehandle
     }

set initstep [ expr $initstep * 6.0 / 5.0 ]
if { $initstep > $maxstep } {
  set initstep [ expr $maxstep ]
}
     set initv [ expr $initv + $initstep ]
set v $initv
# if { [expr abs($initv)] > [expr abs($finalv)] } {
#     set initv $finalv
#     }
}
    close $ofile
    set v $finalv
}
```

pscripts

```
####################
proc pac {} {
    puts "\nAC Solution\n\tReal\t\tImaginary"
        foreach i [circuit nodes] {
            set x [ circuit value real name=$i ]
            set y [ circuit value imag name=$i ]
            puts [ format "%s\t%1.5e\t%1.5e" $i $x $y ]
        }
}

proc pac2 {} {
    puts "\nAC Solution\n\tMagnitude\t\tPhase"
        foreach i [circuit nodes] {
```

```
            set x [ circuit value mag name=$i ]
            set y [ circuit value phase name=$i ]
            puts [ format "%s\t%1.5e\t%1.5e" $i $x $y ]
        }
}

proc pdc {} {
    puts "DC Solution"
        foreach i [circuit nodes] {
            set x [ circuit value name=$i ]
            puts [ format "%s\t%1.5e" $i $x ]
        }
}


proc phb {} {
    puts "HB Solution"
set f [ hbcircuit freq]
        puts [ format "freq\t%s" $f ]
        foreach i [circuit nodes] {
            set xr [ hbcircuit value name=$i real ]
            set xi [ hbcircuit value name=$i imag ]
            puts [ format "%s\t%s" $i $xr ]
            puts [ format "\t%s" $xi ]
        }
}

proc phb2 {} {
    puts "HB Solution"
set f [ hbcircuit freq]
        puts [ format "freq\t%s" $f ]
        foreach i [circuit nodes] {
            set xr [ hbcircuit value name=$i mag ]
            set xi [ hbcircuit value name=$i pha ]
            puts [ format "%s\t%s" $i $xr ]
            puts [ format "\t%s" $xi ]
        }
}

proc phbac {} {
    puts "HB Solution"
set f [ hbcircuit ss freq]
        puts [ format "freq\t%s" $f ]
        foreach i [circuit nodes] {
            set xr [ hbcircuit value name=$i real ss ]
```

```
            set xi [ hbcircuit value name=$i imag ss ]
            puts [ format "%s\t%s" $i $xr ]
            puts [ format "\t%s" $xi ]
        }
}

proc phbac2 {} {
    puts "HB Solution"
set f [ hbcircuit ss freq]
        puts [ format "freq\t%s" $f ]
        foreach i [circuit nodes] {
            set xr [ hbcircuit value name=$i mag ss]
            set xi [ hbcircuit value name=$i pha ss]
            puts [ format "%s\t%s" $i $xr ]
            puts [ format "\t%s" $xi ]
        }
}

proc mydump {ddir} {
    catch {exec mkdir $ddir}
    cd $ddir
    set f [select]
    foreach i $f {
if { ![string compare $i EdgeCouple] } continue
#  puts $i
select z= $i
print.data outf=$i.dat
    }
    cd ..
}
```

shoot

```
#!/usr/bin/env perl

use Math::BigFloat;

sub fstr {
  my $l = shift @_;
  my $D = shift @_;
  my $m = Math::BigFloat->new($l);
  $m->bround($D);
  my $mm = $m->mantissa();
  my $MM = $mm->bfloor();
  $MM = "$MM"."\.0";
  my $me = $m->exponent();
```

```
  while (abs($MM)>=10.0) {
    $MM = $MM / 10.0;
    $me += 1;
  }
  my $str = "$MM"."e"."$me";
  return $str;
}

$file = $ARGV[0];
$E = Math::BigFloat->new($ARGV[1]);

$m = (0.26*9.10938188e-31); #kg
$hbar = (1/2/3.141592654)*6.626e-34; # Js
$K = -1.0*($hbar/($m))*$hbar; # J^2s^2/kg or Jm^2
$K = Math::BigFloat->new($K/1.602e-19); # Convert from J to eV

# Note, first and last points y-values don't matter, as they are considered inf.
open(IF,$file);
$i = 0;
while (<IF>) {
  if (/(\S+)\s+(\S+)/) {
    $dat[0][$i] = $1;
    $dat[1][$i] = $2;
    $i++;
  }
}
close IF;

$N = $i;
$psi[0] = Math::BigFloat->new(0);
$psi[1] = Math::BigFloat->new(1e-100);
$max = Math::BigFloat->new(1e-100);
$sign = 1;
for ($i = 2; $i < $N; $i++) {
  $d1 = ($dat[0][$i-1] - $dat[0][$i-2]);
#  if ($d1 < 1e-16) { print "$dat[0][$i] $d1!!\n"; }
  $d2 = ($dat[0][$i] - $dat[0][$i-1]);
#  if ($d2 < 1e-16) { print "$dat[0][$i] $d2!!\n"; }
  $A = $K/($d1+$d2)/$d2;
  $C = $K/($d1+$d2)/$d1;
  $B = -$A-$C;
  $D = $psi[$i-1]*($dat[1][$i-1]-$E);
  # A*Psi(i)+B*Psi(i-1)+C*Psi(i-2)+D=0
  $psi[$i] = (-$B*$psi[$i-1]-$C*$psi[$i-2]-$D)/$A;
  $psi[$i]->bround(25);
```

```
  #$es = fstr($psi[$i]);
  #print "$i $dat[0][$i] $es\n";
  if ($psi[$i] =~ /inf/) {
    $psi[$N-1] = $psi[$i];
    last;
  }
  if (abs($psi[$i]) > $max) { $max = abs($psi[$i]); }
  if ($psi[$i] > 0) {
    if ($psi[$i-1] < 0) {
      $sign = $sign*-1;
    }
  } else {
    if ($psi[$i-1] > 0) {
      $sign = $sign*-1;
    }
  }
}
$sE = fstr($E,25);
$se = fstr($psi[$N-1],25);
$sm = fstr($max,25);
print "$sE $se $sm\n";
```

shoot.fast

```
#!/usr/bin/env perl

$file = $ARGV[0];
$E = $ARGV[1];

$m = (0.26*9.10938188e-31); #kg
$hbar = (1/2/3.141592654)*6.626e-34; # Js
$K = -1.0*($hbar/($m))*$hbar; # J^2s^2/kg or Jm^2
$K = $K/1.602e-19; # Convert from J to eV

# Note, first and last points y-values don't matter, as they are considered inf.
open(IF,$file);
$i = 0;
while (<IF>) {
  if (/(\S+)\s+(\S+)/) {
    $dat[0][$i] = $1;
    $dat[1][$i] = $2;
    $i++;
  }
}
close IF;
```

```
$N = $i;
$psi[0] = 0;
$psi[1] = 1e-100;
$max = 1e-100;
$sign = 1;
for ($i = 2; $i < $N; $i++) {
  $d1 = ($dat[0][$i-1] - $dat[0][$i-2]);
  if ($d1 < 1e-16) { print "$dat[0][$i] $d1!!\n"; }
  $d2 = ($dat[0][$i] - $dat[0][$i-1]);
  if ($d2 < 1e-16) { print "$dat[0][$i] $d2!!\n"; }
  $A = $K/($d1+$d2)/$d2;
  $C = $K/($d1+$d2)/$d1;
  $B = -$A-$C;
  $D = $psi[$i-1]*($dat[1][$i-1]-$E);
  # A*Psi(i)+B*Psi(i-1)+C*Psi(i-2)+D=0
  $psi[$i] = (-$B*$psi[$i-1]-$C*$psi[$i-2]-$D)/$A;
#  $es = fstr($psi[$i]);
#  print "$i $dat[0][$i] $es\n";
  if ($psi[$i] =~ /inf/) {
    $psi[$N-1] = $psi[$i];
    last;
  }
  if (abs($psi[$i]) > $max) { $max = abs($psi[$i]); }
  if ($psi[$i] > 0) {
    if ($psi[$i-1] < 0) {
      $sign = $sign*-1;
    }
  } else {
    if ($psi[$i-1] > 0) {
      $sign = $sign*-1;
    }
  }
}
$y = $psi[$N-1];
print "$E $y $max\n";
```

quantlin

```
#!/usr/bin/perl

use Math::BigFloat;

sub fstr {
  my $l = shift @_;
  my $m = Math::BigFloat->new($l);
  $m->bround(15);
```

```
  my $mm = $m->mantissa();
  my $MM = $mm->bfloor();
  $MM = "$MM"."\.0";
  my $me = $m->exponent();
  while (abs($MM)>=10.0) {
    $MM = $MM / 10.0;
    $me += 1;
  }
  my $str = "$MM"."e"."$me";
  return $str;
}

$n = 1.0;
$sta = Math::BigFloat->new($ARGV[0]);
$sto = Math::BigFloat->new($ARGV[1]);
$N = $ARGV[2];
$step = ($sto-$sta)/$N;
for ($E = $sta->copy(); $E < $sto; $E += $step) {
  $sE = fstr($E);
  $l = `./shoot well.dat $sE`;
  $l =~ /\S+\s+(\S+)/;
  $e = $1;
  print "$sE $e\n";
}
```

quantize

```
#!/usr/bin/perl

use Math::BigFloat;

sub fstr {
  my $l = shift @_;
  my $D = shift @_;
  my $m = Math::BigFloat->new($l);
  $m->bround($D);
  my $mm = $m->mantissa();
  my $MM = $mm->bfloor();
  $MM = "$MM"."\.0";
  my $me = $m->exponent();
  while (abs($MM)>=10.0) {
    $MM = $MM / 10.0;
    $me += 1;
  }
  my $str = "$MM"."e"."$me";
  return $str;
```

```
}

$n = 1.0;
$IE = Math::BigFloat->new($ARGV[0]);
$step = Math::BigFloat->new($ARGV[1]);
$E = $IE;
$flag = 1;
  $l = `./shoot well.dat $E`;
  $l =~ /(\S+)\s+(\S+)/;
  $e0 = Math::BigFloat->new($2);
  $E = $E+$step;
  $i = 1;
$flag2 = 1;
while ($flag) {
  if ($flag2) {
    $l = `./shoot well.dat $E`;
  } else {
    $l = `./shoot.fast well.dat $E`;
  }
  $l =~ /(\S+)\s+(\S+)\s(\S+)/;
  $ma = Math::BigFloat->new($3);
  $me = $ma->exponent();
  $e1 = Math::BigFloat->new($2);
  $sE1 = fstr($E,25);
  $se1 = fstr($e1,25);
  print "Iter $i : $E $se1\n";
  $i++;
  $step = -1.0*$e1*$step/($e1-$e0);
  $E = $E + $step;
  $e0 = $e1->copy();;
  $f = $e1->copy();  $f->babs();
  if ($sE1 eq $sE0) { last; }
  $sE0 = $sE1;
  if ($me < 100) { $flag2 = 0; }  # Don't need BigFloat anymore in shoot.
}
$sE = fstr($E,30);
$se1 = fstr($e1,30);
print "$sE $se1\n";
```

REFERENCES

[1] G. O. Workman, *Physical Modeling and Analysis of Deep-submicron Silicon-On-Insulator CMOS Devices and Circuits*, Ph.d. dissertation, University of Florida, Gainesville, FL, 1999.

[2] M. R. Pinto, *Comprehensive Semiconductor Device Simulation for Silicon ULSI*, Ph.d. dissertation, Stanford University, Palo Alto, CA, 1990.

[3] *UFSOI MOSFET Models, version 6.0*, University of Florida, Gainesville, FL, 1997, revised 2000.

[4] Dongwook Suh and Jerry G. Fossum, "A physical charge-based model for non-fully depleted soi mosfet's and it's use in assessing floating-body effects in soi cmos circuits," *IEEE Transactions on Electron Devices*, vol. 42, no. 4, pp. 728–737, 1995.

[5] M. G. Ancona and B. A. Biegel, "Non-linear discretization scheme for the density-gradient equations," in *Proceedings of the International Conference on Simulation of Semiconductor Processes and Devices 2000*. pp. 6–9, IEEE.

[6] Mark Lundstrom, *Fundamentals of Carrier Transport*, Addison-Wesley Publishing Company, Reading, MA, 1990.

[7] T. Tang, "An improved hydrodynamic transport model for silicon," *IEEE Transactions on Electron Devices*, vol. 40, no. 8, pp. 1469–1477, 1993.

[8] D. B. M. Klaassen, "A unifed mobility model for device simulation–i. model equations and concentration dependence," *Solid-State Electronics*, vol. 35, no. 7, pp. 953–959, 1992.

[9] D. B. M. Klaassen, "A unifed mobility model for device simulation–ii. temperature dependence of carrier mobility and lifetime," *Solid-State Electronics*, vol. 35, no. 7, pp. 961–967, 1992.

[10] Mohamed N. Darwish, Janet L Lentz, Mark R. Pinto, P. M. Zeitzoff, Thomas J. Krutsick, and Hong Ha Vuong, "An improved electron and hole mobility model for general purpose device simulation," *IEEE Transactions on Electron Devices*, vol. 44, no. 9, pp. 1529–1538, sep 1997.

[11] R. Stratton, "Diffusion of hot and cold electrons in semiconductor barriers," *Physical Review*, vol. 126, no. 6, pp. 2002–2014, 1962.

[12] K. Bløtekjær, "Transport equations for electrons in two-valley semiconductors," *IEEE Transactions on Electron Devices*, vol. ED-17, no. 1, pp. 38–47, 1970.

[13] R. Thoma, B. Meinerzhagin, H. Peifer, and W. H. Engl, "A generalized hydrodynamic model capable of incorporating monte carlo results," in *Proceedings of the International Electron Devices Meeting*. 1989, pp. 89–139–89–142, IEEE.

[14] M. Ieong and T. Tang, "Influence of hydrodynamic models on the prediction of submicrometer device characteristics," *IEEE Transactions on Electron Devices*, vol. 44, no. 12, pp. 2242–2251, 1997.

[15] Yiming Li and Shao-Ming Yu, "A unified quantum correction model for nanoscale single- and double-gate mosfets under inversion conditions," *Nanotechnology*, , no. 8, pp. 1009–1016, 2004.

[16] S. Krishnan and J. G. Fossum, "Compact non-local modeling of impact ionization in soi mosfets for optimal cmos device/circuit design," *Solid-State Electronics*, vol. 39, no. 5, pp. 661–668, 1996.

[17] J. L. (Skip) Egley, B. Polsky, B. Min, E. Lyumkis, O. Penzin, and M. Foisy, "Soi related simulation challenges with moment based bte solvers," in *Proceedings of the International Conference on Simulation of Semiconductor Processes and Devices 2000*. 2000, IEEE.

[18] B. Polsky, O. Penzin, K. E. Sayed, A. Schenk, A. Wettstein, and W. Fichtner, "On negative differential resistance in hydrodynamic simulation of partially depleted soi transistors," *IEEE Transactions on Electron Devices*, vol. 52, no. 4, pp. 500–506, 2005.

[19] D. Munteanu and G. Le Carval, "Assessment of anomalous behavior of cmos bulk and partially depleted soi devices," *Journal of the Electrochemical Society*, vol. 149, no. 10, pp. G574–G580, 2002.

[20] I. Bork, et. al., "Influence of heat flux on the accuracy of hydrodynamic models for ultrashort si mosfets," *NUPAD Technical Digest*, pp. 63–66, 1994.

[21] M. Gritsch, et al., "Revision of the standard hydrodynamic transport model for soi simulation," *IEEE Transactions on Electron Devices*, vol. 49, no. 10, pp. 1814–1820, 2002.

[22] K. Banoo and M. Lundstrom, "Electron transport in a model si transistor," *Solid-State Electronics*, 2000.

[23] W. Shockley, J. A. Copeland, and R. P. James, "The impedance field method of noise calculation in active semiconductor devices," in *Quantum Theory of Atoms, Molecules, and the Solid-State*, P.-O. Lowdin, Ed., New York, 1966, pp. 537–563, Academic.

[24] F. Bonani, G. Ghione, S. Donati, L. Varani, and L. Reggiani, "A general framework for the noise analysis of semiconductor devices operating in nonlinear (large-signal quasi-periodic) conditions," in *14th Int. Conf. on Noise in Phys. Syst. and 1/f Fluctuations*, C. Claeys and E. Simoen, Eds., pp. 144–147. World Scientific, Singapore, 1997.

[25] J. E. Sanchez, F.-C. Hou, G. Bosman, and M. E. Law, "Physics based noise simulation implemented in floods," in *TECHON 98*. 1998, Semiconductor Research Corporation.

[26] F. C. Hou, Gijs Bosman, and Mark E. Law, "Characterization of generation-recombination noise using a physics-based device noise simulator," in *15th International Conference on Noise in Physical Systems and* $1/f$ *Fluctuations*, Aug. 1999.

[27] J. E. Sanchez and G. Bosman, "Frequency conversion of flicker noise in bipolar junction transistors," in *Bipolar/BiCMOS Circuits and Technology Meeting*, pp. 176–179. IEEE, Piscataway, NJ, 1998.

[28] F. Hou, "Unpublished work," 2001.

[29] F. C. Hou, *Low Frequency Bulk and Surface Generation-Recombination Noise Simulations of Semiconductor Devices*, Ph.d. dissertation, University of Florida, Gainesville, FL, 2002.

[30] Jung-Suk Goo, Chang-Hoon Choi, Eiji Morifuji, Hisayo Momose Sasaki, Zhiping Yu, Hiroshi Iwai, Thomas H. Lee, and Robert W. Dutton, "Rf noise simulation for submicron mosfet's based on hydrodynamic model," *IEEE Transactions on Electron Device*, vol. 41, no. 3, pp. 330–339, 1994.

[31] F. Bonani, G. Ghione, M. R. Pinto, and R. K. Smith, "An efficient approach to noise analysis through multidimensional physics-based models," *IEEE Transactions on Electron Devices*, vol. 45, no. 1, pp. 261–269, 1998.

[32] E. Starikov, P. Shiktorov, and V. Gruzinkskis, "The acceleration scheme for noise modeling of deep submicron devices," in *16th Int. Conf. Noise Phys. Syst. 1/f Fluct.*, G. Bosman, Ed., pp. 663–668. World Scientific, 2001.

[33] Hyung-Kyu Lim and Jerry G. Fossum, "Threshold voltage of thin-film silicon-on-insulator (soi) mosfet's," *IEEE Transactions on Electron Devices*, vol. ED-30, no. 10, pp. 1244–1251, 1983.

[34] E. Simoen, Ulf Magnusson, Antonio L. P. Rotondaro, and Cor Claeys, "The kink-related excess low-frequency noise in silicon-on-insulator mosts," *IEEE Transactions on Electron Devices*, vol. 41, no. 3, pp. 330–339, 1994.

[35] N. Lukyanchikova, et. al., "Back and front interface related generation-recombination noise in buried-channel SOI pMOSFET's," *IEEE Transactions on Electron Devices*, vol. 43, no. 3, Mar. 1996.

[36] S. Selberherr, W. Hänsch, M. Seavey, and J. Slotboom, "The evolution of the minimos mobility model," *Solid-State Electronics*, vol. 33, no. 11, pp. 1425–1436, 1990.

[37] Claudio Lombardi, Stefano Manzini, Antonio Saporito, and Massimo Vanzi, "A physically based mobility model for numerical simulation of nonplanar devices," *IEEE Transactions on Computer Aided Design*, vol. 7, no. 11, pp. 1164–1171, 1988.

[38] *Dessis-ISE, ISE TCAD Release 6.1*, 1995–2000.

[39] D. L. Scharfetter and H. K. Gummel, "Large-signal analysis of a silicon read diode oscillator," *IEEE Transactions on Electron Devices*, vol. ED-16, pp. 66–77, 1969.

[40] T.-W. Tang, "Extension of the scharfetter-gummel algorithm to the energy balance equation," *IEEE Transactions on Electron Devices*, vol. ED-31, no. 12, pp. 1912–1914, 1984.

[41] A. G. Chynoweth, "Ionization rates for electrions and holes in silicon," *Physics Review*, vol. 109, pp. 1537–40, 1958.

[42] R. V. Overstraeten and H. D. Man, "Measurement of the ionization rates in diffused silicon junctions," *Solid-State Electronics*, vol. 13, pp. 583–608, 1970.

[43] M. Liang and M. E. Law, "Influence of lattice self-heating and hot-carrier transport on device performance," *IEEE Trans. Electron Devices*, vol. 41, no. 12, pp. 2391–2398, Dec. 1994.

[44] M. Liang and M. E. Law, "An object oriented approach to device simulation," *IEEE Trans. Computer-Aided Design*, vol. 13, no. 10, pp. 1235–1240, Oct. 1994.

[45] S. Decker, C. Jungemann, B. Neinhüs, and B. Meinerzhagen, "An accurate and efficient methodology for rf noise simulations of nm-scale mosfets based on a langevin-type drift-diffusion model," in *16th International Conference on Noise in Physical Systems and 1/f Fluctuations*, G. Bosman, Ed., pp. 659–662. World Scientific, 2001.

[46] C. Jungemann, B. Neinhüs, S. Decker, and B. Meinerzhagen, "Hierarchical 2d rf noise simulation of si and sige devices by langevin-type dd and hd models based on mc generated noise parameters," in *IEEE IEDM Tech. Dig.*, pp. 481–484. IEEE, Piscataway, NJ, 2001.

[47] K. M. van Vliet, "Noise and admittance of the generation-recombination current involving srh centers in the space-charge region of junction devices," *IEEE Trans.*

Electron Devices, vol. ED-23, pp. 1236–1246, Nov. 1976.

[48] C. Jungemann, C. D. Nguyen, B. Neinhüs, and B. Meinerzhangen, "Improved modified local density approximation for modeling of size quantization in nmosfets," *MSM*, vol. Hilton Head Island, pp. 458–461, 2001.

[49] B. Neinhüs, C. D. Nguyen, C. Jungemann, and B. Meinerzhagen, "A cpu efficient electron mobility model for mosfet simulation with quantum corrected charge densities," *ESSDERC*, vol. Cork, pp. 332–335, 2000.

[50] Jong-Hwan Lee, *Comprehensive Compact Noise Modeling of Nanoscale CMOS Devices*, Ph.d. dissertation, University of Florida, Gainesville, FL, 2003.

BIOGRAPHICAL SKETCH

Derek O. Martin was born in Colorado Springs, CO, in 1973. He received the B.S.E.E. degree (with honors) and the M.S. degree from the University of Florida, Gainesville, in 1996 and 1998, respectively. He is currently pursuing a Ph.D. degree at the same university. This endeavor has been supported financially by fellowships from the National Science Foundation and the Semiconductor Research Company.

During the fall of 1999 he worked as an intern at Advanced Micro Devices in Sunnyvale, CA. During the summer of 2001 he worked as an intern at Motorola in Tempe, AZ. He has recently been working at Agilent Technologies in Colorado Springs, CO, where he will continue his career upon completion of his Ph.D. His research interests lie in device physics, modeling and design.